POLITECNICO
MILANO 1863

SCUOLA DI INGEGNERIA INDUSTRIALE
E DELL'INFORMAZIONE

Operando X-ray spectroscopic investigation of ceria in redox conditions

Tesi di Laurea Magistrale in
Engineering Physics - Ingegneria Fisica

Author: **Simona Sorrentino**

Student ID: 964084
Advisor: Prof. Giacomo Claudio Ghiringhelli
Co-advisors: Dr. Vinod K. Paidi, Dr. Pieter Glatzel
Academic Year: 2021-22

Abstract

The present study aimed to investigate the electronic structure of cerium dioxide (CeO_2, also known as ceria) using *operando* High Energy Resolution Fluorescence Detection (HERFD) X-ray Absorption Near Edge Spectroscopy (XANES). Ceria has been widely studied in the last decades due to its oxygen storage capacity, which makes it a promising material in the fields of catalysis and biomedicine. However, the microscopic origin of its redox properties has not yet been fully elucidated. HERFD measurements were performed at the European Synchrotron (ESRF, Grenoble), and XANES spectra at the L_3 edge of Ce were acquired under reducing and oxidizing conditions (*i.e.* under H_2 and O_2 flow). It was observed that pure CeO_2 samples were not reduced below 300°C. Therefore, CeO_2 samples with the addition of 1% and 5% of Pt nanoparticles were studied, since the presence of a noble metal is known to enhance ceria's chemical activity. Under H_2 flow, prominent spectral changes appeared in the 1%Pt/CeO_2 and 5%Pt/CeO_2 spectra, which were associated with oxygen vacancies formation in the lattice, accompanied by the localization of electronic charge onto the Ce *4f* states. These spectral changes have not been observed before, providing new insight into ceria catalysis. Overall, this study provides valuable information on the electronic structure of ceria, which could be used to improve its applicability.

Keywords: ceria, catalytic activity, oxygen vacancies, *operando* spectroscopy, HERFD-XAS

Abstract in lingua italiana

La seguente tesi ha l'obbiettivo di investigare il diossido di cerio (CeO_2, anche chiamato ceria), utilizzando la tecnica spettroscopica *High Energy Resolution Fluorescence Detection X-ray Absorption Near Edge Spectroscopy* (HERFD-XANES). Negli ultimi anni la ceria è stata oggetto di ricerca a causa della sua capacità di accomodare e rilasciare atomi di O nel suo reticolo cristallino, proprietà che la rende interessante per molteplici applicazioni nei campi della catalisi e della biomedicina. Tuttavia, l'origine microscopica alla base delle sue proprietà di ossido-riduzione non è stata ancora del tutto identificata. Esperimenti HERFD sono stati eseguiti presso *The European Synchrotron* (ESRF, Grenoble), per acquisire degli spettri XANES all'edge L_3 del Ce, in condizioni di riduzione e di ossidazione (ossia in presenza di H_2 e di O_2). È stato osservato che al di sotto dei 300°C non è possibile ridurre un campione di pura ceria, dunque sono stati indagati campioni di CeO_2 con una piccola percentuale di nanoparticelle di Pt sulla superficie (1% e 5%), dato che è noto in letteratura come la presenza di un metallo nobile amplifichi l'attività chimica della ceria. In presenza di H_2, notevoli cambiamenti sono stati osservati negli spettri dei campioni 1%Pt/CeO_2 e 5%Pt/CeO_2, attribuibili alla creazione di vacanze di O nel reticolo, le quali lasciano della carica elettronica localizzata sugli orbitali *4f* del Ce. L'osservazione di tali cambiamenti negli spettri non era mai stata fatta in precedenza, e introduce nuovi spunti di riflessione nel dibattito sull'attività catalitica della ceria. È possibile pertanto concludere che il presente studio fornisce importanti informazioni circa la struttura elettronica della ceria, dando nuovi strumenti per migliore la sua implementazione nelle varie applicazioni.

Parole chiave: ceria, catalisi, vacanze di ossigeno, spettroscopia *operando*, HERFD-XAS

Contents

Abstract **i**

Abstract in lingua italiana **iii**

Contents **v**

1 Introduction **1**
1.1 Ceria and its applications 1
1.1.1 Medical applications 3
1.2 Ceria electronic structure 5
1.3 Research at ID26 and case study 8

2 Experimental techniques **11**
2.1 XAS 12
2.2 Sample characterization techniques 17
2.3 Beamline ID26 21
2.4 HERFD-XANES 28
2.4.1 Self-absorption in fluorescence-collected data 30
2.5 Operando cell 32
2.6 Measurement protocols 34

3 Results and data analysis **35**
3.1 Pt/CeO_2 sample characterization 35
3.2 Starting material comparison and self-absorption evaluation 40
3.3 CeO_2 42
3.4 Pt/CeO_2 47

4 Discussions **53**
4.1 The effects of oxygen vacancies on Ce electronic structure 54
4.2 Ceria as a support material 60

4.2.1 Platinum on ceria 63
4.2.2 Platinum on ceria in redox conditions 69
4.2.3 Calculation of the fraction of Pt-Ce sites participating in the interaction 79

5 Conclusions and future developments **81**

Bibliography **85**

A Appendix A **91**

B Appendix B **95**

List of Figures **99**

List of Tables **105**

List of Symbols **107**

Acknowledgements **109**

1 | Introduction

1.1. Ceria and its applications

Cerium dioxide (CeO_2), commonly known as ceria, is a well-known cerium compound, and it has long been the subject of a multitude of studies in the last decades, both in academia and in industry, with a number of publications that has been exponentially growing over the years. This growing trend featuring more than 26000 publications concerning CeO_2 between 1950 and 2015 demonstrates the constant increase of interest in the subject [1].

In particular, the papers concerning catalytic applications of ceria in the last years constitute around the 50% of the total number of published papers, as it is visible from the histogram in Figure 1.1, showing how the employment of ceria as a catalyst material is following a similar trend.

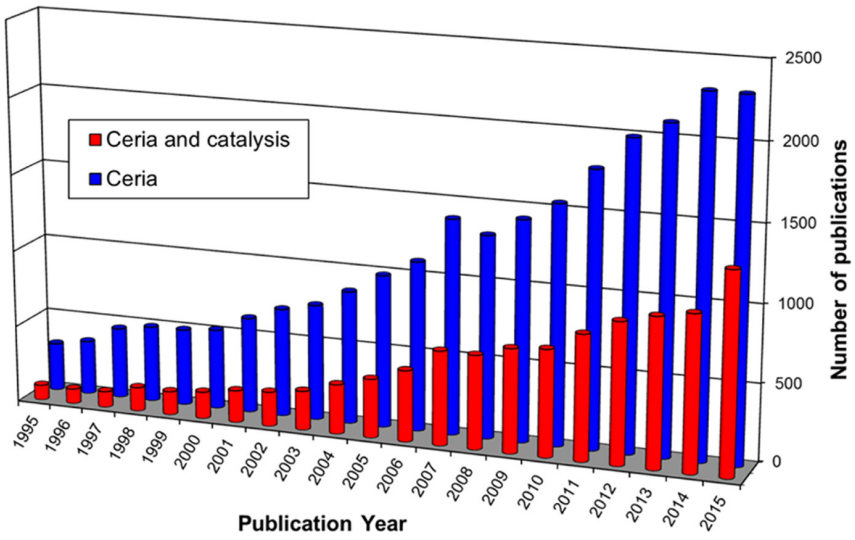

Figure 1.1: Histogram of the number of publications concerning ceria (blue bars) and ceria in the catalysis field (red bars) from 1994 to 2015 [1].

Ceria's wide-spread interest is due to its ability to store, release, and transport oxygen atoms, usually referred to as oxygen storage capacity (OSC), originating from the double

oxidation state of cerium.

In fact, Ce in the CeO_2 structure is present in its oxidized form Ce^{4+}, but is reduced to Ce^{3+} when a neighbouring oxygen vacancy is formed in the lattice, due to structural defects or local compound formation. More specifically, because of such double valence state, under reducing environment ceria is able to release oxygen ions, while under oxidizing conditions it can store oxygen by filling oxygen vacancies.

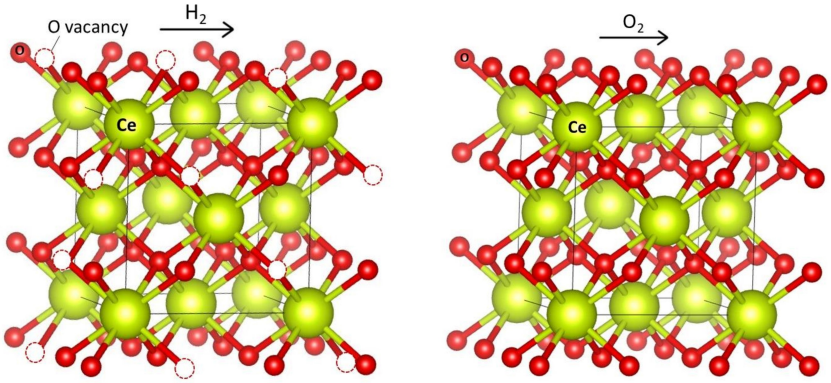

Figure 1.2: Ceria lattice releasing O atoms under reducing environment (H_2), and storing oxygen under oxidizing environment (O_2).

The propensity of ceria to act as an oxygen buffer provides a large variety of applications for ceria, *e.g.* three-way catalysts and fuel cells, because of the derived catalytic activity: in fact, closely linked to CeO_2 number and mobility of oxygen vacancies in the lattice, it is acknowledged a high catalytic performance.

In addition to this, it has been observed that the presence of noble metals can modify the surface properties as well. In particular, ceria is often implemented in combination with platinum group metals (PGM) as active catalysts, because of the enhancement in the redox activity of ceria, that is reduced more easily. Stable systems are reached when platinum nanoparticles are placed on reducible supports, demonstrating how in certain cases the strong synergy arising between the metal and the support material influences the chemical and electronic properties.

Moreover, it is generally accepted that the oxygen storage in ceria is restricted to the surface region, therefore one method to better exploit the catalytic processes is to go to the nanoscale: nanosized ceria is studied in literature because of its increased amount of surface oxygen defects, investing nanoceria with an important role as a catalyst material.

Nanoceria has a high surface-to-volume ratio, and its atom efficiency gives rise to novel catalytic effects, making it a subject of interest in catalysis.

However, beside catalysis there is another scientific field where nanoceria shows remarkably high potentialities, and that is the one where our research finds its origin: the biomedicine field [2]. In fact, among its many biomedical applications, we choose to study nanoceria as it allows to implement catalase mimetic activity and free radical scavenging, while being at the same time non-toxic to the human body.

In particular, by exploiting the oxygen storage capacity, the employment of nanoceria appears promising for improving or creating *ex novo* therapies to reduce inflammations and oxidative stress pathologies by removing excess in reactive oxygen species (ROS) concentration. For this reason, the next section is dedicated to better explore how ceria is implemented in the biomedicine field, and specifically for ROS scavenging activities.

1.1.1. Medical applications

Cerium, like other rare-earth compounds, has been used in medicine since the 19^{th} century: at first it was usually prescribed as anti-emetic agent during pregnancy, but later on it has been implemented also for many other disorders, due to the rapid and widespread popularity that it gained in the field, *e.g.* to treat sickness and coughing, or nervous disorders such as chorea and epilepsy [2].

For unclear reasons it fell into oblivion for a long period of time, probably due to the lack of a mechanistic description of its action and the lack of standardized materials, leading to some controversies in the debate.

Afterward, in the late 1950s, cerium found new popularity in the form of cerium oxide that, tested in rats, showed anti-inflammatory efficacy due to Ce dual oxidation state, better explained in *Section 1.2*.

Later, in 1999, Telek et al. [3] observed anti-inflammatory effects when using cerium chloride for *in vivo* histological detection of oxygen-derived free radicals in inflammatory conditions, and this hinted at a possible role of cerium in the decrease of reactive oxygen species (ROS) concentration.

Finally, the nanoceria biomedical potential was re-discovered less than two decades ago in Virginia Tech, where they observed that nanoceria of less than 20 nm prolonged the lifespan of brain cell cultures for periods of time going up to 6-8 months [4]. Since then, many studies have focused on ceria investigation, to examine its potential therapeutical effects.

ROS and nanoceria

CeO_2 nanoparticles have been found to be effective in modulating the immune response and protecting against oxidative stress, which is a result of inflammation. This imbalance between reactive oxygen species production and antioxidant defense is described by Ernst et al. [2] as a disturbance in the balance. These applications have been explored in the biomedical field.

In order to understand the latter statement, it is useful to start by defining ROS: Reactive Oxygen Species are unstable and highly-oxidant compounds (free radicals), that result from natural metabolic activities of the cells.

These free radicals are involved in different critical physiological processes, among which inflammation, where high ROS concentrations are needed both to activate inflammatory pathways and to sustain the energetic demands of an inflammatory response. For this reason, antioxidant substances can theoretically protect from oxidative stress and facilitate the resolution of the inflammation by inhibiting ROS-dependent inflammatory reactions.

Past experiences with traditional antioxidant substances have shown their high unspecific uncontrolled reactivity, poor solubility and bioavailability, together with low concentrations at the target site, making them not ideal for clinical use, which often is not reached by many substances. On the other hand, nanoceria has been explored as a new antioxidant mineral substance, showing minimal toxicity to tissues and providing cellular protection from ROS-dependent oxidative damage.

High levels of ROS induce oxidative stress, damaging phospholipids and DNA and creating cell mutations and death, favoring the progression of many diseases. Being free radicals, ROS propagate in chain reactions, interacting with other species to form new free radicals, and chain termination occurs when two free radical species react with each other to form stable, non-radical ones: this can be promoted by nanoceria.

Nanoceria, with their ability to store and release oxygen, show permanent ROS scavenging capacities and good pharmacology, advantages that suggest the possibility to finally provide full antioxidant therapies in human health. Based on their ability to reduce ROS levels, they are able to restrict inflammation in many pathologies.

As already mentioned and better discussed in *Section 1.2*, the storage and release of oxygen atoms in CeO_2 is attributed to the two oxidation states of Ce atom in the face-centered cubic crystal lattice, allowing the formation and creation of oxygen vacancies: this originates its oxygen (or electron) buffering capabilities, making cerium a catalyst for both oxidation and reduction reactions.

Nanoceria has been described both as an antioxidant and as an anti-inflammatory agent because of its "electron sponge" behavior, in the sense that a labile unpaired electron from the free radical can be passivated by either pairing it with another electron (provided by ceria as an antioxidant), or removing it (as antireducers do), with opposite effects on pH.

Thus, nanoceria is an antireducer (Ce^{4+} to Ce^{3+}), and an antioxidant (Ce^{3+} to Ce^{4+}) during recycling, providing a high capacity to remove excess ROS from its surroundings.

Furthermore, when discussing medical application, a critical issue is nanosafety: many studies have been carried out and it was found that nanoceria can be used at low doses for prolonged periods of time, and in the neutral pH and low oxidant conditions inside the body it slowly dissolves in few months, Ce^{4+} (insoluble) progressively reducing to soluble Ce^{3+}, that gets excreted through the urine.

Therefore, we can affirm, in conclusion, that nanoceria is a very promising material, but at the same time a long way is necessary to pursue a safe and efficient applicability of ceria nanoparticles for ROS scavenging. A fundamental understanding and predictability of the system are needed, such that it is fundamental to study the system under many different reaction conditions, in order to gain an all-round characterization of nanoceria behavior.

For this reason, it is essential to probe nanoceria, even when the experimental conditions are not analogous to real catalytic applications, as it provides insight into the interactions between model surfaces and small molecules.

The oxygen activation process in CeO_2 has been widely investigated, together with O diffusion at the surface and in the bulk of the material, but its fundamental microscopic origin has not been fully understood yet, and further investigations are required. This is the framework in which our research originates and is inserted, providing small contributions to better understand nanoceria behavior under different reaction conditions.

In order to do this, it is necessary to look at the electronic structure of CeO_2, which is at the very basis of ceria crystal structure and chemical behavior.

1.2. Ceria electronic structure

Cerium is the most abundant rare earth element, and depending on the temperature and on the pressure, many different phases can be achieved by the oxidation of metal Ce with oxygen [1].

CeO_2, specifically, crystallizes in the fluorite structure with a face-centered cubic unit cell

(space group $Fm\bar{3}m$), where eight nearest-neighbor O anions are coordinated around each Ce^{4+} cation at the corners of a cube, and for each anion four cations are coordinated, forming a tetrahedron.

Cerium atom has an electronic configuration $[Xe]4f^1 5d^1 6s^2$ and it exits in two oxidation states: in fact, besides Ce^{4+} (electronic configuration: $[Xe]4f^0 5d^0 6s^0$), Ce cations can be in the oxidation state Ce^{3+}, where the electronic configuration becomes $[Xe]4f^1 5d^0 6s^0$.

When some O anions are released from the CeO_2 lattice, non-stoichiometric $CeO_{2-\delta}$ is achieved, with consequent reduction of some Ce^{4+} to Ce^{3+} and O vacancies formation.

Depending on the amount of O atoms lost by the lattice, different phases can be identified for $CeO_{2-\delta}$, and in general, it is possible to distinguish different spectral near-edge features in absorption spectra according to the oxidation state of Ce, being such features associated to different electronic structures.

In this section a brief description of the main Ce spectral features in the two oxidation states at the L_3 edge is presented, while more detailed considerations are discussed in *Section 4.1*.

Like other rare earths, Ce *4f* electrons are shielded by *4d* and *5p* orbitals: this makes them weakly bound to the nucleus, and therefore allows the two forms Ce^{3+} and Ce^{4+}.

Within the framework of the selection rules for photon-induced electron transitions, using the spin-orbit term notation ^{2S+1}L, we distinguish two symmetry terms for the two oxidation states of cerium [5]:

- ^2F for Ce^{3+}, since we have a configuration f^1 (S=1/2)
- ^1S for Ce^{4+}, since we have a configuration f^0 (S=0)

Since we have different electron spin (S) and orbital angular momentum (L) of the ground state electronic structure in the two cases, we expect different spectral shape of transitions into the *4f* orbitals of Ce, that corresponds to different pre-edge spectral features at the L_3 edge (as visible in Figure 1.3b).

In fact, such region is associated to quadrupole transitions from the Ce *2p* to the Ce *4f* states, leading to one single peak in the case of Ce^{4+}, due to the single spin state (S=0), while in the case of Ce^{3+} two peaks become visible, associated to the two possible spin states.

Also, with high resolution techniques such as HERFD-XAS it is possible to resolve the *5d* fine structure, revealing different features at the near-edge region of the spectra for the

two oxidation states, allowing to distinguish the presence of Ce^{3+} and Ce^{4+}. An example is given in Figure 1.3, where Ce spectra were acquired by means of of X-ray absorption spectroscopy at ID26 during *in situ* ceria nanoparticles synthesis, starting from $CeCl_3$ at a time t=0 (where cerium is in the Ce^{3+} form) and successively achieving CeO_2 (where cerium is Ce^{4+}).

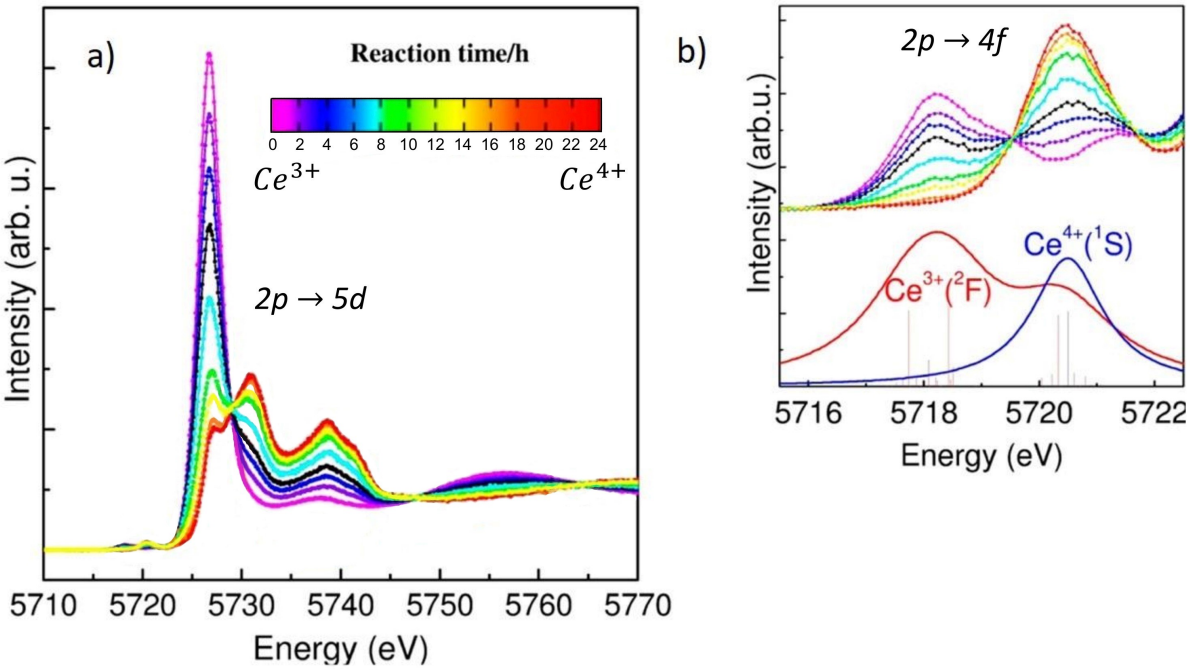

Figure 1.3: a) Time dependent X-ray absorption spectra during *in situ* synthesis of ceria nanoparticles. At time t=0 cerium is Ce^{3+}, while it progressively shifts to its Ce^{4+} configuration; b) Magnification of the pre-edge region corresponding to *2p* to *4f* quadrupole transitions for the two oxidation states of Ce [5].

However, the picture is much more complex due to energetic closeness of the topmost O *2p* orbitals to the lowest vacant Ce *4f* orbitals, leading to a strong hybridization between such states, therefore, when considering cerium dioxide (CeO_2), a multiconfiguration approach is necessary, where the single configuration ionic picture fails in describing Ce inner-shell spectra: the electronic structure of Ce in CeO_2 with formal valence state of IV can be described as a mixture of f^0 and $f^1\underline{L}$ contributions [5].

The notation "$f^1\underline{L}$", considering orbital mixing and sharing of electron density between the two atoms Ce and O, denotes with the term "$\underline{L}$" that a hole in the ligand orbital (*i.e.* O *2p* state) is present and that the Ce f electron is spin-paired with a ligand electron, thus the system remains in a ^1S state independent on the f^0 and $f^1\underline{L}$ mixing ratio, conserving

the Ce spin state.

For this reason, the resulting spectrum of Ce in CeO_2 is not given by the exact sum of the two species contributions f^0 (Ce^{4+}, ^1S) and $f^1\underline{L}$ (Ce^{3+}, ^2F), being more complex than that.

In the case of an oxygen-deficient system ($CeO_{2-\delta}$), in the presence of a strong orbital mixing and an unchanged ^1S spin-orbit state, a correct description is achieved by increasing the $f^1\underline{L}$ contribution.

Moreover, unique new properties appear for CeO_2 at the nanoscale, where some defects are usually present in nanoceria crystal structure, and some Ce ions present a Ce^{3+} valence state. Because of these Ce^{3+} ions we face a deficiency of positive charge that gets compensated with oxygen vacancies, usually occurring at the surface.

Consequently, the particle's size plays an important role in the chemical activity, in fact reducing the size of CeO_2 to the nanometre scale results in an increase of the surface to bulk ratio and thus of the presence of oxygen vacancies: the extra electrons accumulated reduce Ce^{4+} to Ce^{3+}, resulting in a higher level of catalytically active Ce^{3+} at the surface, and therefore in an increased chemical activity.

When Ce^{4+} is reduced to Ce^{3+} and oxygen vacancies are formed, the nanoceria cubic fluorite crystal structure is preserved and, consequently, Ce^{3+} can be easily re-oxidized to Ce^{4+} and the vacancy covered, completing a catalytic loop.

Such complicated picture opens many debates regarding Ce^{3+} formation in CeO_2, where it has been proposed that in 3 nm nanoparticles, where the high surface to bulk ratio increases the presence of oxygen vacancies and thus the reduction of cerium, compensate for the excess charge by modifying the f^0 and $f^1\underline{L}$ mixing ratio, and by increasing the Ce-O distances, rather than favoring the localized surface reduction from Ce^{4+} to Ce^{3+} near the oxygen vacancies [5].

In general, however, because of the above described electronic structure, ceria presents competitive advantages, such as its catalytic behavior, potential biodegradability and electron sponge effect, a peculiar behavior attributed to a delocalized accommodation of charge in the CeO_2 structures.

1.3. Research at ID26 and case study

The complexity of the system and the reactions involved necessitates extensive research to gain a comprehensive understanding of the subject. However, an essential question still

remains: how does the electronic structure of Ce alter in response to modifications of its chemical environment and surroundings?

It is also important to understand which species of Ce are present in CeO_2 under different reaction conditions and upon changing the many factors that can influence the catalytic activity, such as the particle size, the surface area, and the oxidation state.

Also, it is acknowledged that ceria performances are controlled by the size, type and distribution of oxygen vacancies, and a rightful characterization of the latter can lead to a deeper understanding of the fundamental features of the redox activity of the system.

Achieving the control over the density and the nature of oxygen vacancies in nanoceria could allow us to tailor the reactivity of ceria catalysts, therefore our goal is to enrich the understanding of the oxygen vacancies and of their role in the reaction activity, to study how they interact with the system and modify the spectral features.

To gain a detailed understanding of the atomic-level properties of CeO_2, high-resolution instruments and tools have been employed to acquire high-quality spectra capable of detecting the slightest electronic changes. To this end, synchrotron source radiation has been used to investigate nanoceria, with numerous collaborations using the ESRF beamline ID26 over the past decade.

In such context the research project of the present thesis inserts itself, describing a six-month traineeship at ID26 dealing with new experiments outlined and carried out to investigate Ce behavior.

The case study described in the present thesis aims at understanding how oxygen vacancies alter the electronic structure of cerium under reducing and oxidizing environments, and in order to do this, four samples were analyzed: two consisting in pure CeO_2 (one commercial and one lab synthesized) and the other two consisting in CeO_2 with the addition of a small percentage of platinum (1%Pt/CeO_2 and 5%Pt/CeO_2), to enhance ceria redox activity.

We exploited the five crystal analyzer at ID26 to acquire HERFD-XANES (X-ray Absorption Near Edge Structure) spectra of Ce under oxidation and reduction conditions (achieved by flowing respectively oxygen and hydrogen upon the sample), for all the samples at different temperatures (50°C, 200°C, and 300°C).

The spectroscopic techniques alongside with the instruments that were used to carry out the experiments are described in *Chapter 2*, while the experimental results are showed in *Chapter 3*, together with additional details about the samples characterization analysis. Finally, in *Chapter 4* a discussion about the acquired spectra and a possible interpretation of the data are presented.

2 | Experimental techniques

X-ray radiation is a powerful tool for studying the atomic and molecular structure of materials. Its use has been instrumental in a wide range of scientific fields, including materials science, medical imaging, and crystallography.

In the past decades many X-ray sources and technologies have been investigated and developed, in order to better adapt for a variety of different experimental necessities, and in particular, for X-ray photoemission and diffraction measurements X-ray tubes have often been implemented. However, when dealing with X-ray spectroscopy, the usage of such tubes has been drastically reduced due to new and better solutions for X-ray production, *i.e.* synchroton facilities.

Synchrotron facilities generate and accelerate electrons to the desired energy and store them in the so-called storage ring by applying a Lorentz force to keep them in a circular trajectory. Being electrons charged particles, their circular acceleration produces the emission of radiation, *i.e.* X-ray synchrotron radiation.

The reason for the spread of sychrotron radiation implementation over the last few decades must be addressed to a higher flux/brightness parameter, improving from 10^{10} photons per second to 10^{19} with respect to X-ray tubes [6], leading to higher brightness of the beam and much faster experiments. Moreover, the so-produced X-ray beam is characterized by high brilliance (being the beam highly collimated), tunability, polarization properties, time structure, and focal spot size.

For the experiment described in the present work the extremely brilliant source provided at The European Synchrotron (ESRF, Grenoble - FR) was employed [7], working at the beamline ID26.

Figure 2.1: The European Synchrotron Radiation Facility (71 Av. Martyrs, 38000 Grenoble) [8].

The present chapter is dedicated to better describe the potentiality of such high-energy photon beam for the study of matter, starting from a general presentation of XAS and other characterization techniques basic principles (*Section 2.1* and *2.2*) and then going more in detail about the instrumentation and the techniques exploited to perform the experiment.

Section 2.3 is in fact devoted to describe the ID26 beamline, while *Section 2.4* contains specifics about the HERFD-XANES technique used during the experiment and about the data analysis methods.

Finally, *Section 2.5* and *2.6* respectively contain information about the cell hosting the samples analyzed in the case study and the measuring protocols adopted to carry out the experiment.

2.1. XAS

X-ray Absorption Spectroscopy (XAS) is an experimental technique commonly employed in synchrotron facilities to characterize the electronic structure of materials.

We can distinguish two regimes for X-ray radiation - both exploitable at ID26 in two distinct experimental hutches - which are the soft X-rays, ranging from hundreds of eV to a few keV, and the hard X-rays, from a few keV up to around 100 keV. At such energies, the dominant phenomenon driving the interaction of X-rays with matter is the photoelectric effect: upon illuminating the sample with X-ray radiation, X-ray photons of energy $h\nu$ are absorbed by core electrons bounded to the nucleus with energy $h\nu_0 < h\nu$. In fact, if such condition is respected, the X-ray is absorbed and the core electron leaves the sample with a kinetic energy given by Equation (2.1), stating that E_{kin} of the emitted electron is

equal to the energy transferred from the absorbed photon minus the energy required to overcome the Fermi level, which is given by the work function ϕ_0 and is characteristic of the sample.

$$E_{kin} = h\nu - h\nu_0 - \phi_0 \tag{2.1}$$

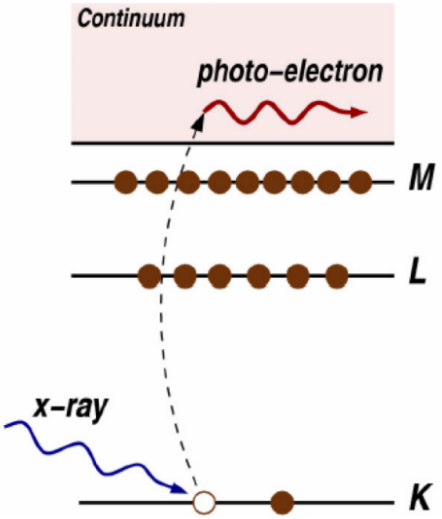

Figure 2.2: Schematic absorption process of an X-ray photon with consequent emission of a core electron [9].

Depending on the core level from which the photo-electron is emitted, the commonly-used nomenclature distinguishes K, L and M edges, where respectively the innermost shell of origin of the emitted electron is n = 1,2, and 3. Therefore, *e.g.*, at the K edge the electron is emitted from the *1s* orbital, while at the L edges the orbitals of origin are the *2p* (L_1 designates the *2s* states, L_2 the $2p_{1/2}$, and L_3 the $2p_{3/2}$, shown in the figure as a unique line).

The probability that such transition of the excited electron from the core level into the continuum occurs is regulated by Fermi Golden Rule (2.2) [10], which gives the probability $\Gamma_{i,f}$ that an electron is excited from an initial state $|i>$ into a final state $|f>$.

$$\Gamma_{i,f} = \frac{2\pi}{\hbar} | < f|H_{int}|i > |^2 \delta(E_f - E_i - h\nu) \tag{2.2}$$

$\Gamma_{i,f}$ is dependent on the interaction Hamiltonian H_{int}: when describing the absorption and emission phenomenon due to incident radiation, H_{int} is the electromagnetic field Hamiltonian and it can be treated in the electric dipole approximation [6]. This leads to

the restriction that the difference in the azimuthal quantum number between the initial and final state Δl must be ± 1. Such imposition added to $\Delta m = 0, \pm 1$ and $\Delta s = 0$, constitutes the selection rules determining which transitions are allowed and which ones are, instead, prohibited.

However, when dealing with X-ray radiation, the dipole approximation is an oversimplification and excludes from the picture quadrupole transitions, that obey $\Delta l = 0, \pm 2$ and constitute an important source of additional possible transitions [6].

Therefore, provided that the beam energy is tuned correctly and the selection rules are respected, the X-rays are absorbed by the sample following Lambert-Beer's law (2.3), that describes the dependence of the intensity I transmitted through the sample on the incident X-ray intensity I_0, the sample thickness t and the absorption coefficient μ.

$$I = I_0 e^{-\mu(E)t} \tag{2.3}$$

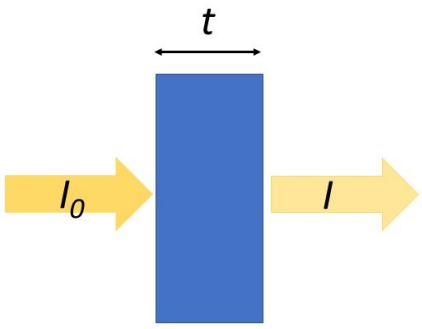

Figure 2.3: Schematic depiction of an X-ray beam of intensity I_0 crossing a sample of thickness t and leaving with final intensity I.

The absorption coefficient strongly depends on the X-ray energy and on the sample, more specifically on its atomic number Z, density ρ and atomic mass A, with a dependence behavior given by Equation (2.4).

$$\mu(E) = \frac{\rho Z^4}{AE^3} \tag{2.4}$$

Furthermore, it shows sharp absorption edges in correspondence of the binding energies of the core-level electrons, that, if provided with right enough energy, absorb the X-ray beam and transit to a higher-energy state or to the continuum.

To perform a XAS measurement means tracking the X-ray absorption probability, that

is linked to the energy dependence of μ, at and above the absorption edges. Since such absorption edges are characteristic for each atom, XAS measurements provide element-selectivity: when starting the experiment, the element to probe is selected by tuning the energy of the X-ray beam to the chosen absorption edge.

A possible way to obtain μ(E) is in transmission, using Lambert-Beer equation (2.5) and directly measuring the initial (I_0) and final (I) beam intensity as a function of the energy.

$$\mu(E) = \frac{1}{t} \ln \frac{I_0}{I} \tag{2.5}$$

Alternatively, the fluorescent de-excitation mechanism providing the core hole annihilation can be exploited. In fact, when the core hole is formed after the absorption, it persists for a limited "lifetime", proceeding to getting re-filled by an electron from a higher-energy core state. The electron decay can happen with different mechanisms, among which the fluorescent one (depicted in Figure 2.4): the decay produces the emission of an X-ray photon, *i.e.* the emission signal, with an energy equal to the difference of the energies of the two core states involved in the transition. μ is then calculated from the ratio of the emitted signal and incoming beam intensities (2.6).

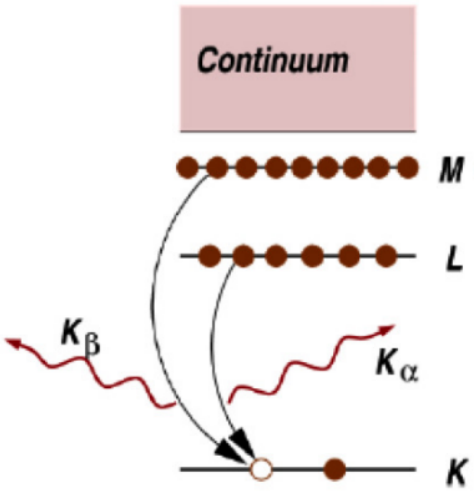

Figure 2.4: Schematic fluorescent de-excitation process of an electron filling the core hole with consequent emission of an X-ray photon [9]. In this example, the emission lines depicted are the K_α, involving the *2p-1s* transitions and the K_β, involving the *3p-1s*.

$$\mu(E) \sim \frac{I_f}{I_0} \tag{2.6}$$

In Figure 2.5 it is offered a schematic layout of the experimental setup at ID26 for measuring both in fluorescence and in transmission mode, better described in *Section 2.3*. The advantages of measuring the absorption coefficient in fluorescence are many, *e.g.* the high resolution achievable, as further discussed in *Section 2.4*.

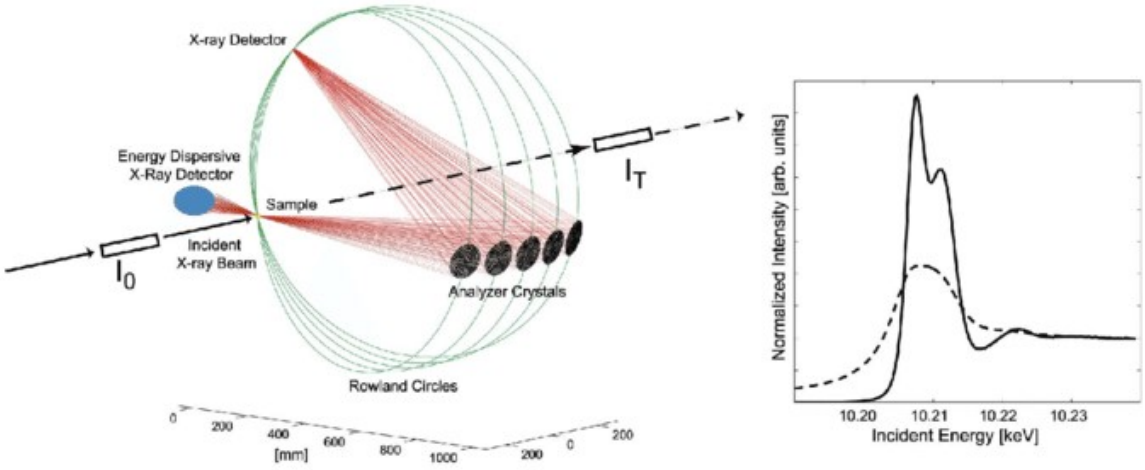

Figure 2.5: Schematic layout of the experimental setup for measuring in fluorescence mode (achieved through the five-analyzer crystal spectrometer) and in transmission mode at ID26 [11].

When high energy resolution is obtained in the measurements, it is possible to observe the fine structure of the absorption coefficient, which is given by its oscillatory behavior below and above the absorption edge (Figure 2.6). Such features are formed by the photo-electron emitted upon X-ray absorption that scatters with the atoms neighbouring the absorbing one: its wavefunction creates interference after single and multiple scattering [12]. The so-produced oscillations visible in the spectra are therefore loaded with meaningful structural information about the sample, *e.g.* inter-atomic distances and coordination number.

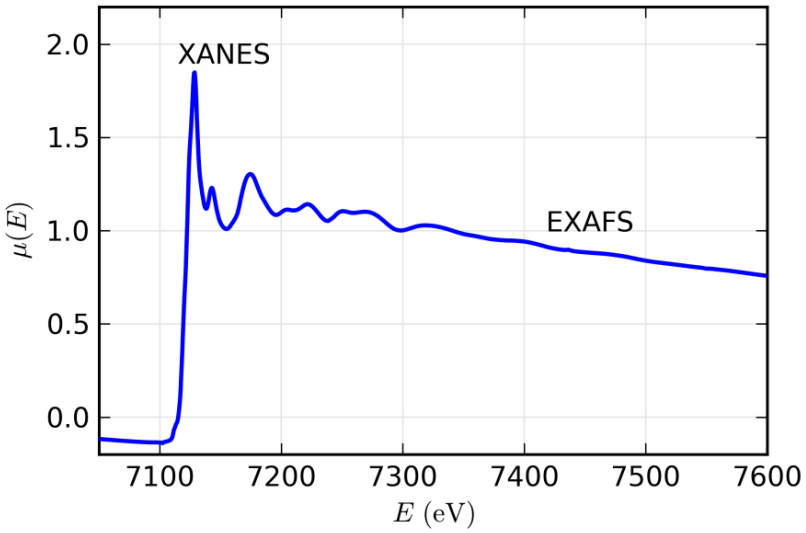

Figure 2.6: Example of absorption spectrum for the Fe K edge of FeO. Two regions are distinguished: the near-edge (XANES) region and the extended fine structure (EXAFS) [13].

Techniques able to detect such fine structure in the absorption spectra are defined X-ray Absorption Fine Structure (XAFS) spectroscopies [14], and as depicted in Figure 2.6, two regions are distinguished in the spectra: the X-Ray Absorption Near Edge Structure (XANES), comprehending transitions to discrete energy levels (including pre-edge features), and the Extended X-Ray Absorption Fine Structure (EXAFS), accounting for transitions into continuum states. In the present case we focused on the XANES region, as better discussed in *Section 2.4*.

2.2. Sample characterization techniques

Before performing the XAS experiment, the samples were analyzed by our collaborators [15]: using different characterization techniques, the goal is to provide an exhaustive comprehension of the samples' structure and surface morphology, in particular about the Pt/CeO_2 case, where it is relevant to understand how the Pt atoms added onto the support have displaced.

- **X-Ray Diffraction (XRD)**

  This technique is commonly used to determine the crystalline structure of the sample. X-rays are chosen with a wavelength λ comparable with the lattice spacing d of the atomic planes in the sample of interest, and are sent onto the sample's surface.

Such incident beam will be diffracted and will produce constructive interference with itself when the Bragg's law is fulfilled (2.7):

$$n\lambda = 2dsin\theta \tag{2.7}$$

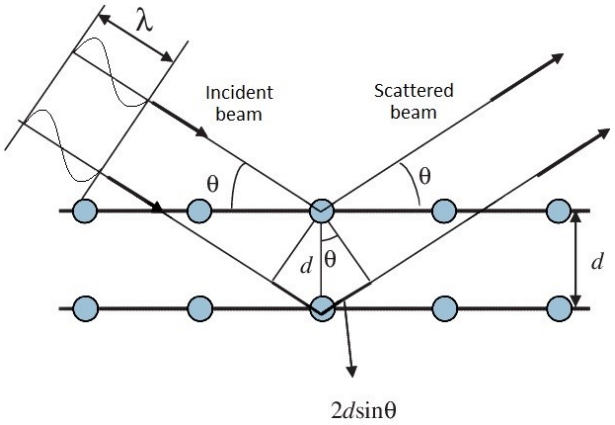

Figure 2.7: XRD experiment scheme: the incident radiation is scattered by the atomic planes and produces constructive interference with itself when Bragg's law is fulfilled.

Results are plotted as the intensity of the signal at different angles of diffraction 2θ (Figure 2.8a): at each value of 2θ that fulfills Bragg's law, constructive interference produces an intensity peak, and from the so-created pattern it is possible to understand the sample composition, crystallinity, and phase purity.

In particular, it is possible to derive the crystallites' size by using Scherrer's equation (2.8), which provides the relationship between the sub-micrometer crystallites in a solid and the broadening of the diffraction peaks in a pattern.

$$\tau = \frac{K\lambda}{\beta cos\theta} \tag{2.8}$$

τ represents the mean size of the crystalline domains, K is the shape factor, λ the wavelength of the X-rays, β the line broadening at half maximum of the intensity minus the broadening due to instrumental effects, and finally, θ is again the Bragg angle.

In our case, XRD patterns were recorded on a D8 Endeavor diffractometer from Bruker, equipped with a Cu K_α monochromatic radiation source at 40 kV and 35 mA ([15], SI).

- **High-Angle Annular Dark Field (HAADF) Scanning Transmission Electron Microscopy (STEM)**

  STEM technique was used to investigate the catalyst morphology and size, and particularly, in order to enhance the contrast between the Pt particles and the ceria support, HAADF was employed.

  HAADF is an imaging technique able to produce an annular dark field image coming from the incoherently scattered electrons at very high angles: since the higher the atomic number Z, the higher the number of electrons scattered at a large angle, a greater signal is detected from atoms with a higher Z, resulting in brighter images (Figure 2.8b).

  This way it is possible to detect small areas occupied by atoms with a larger Z with respect to the rest of the sample, as in our case where platinum clusters are identified and distinguished from the sample.

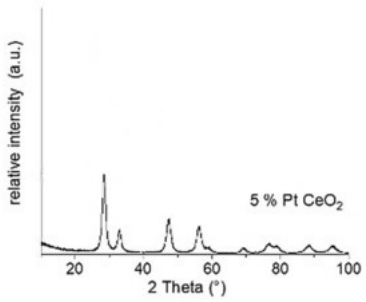

(a) Example of XRD pattern.

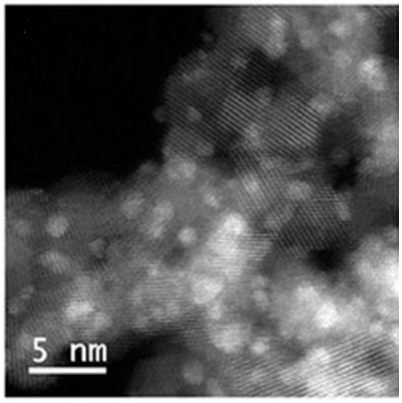

(b) Example of HAADF-STEM image.

Figure 2.8: Examples of images produced by characterization techniques employed on 5%Pt/CeO_2([15], SI).

- **Selected Area Electron Diffraction (SAED)**

  This case figures as a TEM technique as well, exploiting the diffraction patterns created by a beam of high-energy electrons sent through the sample.

  When SAED is performed, a particular sample area is selected by inserting a metallic slit with the chosen aperture below the sample holder, through the beam. This

way, the passing portion of beam corresponds to the selected area from which the diffraction pattern is acquired.

Such technique produces images showing the diffraction spots given by the discrete lattice spacings in a single crystal. When more crystallites are present, as in our case, all possible orientations of crystallographic planes become possible and the superposition of individual crystallites' diffraction patterns produces a diffractogram of concentric rings (Figure 2.9a).

Therefore, SAED allows to study crystallites' structures and characteristics, determine their orientations by looking at the obtained reflections.

- **Near Ambient Pressure X-ray Photoemission Spectroscopy (NAP-XPS)**

  Generally, XPS techniques are based on the acquisition of the kinetic energies of photoemited electrons and therfore require UHV chambers.

  NAP-XPS, on the other hand, is able to operate at pressures of a few tens of mbar: this provides the advantage of working directly under oxygen, particularly useful in our case where such possibility prevented the need of a prior reduction of the sample.

  XPS surface analysis was carried out over a commercial NAP-XPS SPECS operating with a monochromatized Al K_α source at 1486.6 eV and equipped with a reaction cell for NAP analysis ([15], SI).

  NAP-XPS measurements under 5 mbar of gas allowed to detect the well-resolved core levels corresponding to Pt, Ce and O, alongside with the gaseous species photoionized in the proximity of the sample surface (Figure 2.9b).

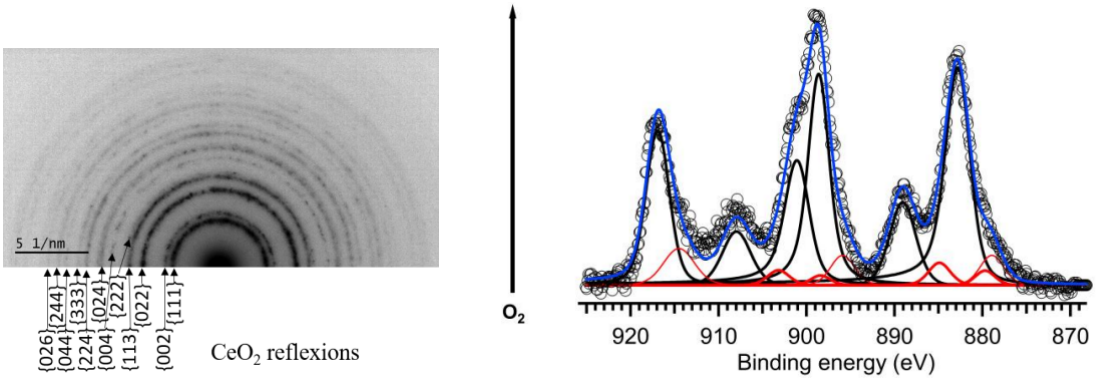

(a) Example of SAED image.

(b) Example of NAP-XPS spectrum.

Figure 2.9: Examples of images produced by characterization techniques employed on 5%Pt/CeO_2([15], SI).

2.3. Beamline ID26

As previously explained, the experiments have been performed at the beamline ID26 at the European Synchrotron Radiation Facility (ESRF) in Grenoble. This beamline is dedicated to X-ray spectroscopy experiments, both in emission and absorption, exploiting the high brilliant source of X-rays coming from the storage ring of the synchrotron.

Figure 2.10 shows a schematic layout of the entire beamline: starting from the right, the X-ray beam leaves the storage ring passing through the undulators, and then proceeds towards two optics hutches where the beam is monochromatized, deflected and focused by the many optical devices present, in order to arrive correctly calibrated onto the sample, which is placed whether in the experimental hutch 1 or 2, according to the necessities of the experiment.

The number of optical devices used inside the beamline is always a trade-off between the necessity to keep the photon flux high (and therefore the number of mirrors and lens low), and to have a high-quality beam.

In fact, each mirror has reflectivity in the order of 80-90%, leading to a 10% minimum of lost photons after each optical element. Moreover, the beam divergence is always slightly bigger after each optical element, due to the inevitable – even if small – lens surface roughness, irregularities etc. For this reason, it is always preferred to limit the number of the optical elements on a beamline.

At the same time, on the contrary, it is fundamental to overcome some necessities such as reduce the heat load, select the incident energies, focus the beam and so on. This leads

to a compromise of a selected number of optical devices that offer sufficient control of the beam parameters while achieving a good quality beam and a reasonable photon flux, and such devices are reported in Figure 2.10.

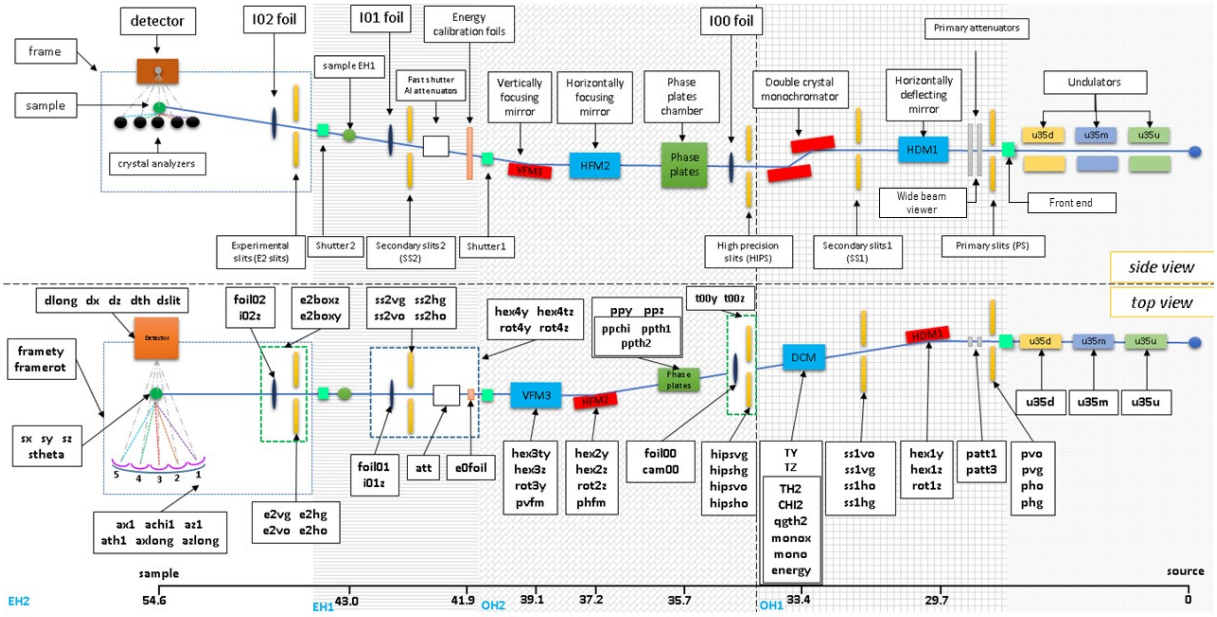

Figure 2.10: Side view and top view of the ID26 beamline. In the upper layout all the optical, electronic and physical elements are depicted, while in the lower one all the motors responsible for the movements of the devices are reported.

During the alignment procedure, all the devices depicted in Figure 2.10 have to be correctly displaced in order to obtain a well collimated beam onto the sample, at the right energy and with a high photon flux.

The functioning and the purpose of each device is described in Appendix A, while below special attention is dedicated to the second experimental hutch, where our experiments were carried out.

In fact, after the optics there are the two experimental hutches where the X-ray emission or absorption spectroscopy experiments are performed: depending on the desired energy range of the X-ray beam (Soft or Hard X-rays), whether the first or the second hutch is chosen.

In the second experimental hutch the beam comes in monochromatized by the double-crystal monochromator placed in the first optics hutch (Figure 2.10), and its size is set by correctly adjusting the motorized slits.

Samples can be mounted on several holders, placed in turn on a plate that allows vertical and lateral translations. In here, according to the necessities of the experiment, all the additional equipment can be mounted, such as cryostats, *in situ* cells, liquid jets and so on.

The beam hitting the sample induces core-hole creation in the analyte atom and consequent emission of X-ray radiation. When detecting such radiation, it is possible to reduce the spectral broadening in the measurements by using an X-ray emission spectrometer for recording the fluorescence lines, instead of a solid state detector.

In fact, as further discussed in *Section 2.4*, an X-ray emission spectrometer provides an instrumental energy bandwidth that is on the order of the core-hole lifetime broadening.

X-ray emissions spectrometers can be distinguished between dispersive and non-dispersive geometries: the first category employs a crystal surface which is flat along the diffraction direction, while the second one, also called 'point-to-point focusing', is based on a bent optics along the diffraction direction. This kind of configuration has the goal to minimize the angular difference $\Delta\theta$ between the Bragg angle at any point of the crystal θ_i and the Bragg angle at the center of the crystal θ_B ($\Delta\theta = |\theta_i - \theta_B|$) [16].

At ID26, in both the experimental hutches, a point-to-point scanning multi-crystal spectrometer is employed, implementing a Rowland circle geometry.

Rowland geometry is a point-to-point focusing geometry based on the key concept of maintaining the X-ray emitting sample (defining the source volume), the analyzer crystals and a photon detector on a circle, the so-called Rowland circle.

The source position (0,0,0) of the spectrometer is defined by the position where the X-ray beam impinges onto the sample, identifying the source volume, which is given by the beam size, the orientation of the sample surface and the attenuation length of the emitted X-rays.

Since the beam cannot be easily moved, the source position (0,0,0) is fixed, while the analyzer crystals and the photon detector can move along the Rowland circle (Figure 2.11), characterized by a radius R_R, which is half the bending radius R_P of the crystal analyzer spherical shape (assumed to be identical for all the crystals).

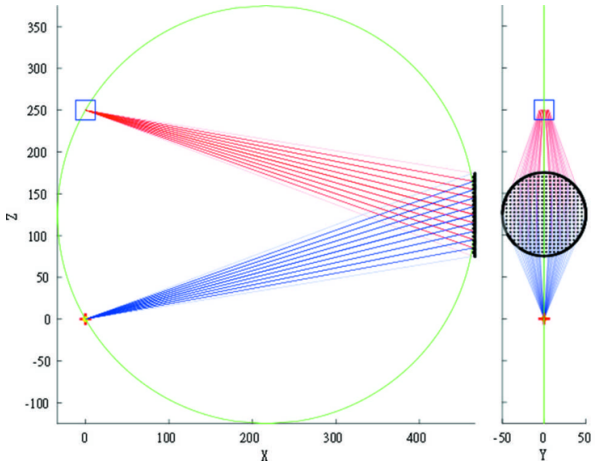

Figure 2.11: Source volume, analyzer crystal and detector placed on a Rowland circle [17].

The X-rays emitted from the sample reach the crystal analyzer and get diffracted following Bragg's law, which relates the energy of the radiation emitted from the sample (the fluorescence line) and the reflection angle θ_{B}:

$$n\lambda = 2dsin\theta_B \tag{2.9}$$

In Equation (2.9) n is an integer number, λ is the wavelength of the radiation (directly related to its energy) and d is the lattice spacing given by the lattice parameter a and the Miller indices h,k,l:

$$d = \frac{a}{\sqrt{h^2 + k^2 + l^2}} \tag{2.10}$$

According to Bragg's law, the wavelength of the radiation λ and the lattice spacing d fix the reflection angle θ_{B}, which is the so-called Bragg angle and is therefore dependent on the atomic number and the electronic transition of interest.

Hence, when changing the fluorescence line, the Rowland circle rotates around the sample and, accordingly, the Bragg angle changes, alongside with the crystals and detector positions (see Figure 2.12a).

Generally, to cover a large solid angle it is necessary to use more than one analyzer crystal in the sagittal plane: a rotation around the z axis is used to achieve an offset between the crystals along the y axis, and then each crystal defines a Rowland circle (Figure 2.12b).

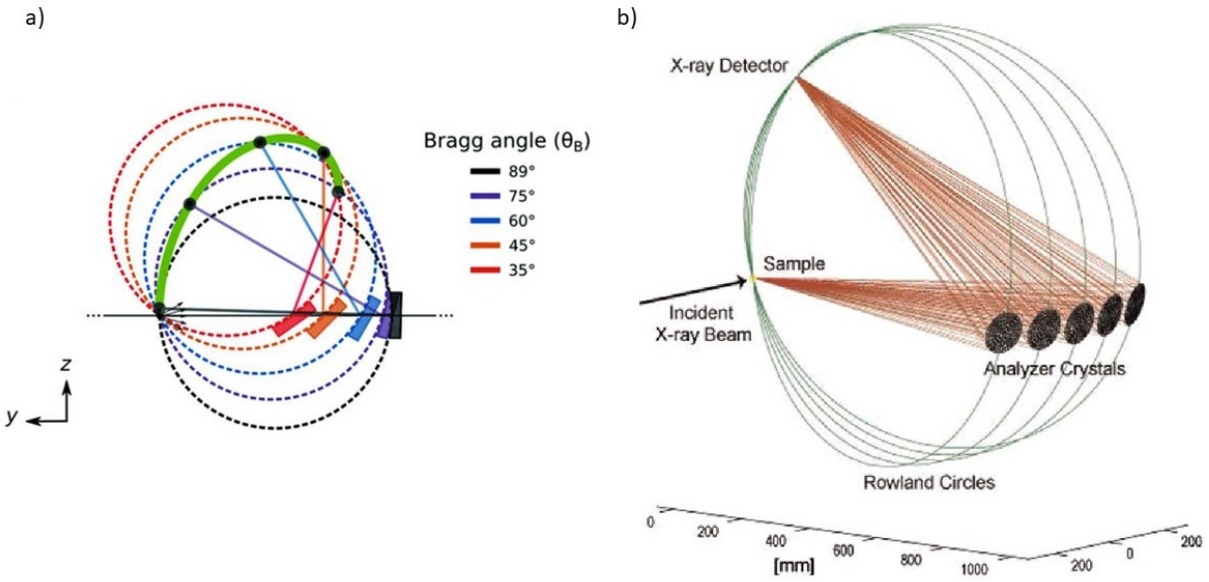

Figure 2.12: a) Motion of the crystal analyzer and the detector on the Rowland circle when changing the Bragg angle. Notice that the Bragg angle is the same from any point on the circle [16]; b) Multi-crystal analyzer layout composed by 5 crystals in the sagittal plane. Each crystal defines a Rowland circle [17].

As evident from Figure 2.12b, all the crystals' Rowland circles intersects in two points: the source volume and the detector position.

The so-positioned detector provides the smallest focal spot size in the scattering plane direction while a large spot size in the sagittal one, and provides a small detector surface in order to keep low the background signal given by the stray X-rays present in the hutch.

In particular, in the second experimental hutch a five-analyzer point-to-point scanning crystal spectrometer is employed, covering an angular range between 60° and 85°.

The five crystals are mounted on a spherical support with a 100 mm diameter substrate (Figure 2.13). The crystals are either Si or Ge with different cuts, since these two materials are the easiest single crystals to be produced, but new crystals are also being explored to increase the number of possible reflections achievable, in order to get closer to Bragg scattering at every energy. In our case five Ge(331) crystals were employed.

Figure 2.13: Five-analyzer crystals in experimental hutch EH2 at ID26 [18].

Plenty of translations are available to move the crystals. Each analyzer crystal can be aligned separately in order to get every crystal into the diffraction condition, *i.e.* such that the reflection goes into the detector.

Rotations and translations motors are required, since as the Bragg angle changes, the structure has to move either forward or backwards to stay on the Rowland circle.

Since typically the working energy ranges are in the order of 5 to 15 keV, especially at around 5 keV, it is not possible to ignore absorption in air, occurring between the 1 m distance between the sample and the crystals, and the similarly 1 m distance between the crystals and the detector.

For this reason, a bag filled with He with a pressure which is just above the atmospheric pressure is placed between the sample, the five crystals and the detector, with thin Kapton windows in correspondence of the exit and entering areas of the beam (see Figure 2.14).

With this kind of configuration, considering a 1 m distance and the presence of Kapton windows and He, the absorption at low energies is negligible compared to what would be absorbed without the helium bag.

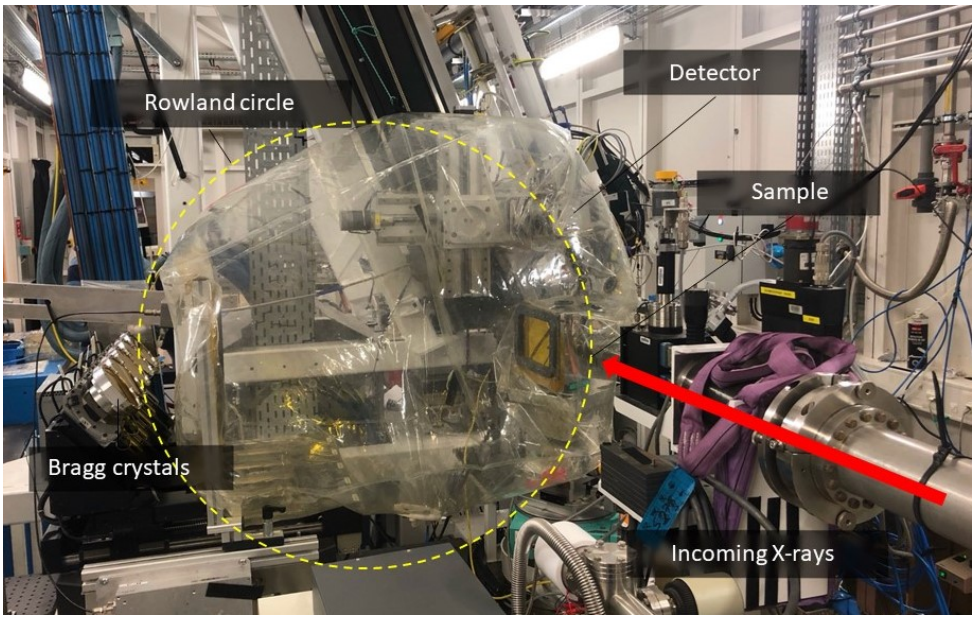

Figure 2.14: EH2 at ID26, He bag between the sample, the analyzer crystals and the detector.

In addition to the High Energy Resolution Fluorescence Detected (HERFD) experiments performed with the five-crystal spectrometer (and better described in *Section 2.4*), Total Fluorescence Yield (TFY) measurements can be carried out too in the same experimental hutch: in fact, there is a diode just above the crystals, visible in Figure 2.13, such that the two measurements (HERFD and TFY) can be performed at the same time. Generally, though, the TF diode can be employed with other purposes too, for example for compensation of concentration correction, or to facilitate the alignment of the sample.

Finally, as a detector an avalanche photodiode is often employed, a photon-counting detector based on the counting of the current pulses created for each incoming photon.

While providing poor energy resolution, the advantage of this detector lies in very high count rates, allowing for counting up to several millions counts per second, without losing linearity of the detector. In fact, the region of interest is the rising edge of the signal: if the detector is not linear there, artifacts would arise due to the non-linearity of the counting.

On the other hand, when the samples contain low concentrations of the analyte, very low background is needed, and the presence of some other chemical element affects the measurements (heterogeneous samples): in these cases, a solid state detector may be used, being an energy resolving detector.

A photon counting detector could be employed as well, but allowing an energy resolution

around 100-200 eV, it is not possible to distinguish between $K_{\alpha 1}$ and $K_{\alpha 2}$ lines. On the other hand, it is already possible to distinguish the metal of interest's K_{α} line from another metal's one, and if distinguishing between the two metals is enough, it is preferable to use a photon counting detector.

In conclusion, when a measurement is performed, the problem has to be approached from two sides: on one hand, which features do I expect to see and what energy resolution do I need in order to see them, and, on the other, how to implement that and if that is possible at all.

2.4. HERFD-XANES

As previously explained in *Section 2.1*, measurements of XAS spectra can be performed both in transmission and in fluorescence mode.

Initially, fluorescence detected XAS was developed in order to study dilute samples, since in such cases not enough photons are absorbed to produce a good XAS spectrum in transmission mode. Nevertheless, much higher potentialities lie in the employment of fluorescence-based detection.

Particularly regarding catalysis research, where it is desirable to study the catalyst under working conditions, XAS measurements are commonly chosen to investigate the electronic structure and local coordination by means of *in situ* experiments, where a detailed analysis of the XANES region provides information about the oxidation states and local geometry.

However, many interactions participate into the formation of the element-characteristic and complex XANES spectrum, and it is essential to completely resolve the spectral features in such region in order to carry out an appropriate analysis.

To correctly resolve the XANES region it is required a high energy resolution, which is correlated to a smaller energy bandwidth around the fluorescence line.

In this frame, High-Energy-Resolution Fluorescence Detected (HERFD) XAS offers a detection of the fluorescence line with an instrumental energy bandwidth of the order of the core hole lifetime broadening. Such broadening constitutes the main limit for improvement, since going further to smaller bandwidth in the emission detection would not further improve the signal to background ratio anymore [11].

High-energy-resolution XANES spectra can be acquired employing an X-ray emission spectrometer based on perfect-crystal Bragg optics, such as the one implemented at ID26 and described in *Section 2.3*. HERFD-XAS requires tunable and high-brilliance X-ray

radiation, available at synchrotron facilities, and provides a spectral sharpening that reveals features previously unobserved by means of transmission detection [19].

Moreover, another detection possibility is represented by Total Fluorescent Yield detection, which is based upon collecting the signal directly emitted from the sample, without exploiting the Bragg crystals. Such solution is possible at ID26, as explained in *Section 2.3*, although energy resolution is considerably lower.

In order to appreciate the energy resolution difference between the two detection techniques, Figure 2.15 offers a comparison in the case of CeO_2 at the L_3 edge.

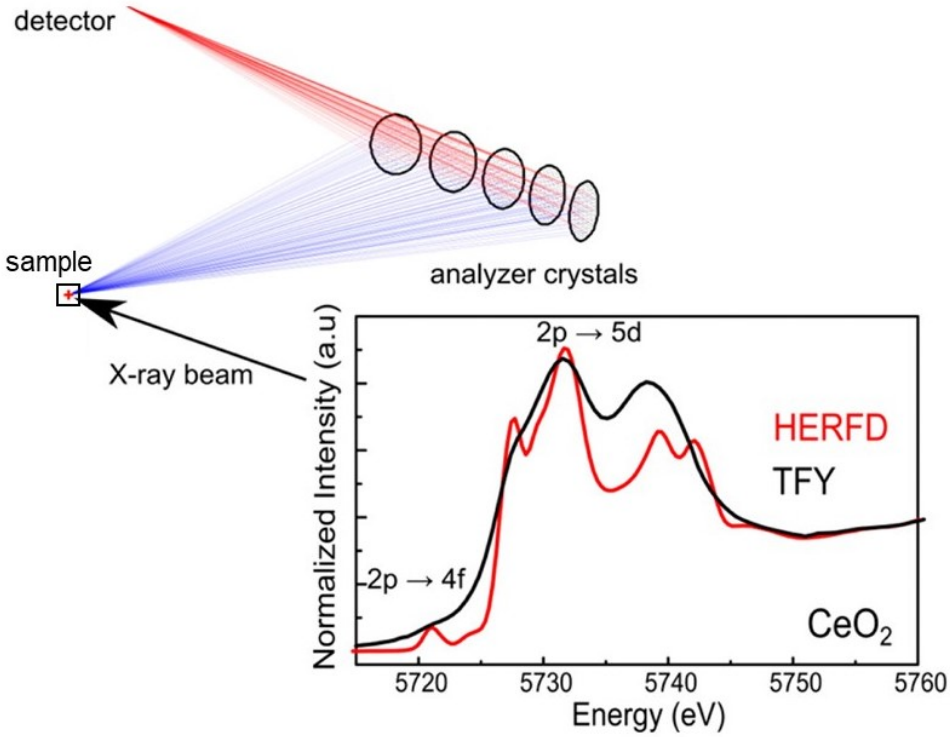

Figure 2.15: Comparison between HERFD and Total Fluorescence Yield (TFY) XANES spectra, acquired at the L_3 edge of ceria [5].

The high-resolution XANES allows to resolve the pre-edge region, where the peak associated to quadrupole-allowed transitions from *2p* to *4f* levels is visible only by means of HERFD. Such feature is hidden by the lifetime broadening in the transmission spectrum, while on the contrary, in HERFD experiments the incident flux and the efficiency of the spectrometer are able to probe even the weak quadrupole transitions, that in this case appear as clearly separated from the white line.

Similarly, the fine structure of the *5d* band is resolved, accurately distinguishing the four peaks in the near edge region associated to *2p* to *5d* dipole-allowed transitions. More

specifically, the white line in proximity of the edge is associated to Ce^{3+}, while higher-energy peaks are related to both transitions from the Ce *2p* to *5d* shell with final electronic configuration $2p4f^{0}5d^{1}$, with no electrons in the *f* shell, and to excitation from the *2p* to *5d* shell along with an electron being excited from the O *2p* shell to the Ce *4f* shell, creating a hole in the valence band (final state $2p4f^{1}5d^{1}v$, where *v* represents the hole) [20].

Another advantage of HERFD XAS is that the data treatment is relatively straight forward: absorption scans of the fluorescence lines are recorded and plotted as a function of the energy, normalizing the spectra using the absolute signal area calculated by means of the trapezoidal rule through Python scripts [21].

In short, HERFD measurements performed at synchrotrons with high incident flux exploit the elevated count rates to produce high resolution spectra, but special attention must be given to self-absorption issues affecting fluorescence-detected data.

2.4.1. Self-absorption in fluorescence-collected data

As explained above, HERFD-XAS provides excellent data quality, both yielding sharper spectral features and suppressing the background originating from unwanted X-ray events such as those arising from the matrix.

However, a meaningful problem concerning this technique stems from the usage of fluorescence detection: the latter is affected by spectral distortions due to incident beam self-absorption that can only be reduced but never fully removed.

In the case of thick analyzed samples the fluorescence signal does not correctly mirror the absorption coefficient: in fact, when μ increase, *e.g.* in correspondence of an absorption edge, the penetration depth decreases, leading to less atoms contributing to the fluorescence signal and therefore reduced counting efficiency [14].

Self-absorption is one of the main problems concerning data collected in fluorescence mode, especially at lower energies and for samples showing high concentrations of the absorber element. Distortions appear in the XAS spectrum, due to limited penetration of the X-ray beam into highly absorbing samples [22], as a function of the sample composition and geometry, namely its effective atomic number, density, thickness, and the X-ray photon energy.

To minimize this undesired effect it is necessary to reduce the interaction of the incoming X-rays with the analyte until the X-rays penetration does not significantly change when the incoming energy is tuned through an absorption edge of the analyte: a way to achieve this is to decrease the total absorption of the sample by making it optically thin, for

example, or to decrease the absorption of the analyte over the total absorption ratio, obtained for example when the analyte is placed in a matrix of high Z elements.

Nevertheless, it might not be always possible to minimize self-absorption when the sample is required to remain unaltered or in a characteristic size above the absorption length, and while sometimes this could not critically compromise the data analysis if all spectra are affected by the same degree of distortion, it is in principle possible to reduce the error by including self-absorption into the analysis.

An exact correction for self-absorption can be arduous and not always possible, since a precise knowledge of the sample's composition, homogeneity, and morphology is required, but nonetheless something in the data analysis can be improved to take into account this physical phenomenon. The fluorescence signal can be evaluated through the approximated Equation (2.11) [23] with the incident energy E, fluorescence energy E_f and the geometry shown in Figure 2.16

$$f_{SA}(x) = kx\frac{1 - e^{-\beta(x+\alpha)}}{x + \alpha} \tag{2.11}$$

where:

$$x \propto \mu(E); g = \frac{sin\theta}{sin\phi}; \alpha = \mu_{\text{else}}(E) + g\mu_{\text{tot}}(E_f); \beta = \frac{d}{sin\theta}$$

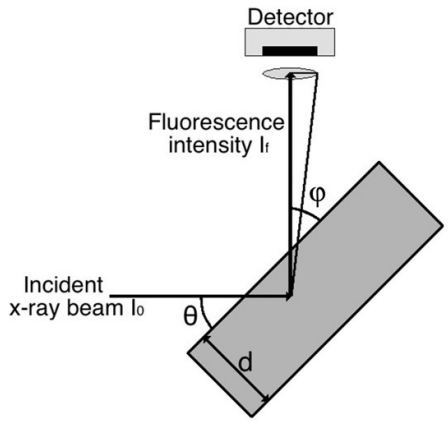

Figure 2.16: Geometry of the experimental setup in a photon-in/photon-out experiment [23].

The fluorescence signal is therefore dependent on the analyte absorption coefficient μ(E) and on the sample and matrix absorption μ_{tot} and μ_{else}, where the absorption coefficient of the sample is the sum of the coefficient of the element of interest ('absorber') and all other

elements: $\mu_{tot} = \mu_{abs} + \mu_{else}$. Only the absorber subshell, that means the edge of interest, that gives rise to the recorded emission line is considered in the absorption coefficient of the absorber.

The angles between incoming and outgoing beam and the sample surface θ and ϕ, as shown in Figure 2.16, are also considered in the expression, alongside with other parameters lumped together in the factor k, including subtended solid angle, fluorescence yield, incoming photon flux, and spectrometer detection efficiency.

The equation is approximate because variations of the angle ϕ across the solid angle subtended by the crystal analyzer surfaces are neglected and a flat sample surface is assumed.

The equation for the fluorescence signal written as in (2.11) cannot be solved exactly for μ(E), but even though it is always desirable in an experiment to know the photoelectric absorption coefficient, it might not be strictly necessary, since it is possible for meaningful considerations to be extrapolated from distorted spectra.

As it is explained by Lafuerza et al. [24], instead of trying to remove the distortion from the spectra affected by self-absorption, it is possible to use the equation to fit a spectrum onto another spectrum that is distorted due to self-absorption, and this is the procedure we employed to manipulate our data.

By performing a linear combination, the reference spectra are already distorted by self-absorption, leading to not successful results, while, on the other hand, it is possible to include self-absorption effects by fitting with α and β as fit parameters, with the constrain that all spectra must be normalized to the spectral area: this way, by deliberately distorting the spectra even more to take into account self-absorption, a far better solution is provided.

2.5. Operando cell

In order to measure HERFD-XANES spectra at different temperatures and under gas flow, the powder samples were placed in a cell designed and produced at ESRF by the Sample Environment.

It is engineered specifically to study samples under gas flowing, provided with a gas inlet and outlet at both sides of the cell, such that the powder is tightly packed inside the small pit and the gas is flown through it (see Figure 2.17). To prevent the powder from going into the pipes, quartz wool is placed at the edges in correspondence of the inlet and outlet

holes.

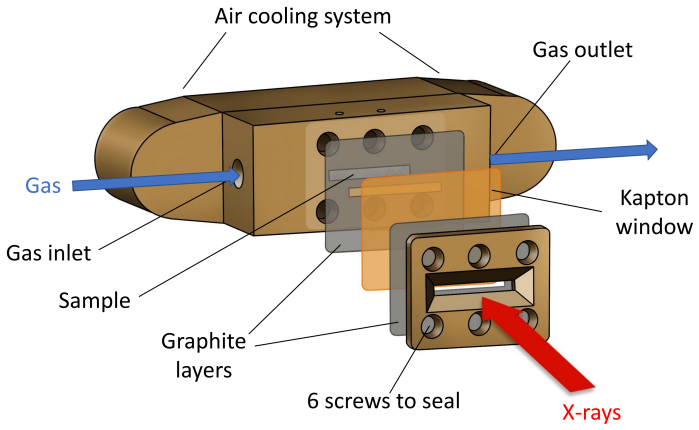

Figure 2.17: Schematic layout of the cell.

A 25 μm-thick Kapton window is used to keep the sample in place into the cell while minimizing the absorption of the incoming beam and, in order to avoid sample dispersion, 200 μm-thick graphite layers are placed before and after the Kapton layer acting as a gasket, leaving at the same time the window onto the sample uncovered to avoid ulterior beam absorption, as depicted in Figure 2.17.

Moreover, such cell is able to reach high temperatures, more precisely it can be heated up to 400°C, although we went up to 300°C maximum to avoid burning of the Kapton layer. The cell is equipped with both air and water cooling systems, but air cooling alone proved to be enough for cooling down from 300°C.

Such cell was placed in correspondence of the X-ray beam rotated by an angle of 45° with respect to the latter. A picture of the powder CeO_2 sample placed inside the cell mounted onto the described experimental setup (*Section 2.3*) is provided in Figure 2.18.

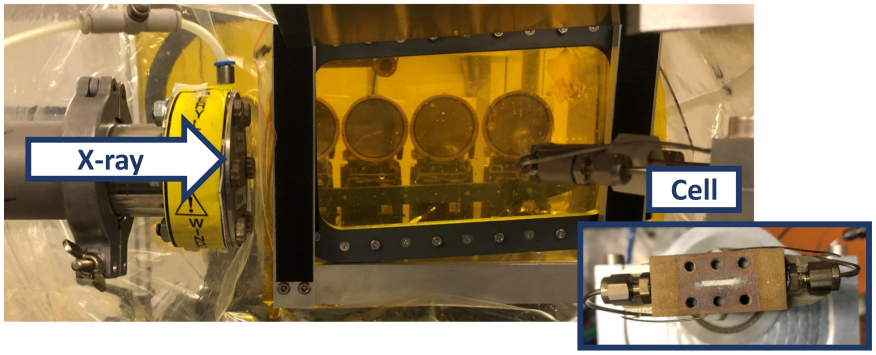

Figure 2.18: Experimental setup at ID26. The X-ray beam is sent onto the cell containing the sample, and the consequently emitted radiation is collected and focused by the five analyzer crystals onto the detector.

2.6. Measurement protocols

For all the samples the measuring procedure was identical:

- At first, we proceed with the acquisition of an initial state, under pure He flow. Being helium an inert gas, we expect no perturbations on the Ce XANES spectra, with Ce in the oxidized state of Ce^{4+}.
- Then, we reduce the sample by flowing 3%H_2 in He and acquire the corresponding spectrum.
- After having reduced the sample, we oxidize it again by flowing 10%O_2 in He and measure.
- Finally, we acquire a final state under no gas condition, where we expect to recover a situation equal to the initial one.

The protocol was implemented using a mass flow control system that allowed to switch from one gas flow to the other.

For safety purpose, a quick He flush was done between the H_2 and the O_2 flow, and then again after the O_2 flow as well, in order to reach the no gas conditions.

In order to avoid burning the sample with prolonged X-ray exposition, the acquisition time was kept at 10 s for each scan in the 16 bunches mode of the synchrotron (corresponding to a current of 73 mA in the ring). This measurement settings allowed a whole protocol going from the initial state to the final one to be completed in more or less 7 hours.

For each sample the same protocol was repeated at 50°C, 200°C and 300°C.

3 | Results and data analysis

The present chapter is dedicated to reporting the experimental measurements resulting from the four CeO_2-based powder samples that we analyzed:

- Commercial CeO_2
- Lab synthesized CeO_2
- 1%Pt/CeO_2
- 5%Pt/CeO_2

Starting from a discussion about the samples' structure, additional details are provided: in fact, aside from the commercial sample that was synthesized by Alpha Aesar, the remaining samples were synthesized at the Ceramic Synthesis and Functionalization Laboratory by our collaborators from the mixt unit CNRS/Saint-Gobain. They have synthesized the three samples following the same procedure for each of them [25] and have subsequently characterized the Pt/CeO_2 structure by performing XRD, HAADF-STEM, SAED and NAP-XPS studies, whose results are reported here in the first section.

Subsequently, in *Section 3.2* it is provided a description of how we corrected self-absorption phenomena afflicting the experimental data acquired from the lab synthesized CeO_2 sample, while the remaining *Section 3.3* and *Section 3.4* report the XANES spectra of the pure CeO_2 and the Pt/CeO_2 samples respectively, under the different gaseous environment and at different temperatures.

3.1. Pt/CeO_2 sample characterization

As it is better discussed in *Chapter 4*, adding platinum to the CeO_2 structure strongly influences its chemical properties, creating a complex and nanostructured catalysts whose surface behavior strongly differs from single-crystal systems. At the same time, it has been observed in many studies that ceria redox properties can differ even according to the crystal structure and size, showing different behaviors when going to the nanoscale.

Characterization studies are essential for better understanding the chemical properties of a system, as they provide insight into the structure and size of the sample prior to spectroscopic measurements. This information can be used to gain further details about the surface structure.

Therefore, additional analysis about the samples' structure are presented below, as discussed by our collaborators Meunier et al. [15].

Before performing HERFD spectroscopic measurements at ID26, our collaborators acquired XRD patterns along side with HAADF-STEM and SAED images to look carefully at the surface of the Pt/CeO_2 samples.

X-ray diffraction patterns of the as-synthesized $5\%Pt/CeO_2$ sample and of the spent catalyst are shown in Figure 3.1. Such patterns indicate the presence of cubic ceria only (space group $Fm\bar{3}m$): all diffractograms can be, in fact, attributed to phase-pure cerium oxide, while no diffraction peaks from neither metallic Pt nor platinum oxide are visible, indicating a high platinum dispersion.

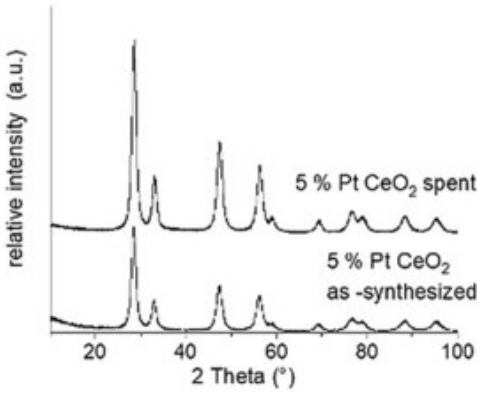

Figure 3.1: XRD pattern of the spent catalyst and of $5\%Pt/CeO_2$ as-synthesized sample (study performed by Meunier et al. [15])

Using the Scherrer's equation (2.8) for the diffraction peak located at $2\theta = 29°$, the crystallite size of ceria particles is found to be equal to 7.4 nm.

On the other hand, HAADF-STEM was performed on the same sample, producing the images visible in Figure 3.2, which provide a good contrast between the platinum nanoparticles and ceria. Ceria crystallites are agglomerated and characterized by an irregular shape, therefore various crystalline planes are exposed on the surface. Pt nanoclusters, moreover, can be spotted on the surface in such HAADF-STEM images, allowing to state

that the samples contain mostly Pt nanoparticles of sizes comprised between 0.6 and 1.5 nm, corresponding to a platinum dispersion of about 100%. Also, a few single Pt atoms can be observed (Figure 3.2b).

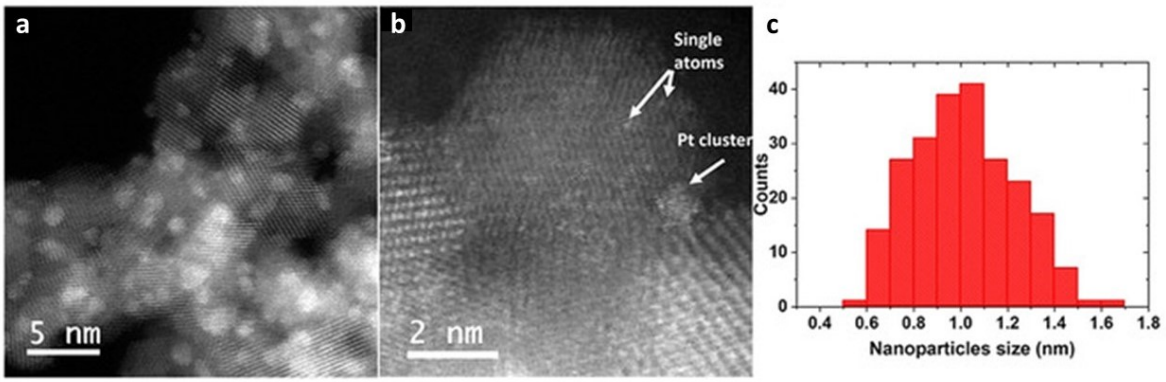

Figure 3.2: Representative HAADF-STEM images of the Pt/CeO_2 catalyst (a, b) and the corresponding Pt particle sizes distribution (c) [15]

Furthermore, the high dispersion of platinum species was once again confirmed by SAED analysis, which show only peaks corresponding to ceria: the absence of Pt diffraction peaks in the reduced sample's images (Figure 3.3) indicates an amorphous nature of the platinum phase.

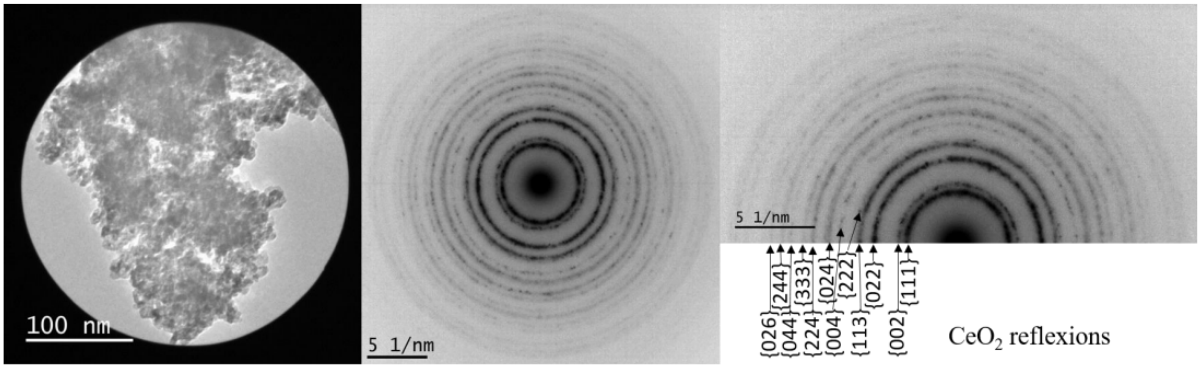

Figure 3.3: Selected Area Electron Diffraction (SAED) on the reduced sample ([15], SI).

On the other hand, when looking at the SAED images for the spent catalyst (Figure 3.4), some spots belonging to crystalline platinum appear, indicating that crystalline metallic Pt is present: this is a result of the crystallization of platinum happening during the reaction processes involving the sample, although an overall similar dispersion of Pt is maintained.

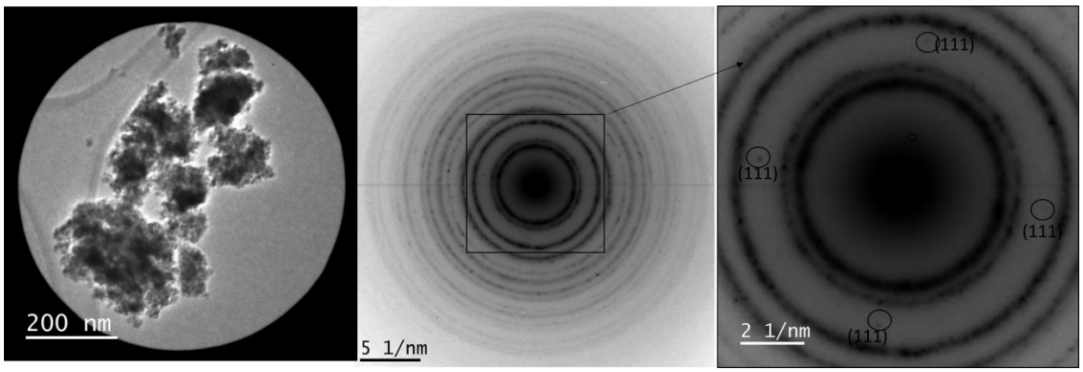

Figure 3.4: Selected Area Electron Diffraction (SAED) on the spent sample ([15], SI).

At the same time, it is not possible to ascertain the presence of oxidized Pt clusters, but the possibility that these latter could have been reduced in the high vacuum or under the electron beam of the electron microscope cannot be excluded.

It is relevant to know the oxidation state of the Pt nanoclusters and single atoms formed onto the ceria support, for this reason, *in situ* or *operando* techniques are required to clarify the nature and the structure of the catalytic active Pt species. In fact, the state of Pt single crystals and nanoparticles has been proposed to change depending on the experimental conditions, requiring surface science and XAS techniques to investigate it.

Meunier et al. [15] proposed that both metallic and oxidized Pt are present in comparable amounts on the surface of ca. 1 nm nanoparticles, based on the results of their analysis. They performed *in situ* NAP-XPS on the samples after that these had been previously reduced *ex-situ*, in order to keep the measurements coherent with the previous HAADF-STEM ones. The results shown in Figure 3.5 confirmed the high modifications of Pt oxidation state upon varying the gaseous environment in the reaction chamber: under O_2 flow a mixture of Pt^0, Pt^{2+} and Pt^{4+} is present, and when adding CO into the chamber Pt^0 concentration increases at the expense of Pt^{4+}, leaving Pt^{2+} unaffected. When only CO is flown, oxidized platinum disappears, leaving Pt^0 species only, and finally, when O_2 is once again added into the chamber, a new mixture of the three oxidation states is shown, different from what was previously found under the same gaseous environment. This latter experimental observation reveals a history-dependent behavior of Pt oxidation state, that changes with the sequence of treatments.

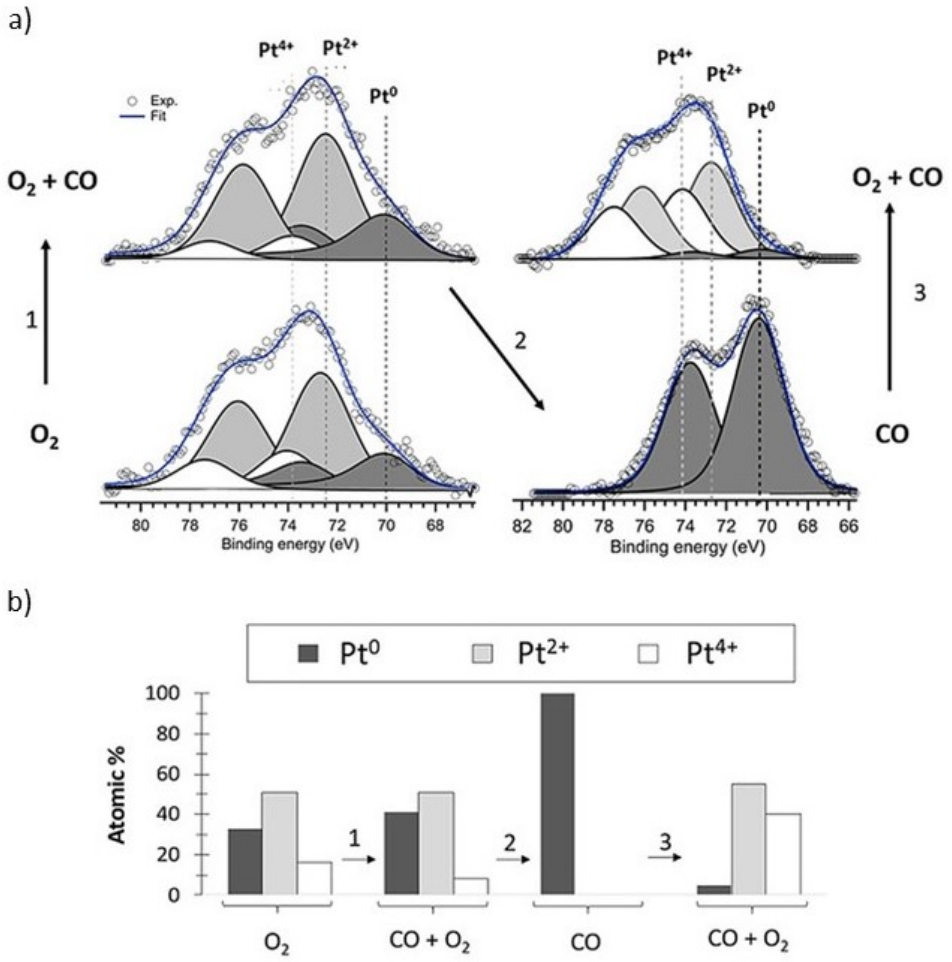

Figure 3.5: a) NAP-XPS Pt 4f core levels measured over the Pt/CeO_2 sample at room temperature under O_2, O_2+CO, CO, and then CO+O_2 again. b) Corresponding distribution of Pt oxidation states under the different gas compositions [15].

The fraction of Pt remaining oxidized under CO could be attributed to the smallest clusters present, that turn out to be more difficult to reduce because of the stronger interaction with the support, and this could lead to oxygen supply from the support to the reduced platinum particles, resulting in an increase in the catalytic performance.

In the end, although additional studies would be required in order to determine the exact structure of the metallic and oxidic Pt phases, we can say that the dual oxidic-metallic nature of supported Pt catalysts is complex and evolves under reaction conditions, and we can conclude that the simultaneous presence of both the states of Pt enables a synergy between the two phases.

3.2. Starting material comparison and self-absorption evaluation

In order to analyze the data, it is necessary to first compare the XANES spectra of the four different starting materials (CeO_2 commercial, CeO_2 lab synthesized, 1%Pt/CeO_2 and 5%Pt/CeO_2) in relation to each other, in order to understand the starting point of the experiment.

The comparison is reported in Figure 3.6, showing the XANES spectra acquired under helium flow at 50°C.

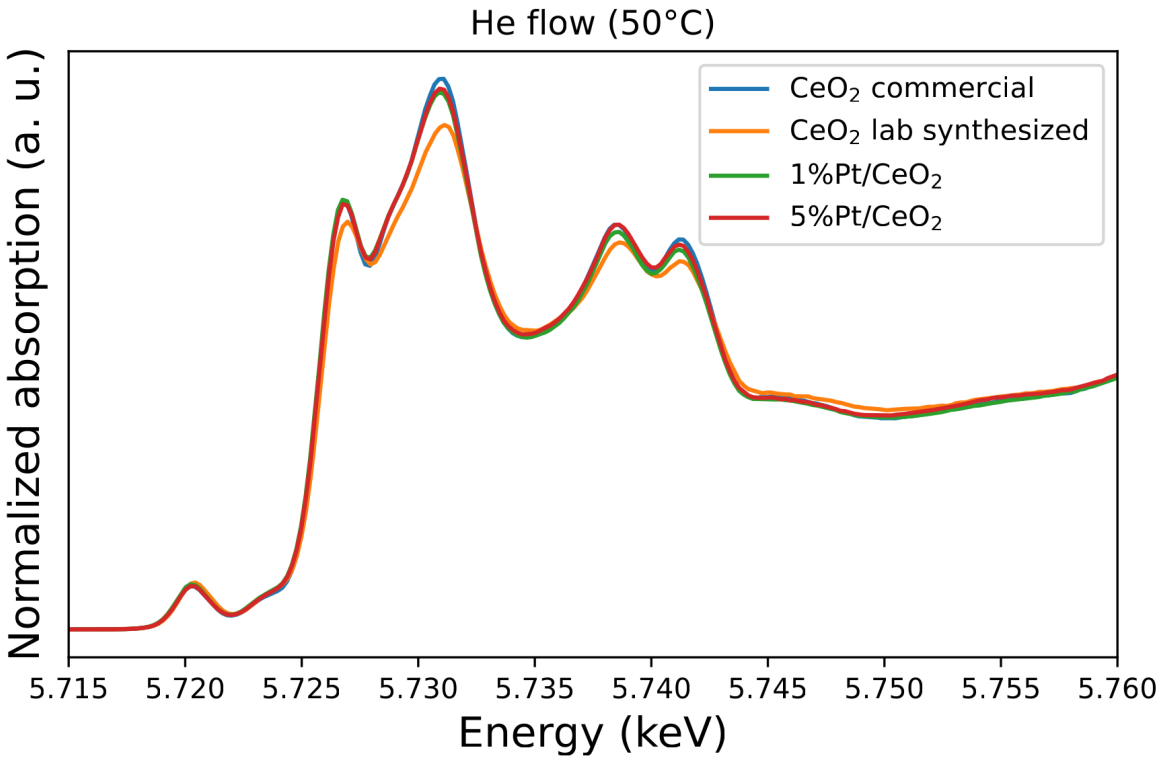

Figure 3.6: XANES spectra of the four samples (CeO_2 commercial, CeO_2 lab synthesized, 1%Pt/CeO_2 and 5%Pt/CeO_2) acquired under helium gas flow at 50°C.

As visible from Figure 3.6, lab synthesized CeO_2 shows smaller intensity in the characteristic four peaks with respect to the other samples. Being helium an inert gas, we expect the samples to be unaffected by the presence of the gas and all the four samples to mainly contain Ce^{4+} species at 50°C, therefore we would expect to see an overlap of all the samples' spectra in the near-edge region. Therefore it is important to ascertain the nature of such spectral distortions: whether these are caused by the chemical nature of the sample

or by other physical phenomena, more specifically self-absorption.

In order to understand this, self-absorption investigations were carried out, following the procedure described in *Subsection 2.4.1*, by fitting the commercial CeO_2 spectrum – considered not affected by self-absorption distortion – onto the lab synthesized CeO_2 spectrum. Results are shown in Figure 3.7.

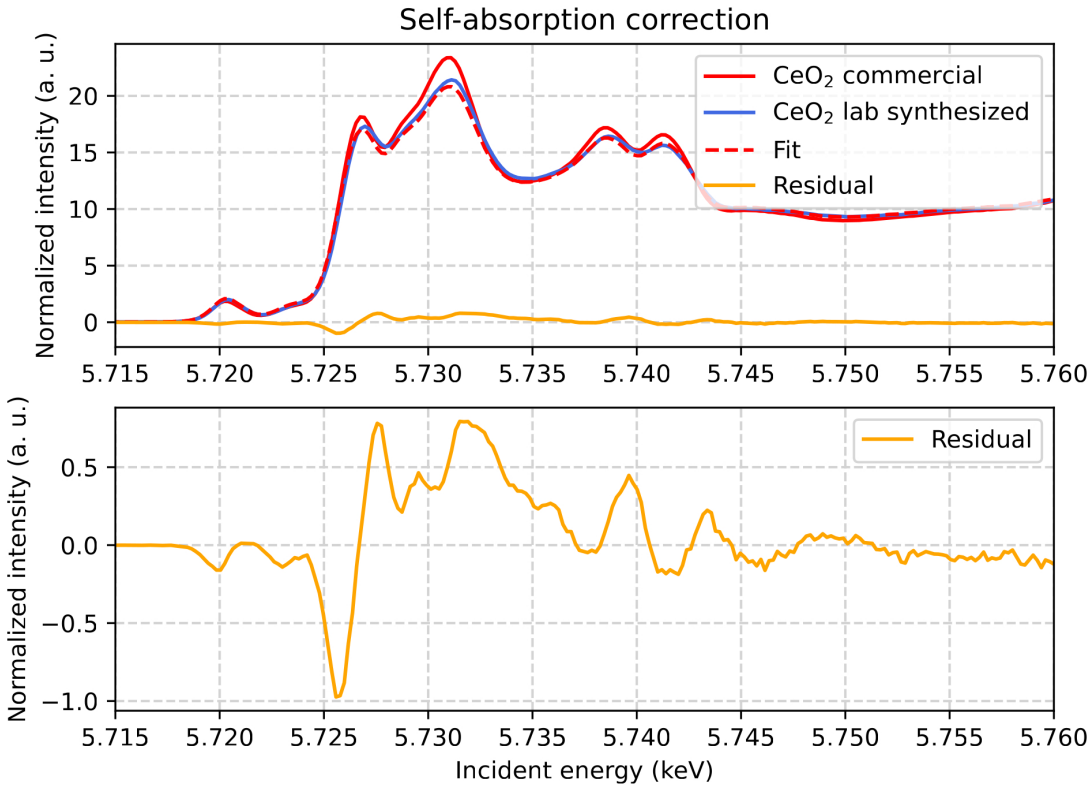

Figure 3.7: Self-absorption evaluation for the lab synthesized CeO_2 spectrum: self-absorption distortion is applied to the non-distorted commercial CeO_2 spectrum, which is subsequently fitted onto the lab synthesized CeO_2 spectrum affected by self-absorption.

The results depicted in Figure 3.7 were obtained by taking a sample's thickness d of 1 mm and a fixed angle $\phi = 45°$, and finding the best fit upon varying k, θ, μ_{tot}, and μ_{else}. The systems finds the best values for k, θ, μ_{tot}, and μ_{else} corresponding to the best fit for the fluorescence signal distorted by the effects of self-absorption, represented by the dashed red line in the picture, and calculated by means of Equation (3.1), which is equivalent to Equation (2.11) but explicitly written as a function of the fitting parameters mentioned above.

$$f_{SA}(x) = kx\frac{1 - e^{-\frac{d}{sin\theta}(x+\mu_{else}(E)+\frac{sin\theta}{sin\phi}\mu_{tot}(E_f)}}{x + \mu_{else}(E) + \frac{sin\theta}{sin\phi}\mu_{tot}(E_f)} \tag{3.1}$$

A good fit was found, consequently confirming self-absorption as the main cause of the observed distortion, affecting mainly the near-edge region (5.72-5.74 keV) of the spectrum. However, such distortion does not compromise our data analysis, since all lab synthesized CeO_2 spectra are affected by the same degree of distortion. In the following sections only spectra acquired from the same sample are compared, making the absolute distortion irrelevant when CeO_2 spectra from the same lab synthesized sample are compared one with respect to the other, showing a null relative distortion.

After this brief section aimed at explaining how we interpreted the intensity shifts in lab synthesized CeO_2 spectral features (Figure 3.6), the following paragraphs are finally dedicated to a comparison and analysis of the acquired data, overcoming the distortions due to self-absorption phenomena and investigating the 'real' spectral changes attributed to electronic transitions.

3.3. CeO_2

In this section and in the next one the results of the HERFD-XAS measurements performed at ID26 are presented, distinguishing between the two cases: pure ceria and ceria with the addition of platinum (*Section 3.4*).

For all the samples, three plots were generated, each corresponding to a different acquisition temperature of 50°C, 200°C, and 300°C. In each graph the four XANES taken at the L_3 edge of Ce under the four gaseous environments described in *Section 2.6* are plotted together, that is Ce under He flow (initial state), H_2 flow (reduced state), O_2 flow (oxidized state) and no gas flow (final state). All spectra were acquired in the energy region between 5.715 keV and 5.815 keV and normalized to the total area.

As previously explained, in the case of pure ceria we analyzed two samples: one commercial and one lab synthesized. Starting from the commercial CeO_2 sample, below is reported in Figure 3.8 a comparison between the XANES spectra acquired at 50°C under the four gases, zoomed in the region of interest.

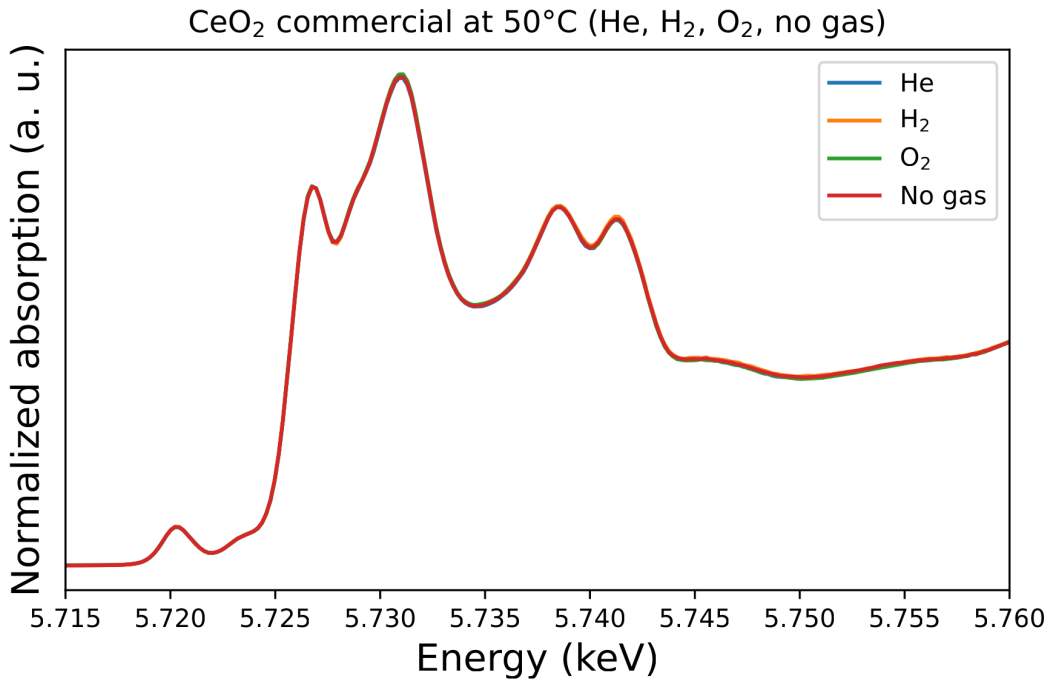

Figure 3.8: XANES spectra of the commercial CeO_2 sample, acquired at 50°C under helium, hydrogen, oxygen and no gas flow.

As it is immediately visible, no variations in the spectra are noticed when switching from one gas flow to the other, in particular we would expect some spectral changes when flowing hydrogen onto the sample, because of the reduction of some Ce sites. This does not happen, indicating that all Ce atoms are in the oxidized state Ce^{4+}, characterized by the four peaks in the 5d band structure and by the single peak in the pre-edge region, corresponding the single spin state (s = 0), as better discussed in *Section 1.2*.

The same measurements repeated at 200°C and 300°C produced the results shown below in Figure 3.9 and Figure 3.10.

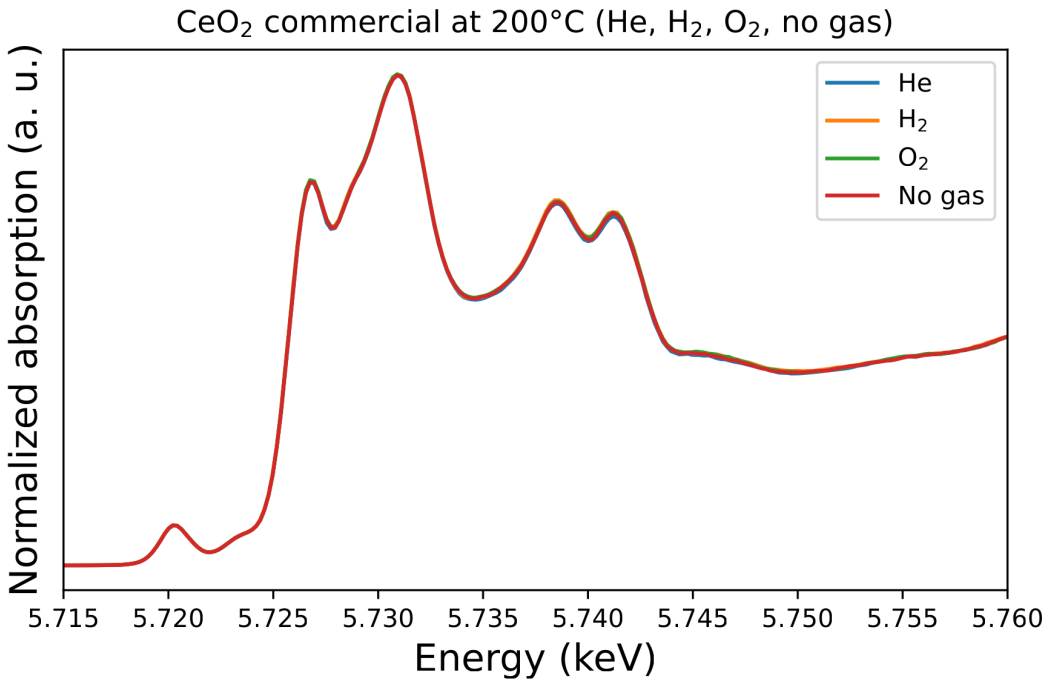

Figure 3.9: XANES spectra of the commercial CeO_2 sample, acquired at 200°C under helium, hydrogen, oxygen and no gas flow.

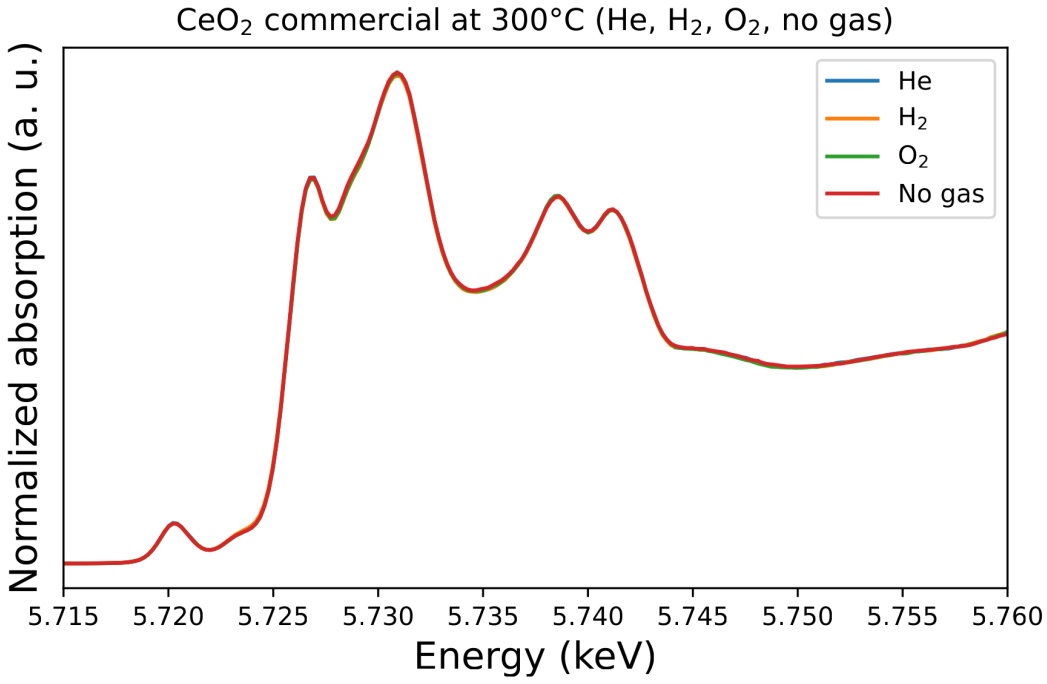

Figure 3.10: XANES spectra of the commercial CeO_2 sample, acquired at 300°C under helium, hydrogen, oxygen and no gas flow.

Once again, all spectra overlap indicating no reduction of Ce and showing the characteristic spectral features of Ce^{4+}.

The same measurement procedure was applied on the lab synthesized CeO_2 sample, producing the spectra reported in Figure 3.11, Figure 3.12, and Figure 3.13 for the three different temperatures.

Similarly to the previous case, no spectral changes are visible when flowing hydrogen onto the sample at any of the considered temperatures.

These results imply that temperatures up to 300°C are not enough to promote the interaction of hydrogen with the sample, resulting in all similar oxidized Ce^{4+} spectra acquired in such working conditions. If we want to reduce ceria it is necessary to reach higher temperatures or, as it is better explored in the next sections, to consider the addition of a noble metal to promote Ce^{4+} reduction to Ce^{3+} when repeating the experiment at the same temperatures.

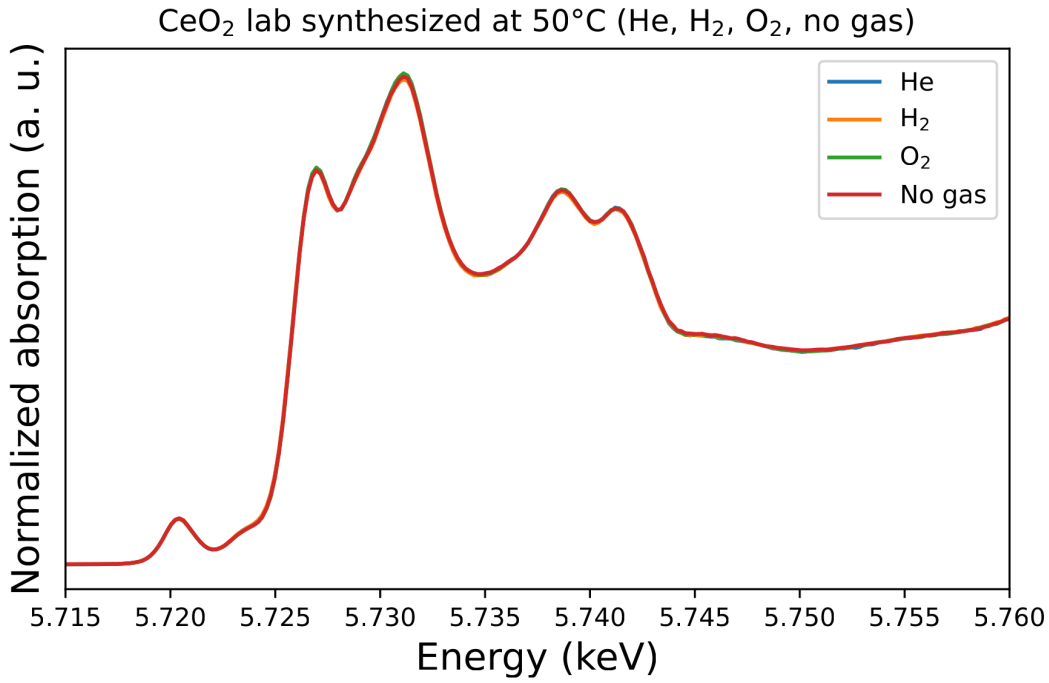

Figure 3.11: XANES spectra of the lab synthesized CeO_2 sample, acquired at 50°C under helium, hydrogen, oxygen and no gas flow.

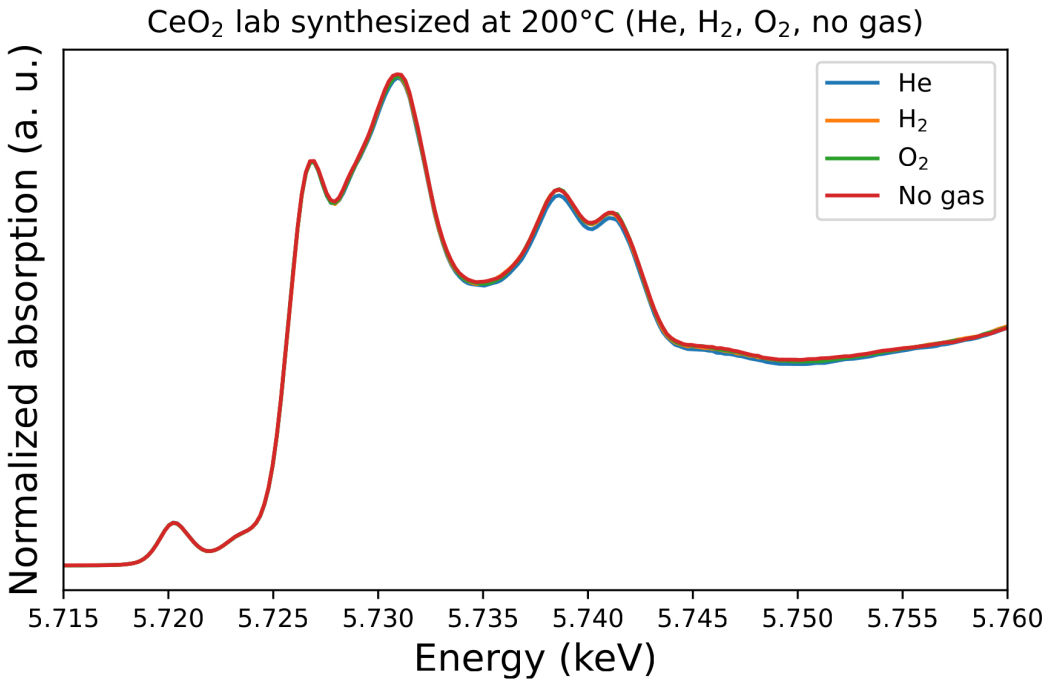

Figure 3.12: XANES spectra of the lab synthesized CeO_2 sample, acquired at 200°C under helium, hydrogen, oxygen and no gas flow.

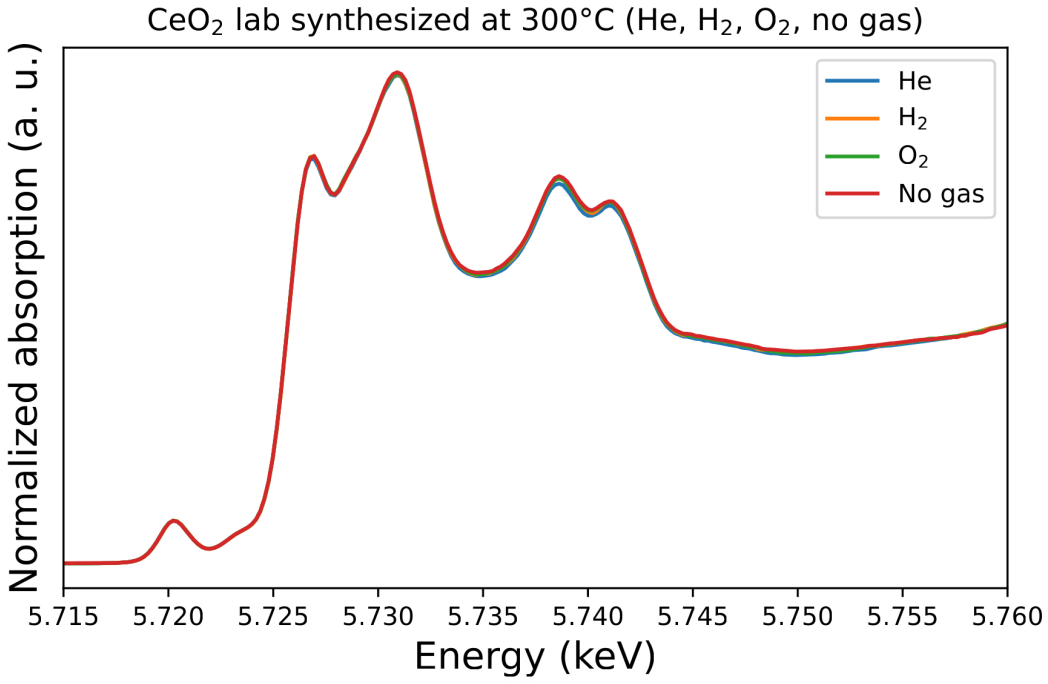

Figure 3.13: XANES spectra of the lab synthesized CeO_2 sample, acquired at 300°C under helium, hydrogen, oxygen and no gas flow.

3.4. Pt/CeO_2

As explained before, we chose to add platinum onto the structure in order to exploit the synergy arising between the noble metal and the support to obtain a reduction of the ceria sample without going to temperatures above 300°C.

We first analyzed a CeO_2 sample with the addition of 1 wt % of Pt and then we moved to analyze the one with 5 wt % of Pt, obtaining very different behaviors with respect to the previous case (shown in *Section 3.3*).

When adding platinum to the system, as expected, the reduction of the ceria sample is reached maintaining the same working conditions we used in the pure ceria case.

In particular, considering the $1\%Pt/CeO_2$ sample, we observe at 50°C very small changes around 5.724 keV, hardly visible without zooming in (Figure 3.14), while upon rising the temperature up to 200°C and 300°C new spectral features appear, clearly visible in Figure 3.15 and 3.16.

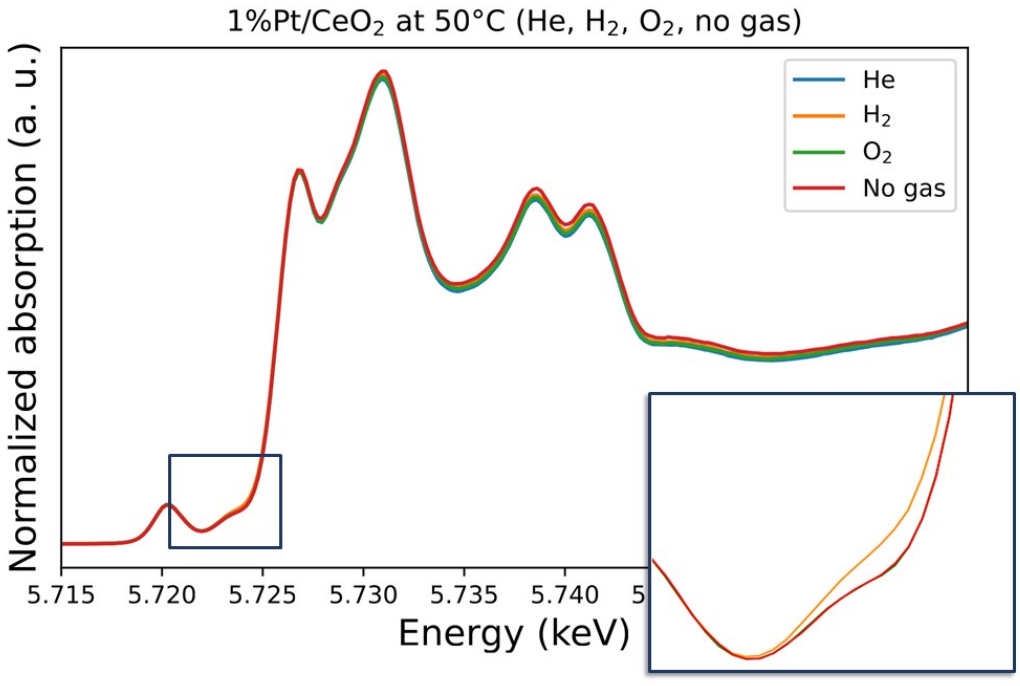

Figure 3.14: XANES spectra of the $1\%Pt/CeO_2$ sample, acquired at 50°C under helium, hydrogen, oxygen and no gas flow. Inset shows the magnified region around 5.724 keV.

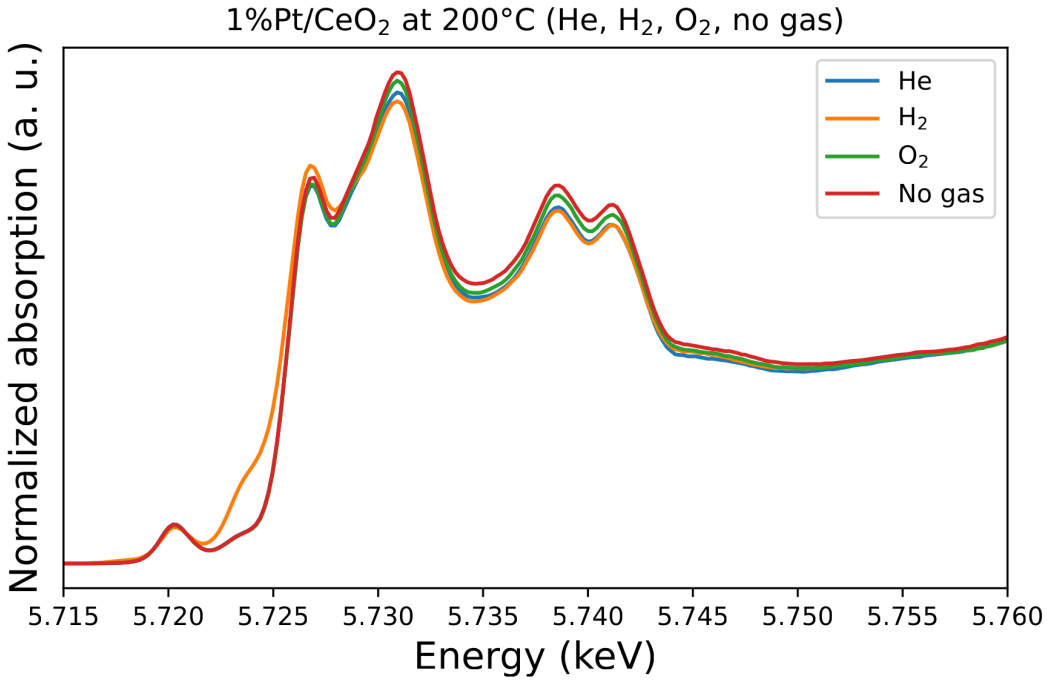

Figure 3.15: XANES spectra of the 1%Pt/CeO_2 sample, acquired at 200°C under helium, hydrogen, oxygen and no gas flow.

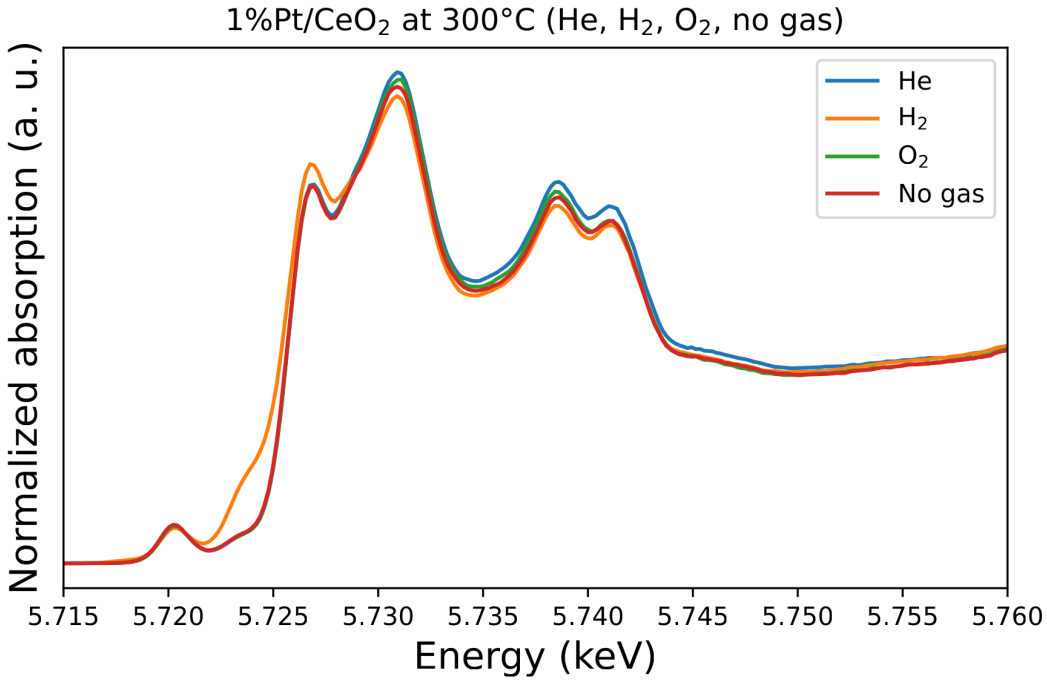

Figure 3.16: XANES spectra of the 1%Pt/CeO_2 sample, acquired at 300°C under helium, hydrogen, oxygen and no gas flow.

Upon introducing hydrogen onto the sample, a large peak was observed at 5.724 keV, suggesting a modification of the cerium electronic structure.

At the same time, similar changes occur when adding 5%Pt on CeO_2, with the major difference that a prominent shoulder is now showing up already at a temperature of 50°C, as visible from Figure 3.17.

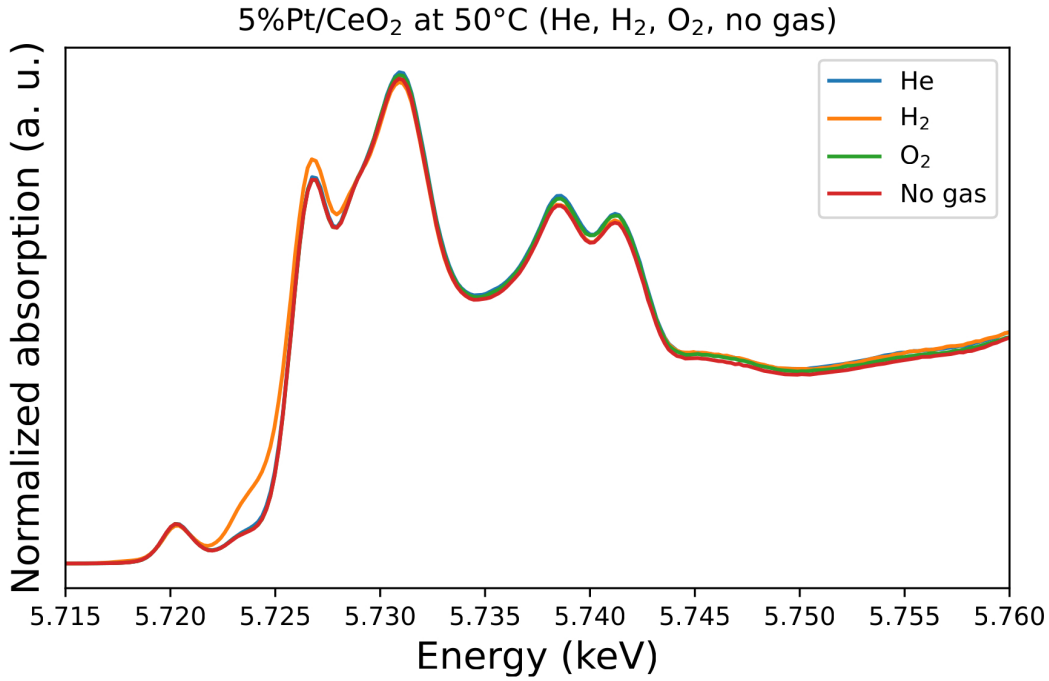

Figure 3.17: XANES spectra of the 5%Pt/CeO_2 sample, acquired at 50°C under helium, hydrogen, oxygen and no gas flow.

Then, upon increasing the temperature up to 200°C and 300°C, we obtain the measured spectra shown in Figure 3.18 and 3.19.

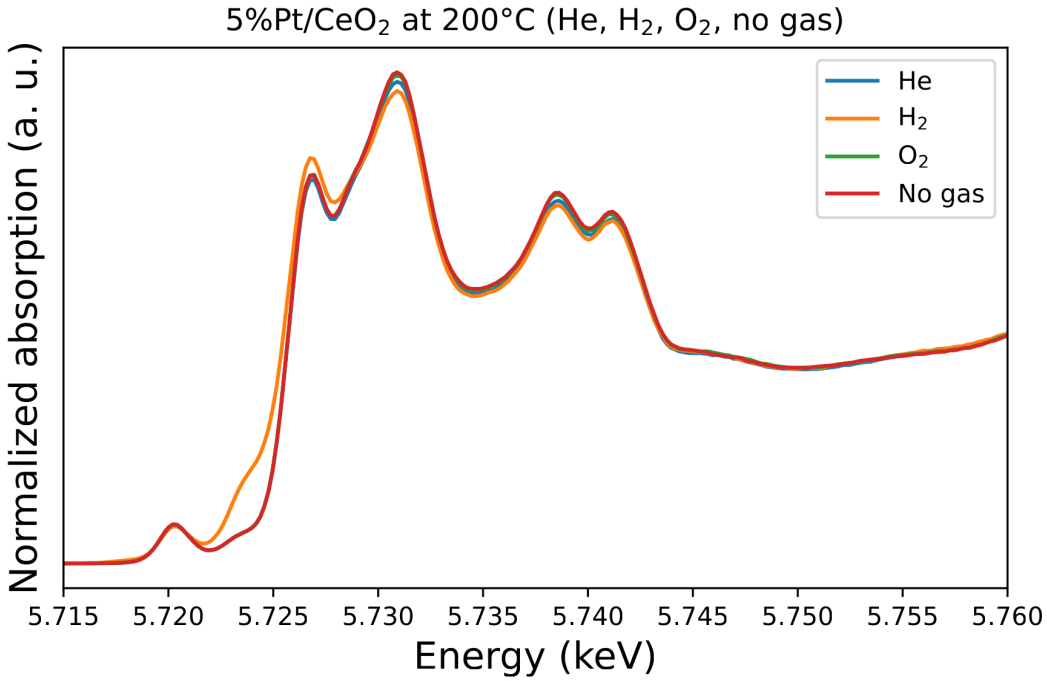

Figure 3.18: XANES spectra of the 5%Pt/CeO_2 sample, acquired at 200°C under helium, hydrogen, oxygen and no gas flow.

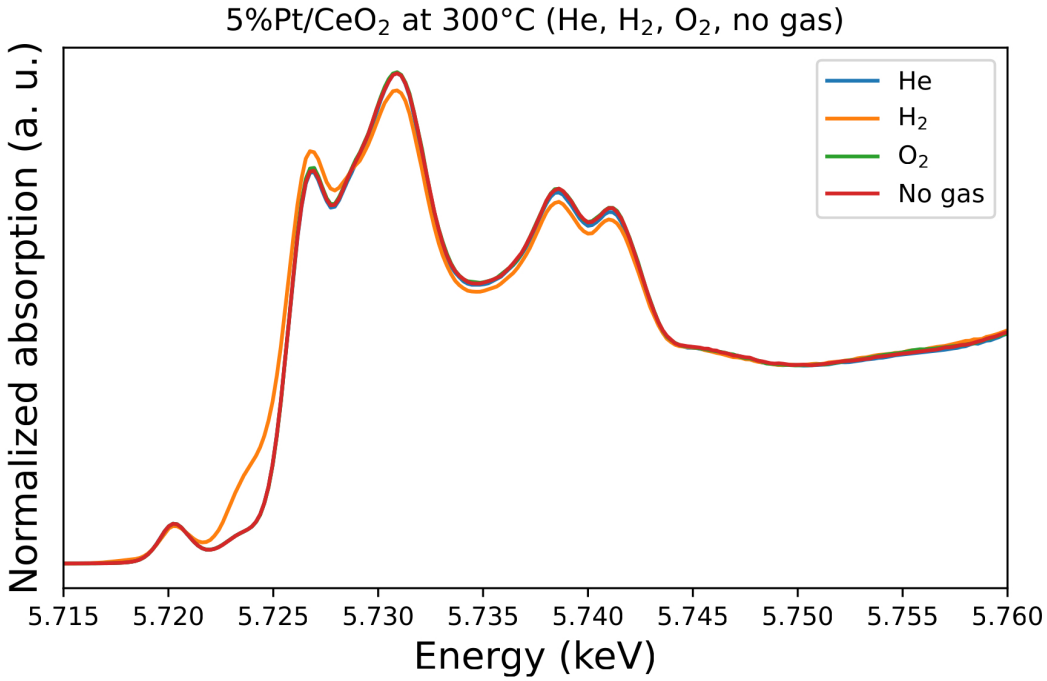

Figure 3.19: XANES spectra of the 5%Pt/CeO_2 sample, acquired at 300°C under helium, hydrogen, oxygen and no gas flow.

When increasing the temperature the shoulder around 5.724 keV grows as well, and in order to better appreciate the growing trend of such spectral feature with temperature, differential spectra – calculated subtracting the reduced spectrum (Ce under H_2) and the oxidized one (Ce under O_2) – are plotted together in Figure 3.20 for all the three temperatures.

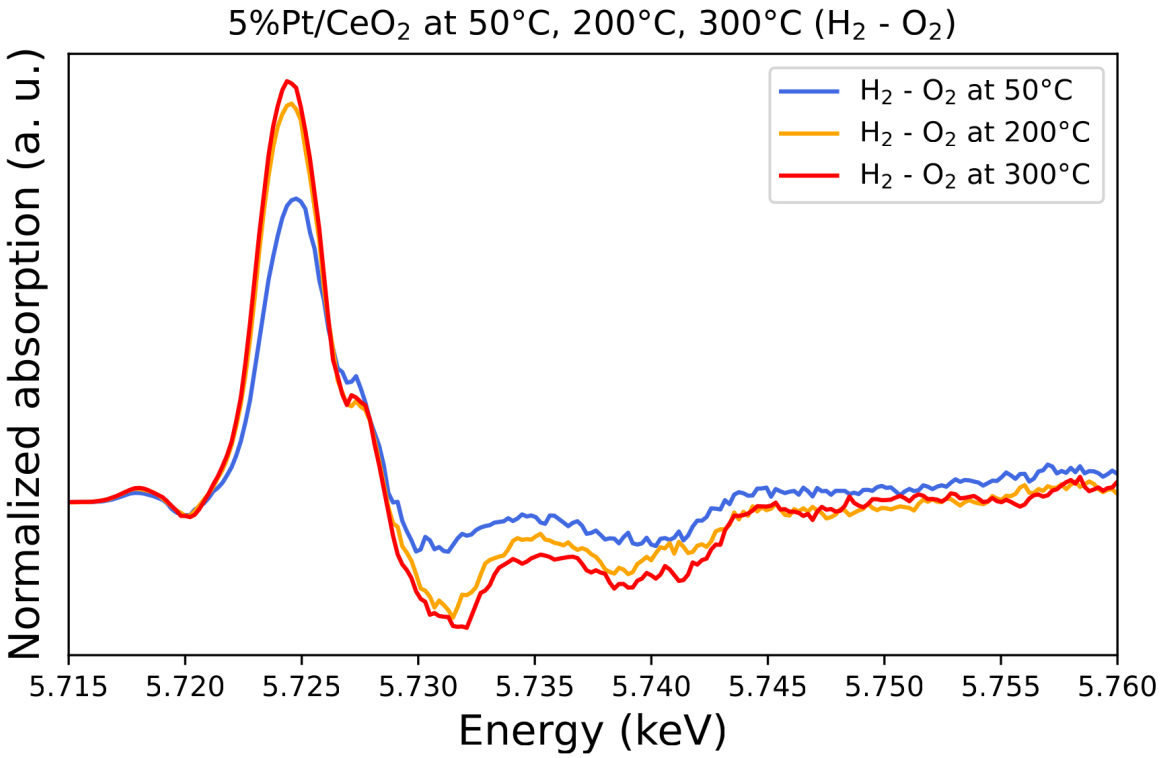

Figure 3.20: Difference XANES spectra (H_2-O_2) of the 5%Pt/CeO_2 sample at 50°C, 200°C, and 300°C.

From Figure 3.20 it is immediately visible that the major spectral changes are limited to the near-edge region, mainly involving the new shoulder appearing around 5.274 keV and the increased intensity of the white line around 5.726 keV at the expense of the adjacent peak on the right.

It can be noticed by the drastic change of the peaks in Figure 3.20 in the above mentioned regions, how such spectral modifications are related to the temperature, becoming more and more visible as the temperature is increased (red curve). Also, it is worth noting how the red curve (300°C) shows a slightly higher peak around 5.718 keV with respect to the blue curve (50°C), indicating that at high temperature some changes are occurring in the pre-edge region too.

The formation of oxygen vacancies in the ceria support is proposed as a possible explanation for the observed behavior when the temperature is increased. Further investigation is needed to fully understand the phenomenon and explain the experimental evidence.

The emergence of new spectral features may indicate a change in the electronic structure of ceria upon exposure to hydrogen flow, but can this modification be solely attributed to the creation of Ce^{3+} ions, or could other Ce species be present?

We have previously stated that oxygen vacancies created into the lattice are responsible for the shoulder observed in the spectra, but how are they really related to the electronic structure modifications of the system and how do they interact with Ce?

Finally, what is the role of platinum in the system and what are its effects on ceria chemical behavior with and without the presence of hydrogen flow?

In order to better address such spectral changes and find a possible answer to the open questions, *Chapter 4* is dedicated to discuss more in detail about the system, exploring the role of oxygen vacancies in relation to the reduction of ceria and the interaction that arises between Pt and the support when the noble metal is added on ceria.

4 | Discussions

It is now relevant to address such spectral changes observed under reducing environment by means of high resolution XAS.

The reason for this behavior is unknown, thus what follows in this fourth chapter is a discussion aimed at providing a possible interpretation of the data collected from the studied system, which is complex and requires a deep investigation.

In order to understand the origin of such spectral features it is useful to go through what is already known in literature about ceria and about its employment as a catalyst material.

For this reason, a first part of the present chapter offers a description of Ce electronic structure and of how oxygen vacancy formation can modify it, suggesting a possible role of such vacancies in the creation of new spectral features.

Subsequently, the remaining part is dedicated to discuss the strong metal-support interaction arising in the Pt/CeO_2 system.

In fact, it is necessary to explain why new spectral features were observed only in the presence of platinum, and in order to do so, we take advantage of the many publications concerning the application of ceria as a support material.

In particular, the strong synergy arising between platinum and ceria has already been investigated in previous literature and, both observing pre-existing studies and availing ourselves of the acquired experimental evidence, the following paragraphs are devoted to understand how Pt modifies the system behavior.

More specifically, *Section 4.2.1* gathers what is known about the phenomena arising when platinum is placed on ceria, while *Section 4.2.2* deals more into detail about the different behaviors of pure CeO_2 and Pt/CeO_2 systems under redox conditions.

4.1. The effects of oxygen vacancies on Ce electronic structure

As already mentioned above, we expected some spectral changes to appear in the ceria XANES spectra upon flowing hydrogen into the cell, and what we observed was that going up to 300°C only allows us to see such changes in the Pt/CeO_2 samples.

However, as it is discussed in the next sections, we strongly believe that such spectral modifications would appear in pure ceria as well when reaching higher temperatures, and that the presence of Pt is only able to lower the temperature at which these phenomena become visible.

We postpone the discussion about why Pt allows to witness such spectral modifications to *Section 4.2* and we now focus on a possible explanation hidden behind the said experimental evidence, reported once again in Figure 4.1 for the $1\%Pt/CeO_2$ sample at 300°C.

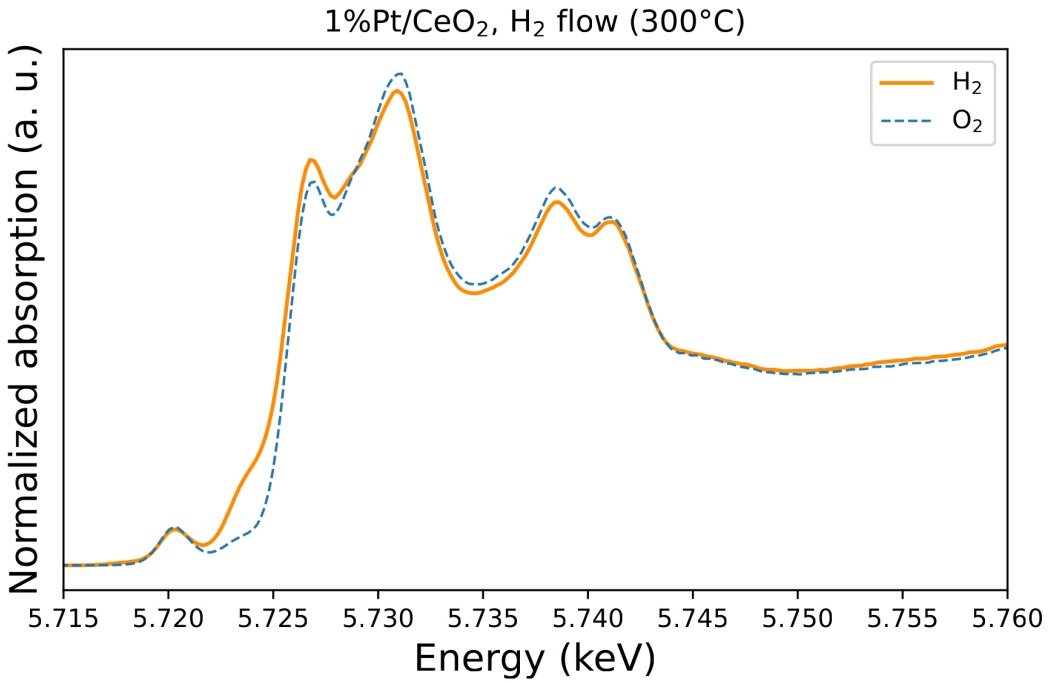

Figure 4.1: XANES spectrum of the $1\%Pt/CeO_2$ sample acquired under hydrogen gas flow (orange line), compared to the one acquired under oxygen flow (dashed blue line).

A large shoulder around 5.724 keV is appearing when hydrogen is flown onto the sample, creating a reducing environment, while it disappears when oxygen gas flow is provided.

Spectral changes were observed in various samples and were found to be highly reproducible when measurements were repeated. This suggests that a reversible process is the basis of the physical explanation for the shoulder appearance. The findings highlight the reliability of the experiment and indicate that the process is reversible.

Ceria is known for its highly mobile lattice oxygen, and we believe that such O atoms play a role into the appearance of the new spectral feature observed. We attribute the behavior shown in Figure 4.1 to the reduction of a fraction of Ce sites, and such reduction of Ce^{4+} to Ce^{3+} is intrinsically related to the formation of some vacancies due to oxygen atoms leaving the lattice, a widely-investigated phenomenon in ceria.

We believe that when enough thermal energy is provided to the system, the interaction between hydrogen and the oxygen atoms from the lattice is promoted, creating water in the cell and oxygen vacancies in the ceria structure (4.1).

$$H_2 + O_{lattice} \longrightarrow H_2O \tag{4.1}$$

On the other hand, when oxygen is flown onto the sample, the oxygen vacancies get filled again and a configuration identical to the one prior H_2-flowing is restored, as observed in the results in *Chapter 3*, where the O_2 curve is overlapping with the initial state curve (taken under He flow).

Such reversible transition has been widely investigated in previous works, *e.g.* Esch et al. [26] have acquired high-resolution scanning tunneling microscopy images, witnessing the formation of oxygen vacancies in $CeO_2(111)$.

Such high-resolution images allow to unravel the local structure at the (111) surface, spotting the surface and subsurface oxygen vacancies created in ceria after that annealing has been performed at high temperatures. Esch et al. [26] observed the formation of both single vacancies and clusters of more than two vacancies. On the slightly reduced surface an abundance of single vacancies prevails, divided in the two kinds, surface and subsurface. Surface vacancies appeared as depressions encircled by three paired lobes, while the subsurface ones appeared as triple protrusions centered around an oxygen site in the third layer of the lattice.

These kinds of STM images demonstrate how it is possible to directly observe and measure the distribution of the oxygen vacancies, but at the same time, when dealing with rare-earth oxides such as ceria, the chemistry of the system is not of immediate comprehension, and the characterization of the oxygen vacancies alone is not enough to understand the fundamental features of the reactivity.

Special attention must be given to the electronic structure of cerium, which is intrinsically affected by the formation of oxygen vacancies: in fact, as pictorially shown in Figure 4.2, the process of oxygen vacancy formation provides that when the oxygen atom leaves its lattice position, two electrons are left behind, localizing on two Ce atoms. More specifically, the localization of such electrons occurs on the lowest-energy level available, which is the f band of Ce.

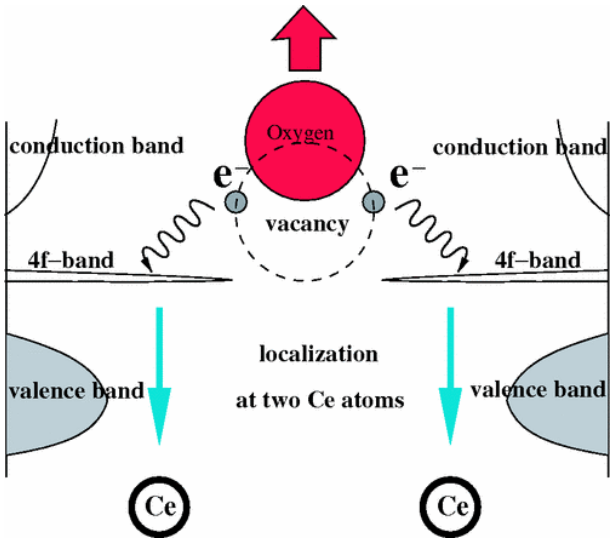

Figure 4.2: Scheme of the oxygen vacancy formation process in ceria: when the oxygen atom leaves the lattice, two electrons are localized on two Ce atoms [27].

Cerium is characterized by a partially occupied f orbital, that in the past decades has originated a few controversies. Such f orbital is usually treated as a core state in DFT calculations when ceria is in a γ phase, with the f states disconnected from the valence states [28].

Skorodumova et al. [27] carried out first principle quantum mechanical simulations for the two oxides CeO_2 and Ce_2O_3, and found that a good estimation of the electronic structure is given for different descriptions of the f states in the two cases: in CeO_2, where Ce is fully oxidized as Ce^{4+}, the $4f$ electron has to be treated as an ordinary valence electron, while in Ce_2O_3, where Ce is in its reduced form Ce^{3+}, the $4f$ electron is localized on the Ce atom.

According to this picture, ceria ground state has a f^0 configuration, where the f band is considered as equivalent to an empty atomic-like $4f$ level in the gap between valence and conduction bands, and all four valence electrons are transferred to the p bands of two oxygen atoms.

In order to better visualize Ce electronic structure, Figure 4.3 offers a schematic diagram of the energy levels in CeO_2, namely the *4f*, *5d*, *3d* and *2p* states, in addition to ligand (L) and valence (v) states.

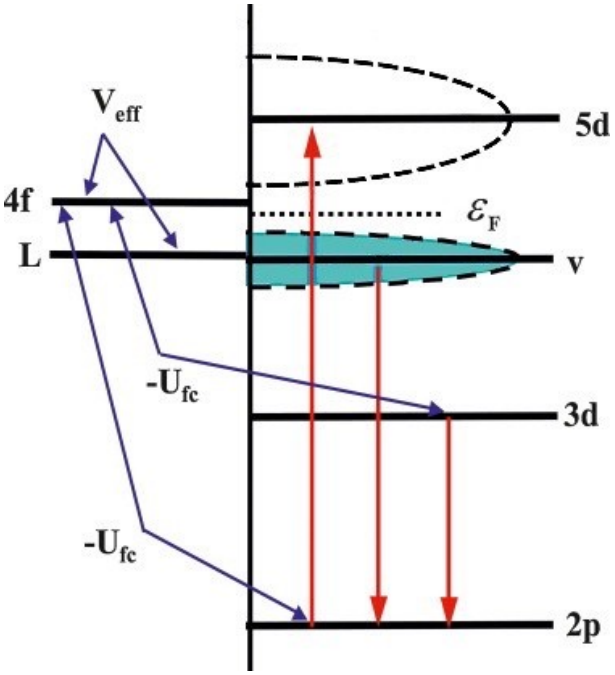

Figure 4.3: Schematic diagram of Ce electronic structure in CeO_2. The red arrows represent the probed *2p* to *5d* transitions and two possible de-excitation paths (not considered in this section) [29].

Ce *5d* and *2p* states, together with O *2p* state, are depicted in the figure as single levels for simplicity, but considering absorption spectra at the L_3 edge of Ce, we know that the probed transitions start from the initial state Ce $2p_{3/2}$.

The ligand state L corresponds to O *2p* states with f symmetry around the Ce atom and it hybridizes with Ce *4f* state, while the state v, corresponding to O *2p* levels as well, has d symmetry around the Ce atom, so that the transition from v to $2p_{3/2}$ states is dipole-allowed.

The hybridization between the *4f* and L states is represented in the picture by the V_{eff} term, and the $-U_{fc}$ potential accounts for the core hole effects onto the *4f* state, assuming it to be equal for the *3d* and *2p* core states.

In this frame, the ground state $|f^0>$ is the state with the occupied L, v, *3d* and *2p* levels, leaving empty the *4f* and the *5d* states.

However, the strong hybridization between the *4f* and L states originates a controversy

over the ground state of CeO_2, introducing a second picture: according to the latter, Ce ground state is correctly described by a strongly mixed state between the f^0 and the $f^1\underline{L}$ states, where $\underline{L}$ represents a hole in the ligand orbital L.

In this case, two energy levels arise (depicted in Figure 4.4), and the intermediate state, given by the excitation of an electron from the $2p_{3/2}$ to the $5d$ state, produces an energy difference between the $4f^1\underline{L}$ and the f^0 configurations equal to the core hole potential $-U_{fc}$, since the latter acts onto the f electron [30].

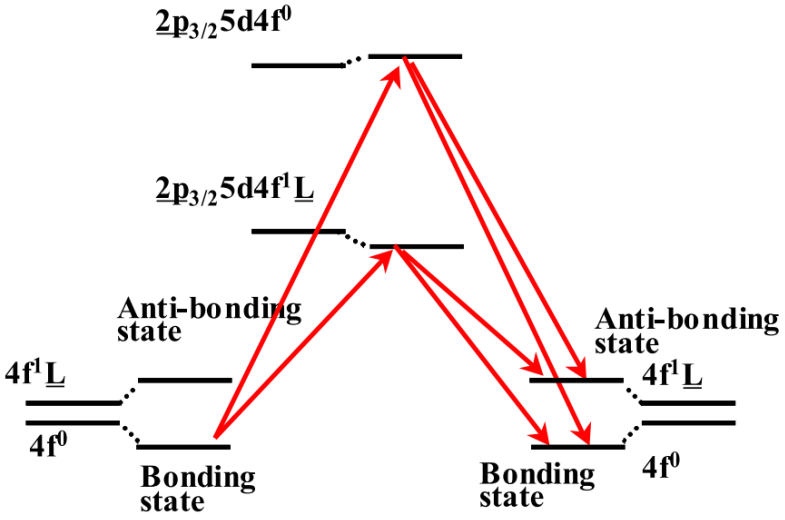

Figure 4.4: Schematic diagram of mixed valence state of Ce in CeO_2. The red arrows represent the probed $2p_{3/2}$ to $5d$ transitions and the four possible de-excitation paths [30].

Therefore, the core hole effect plays an important role in forming the Ce XAS structure at the L_3 edge, with the two peaks at 5.730 and 5.740 keV being given by the existence of the two excited states - called "screened" and "unscreened" - due to the mixed valence state.

The four possible de-excitation paths produce the four peaks at the L_3 edge in the spectrum (Figure 4.1), revealing the fine $5d$ structure.

However, atomic multiplet calculations performed in this frame are not able to predict the little shoulder around 5.724 keV [31], that grows noticeably under reducing environment.

In general, it is challenging to treat theoretically the $2p$ to $5d$ excitations, where core hole screening could be the cause of strong multi-electron excitations and some dipole transitions into the $5d$ density of unoccupied states may be left out of the calculations.

Moreover, the calculation could be enriched by an improved model, accounting for additional energy terms [30] (Figure 4.5):

- First of all, a more accurate *5d* level description, including the energy split between the $5d(t_{2g})$ and the $5d(e_g)$ bands.
- Secondly, contribution from the Ce $4f^2\underline{L}^2$ configuration introducing a U_{ff} term for the *f* electron interactions; the core hole potential acting on both *5d* states (U_{dc}), and the Coulomb interaction between Ce *4f* and *5d* states (U_{fd}).
- Lastly, the background contributions correspondent to transitions from *2p* into an unoccupied continuum state, represented by a step function in the DOS.

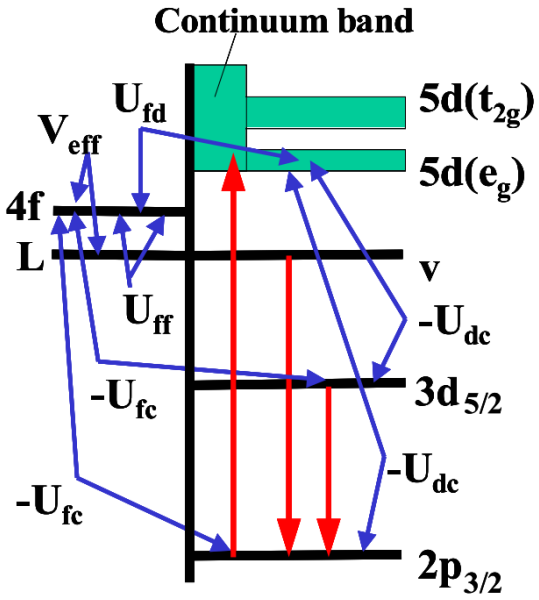

Figure 4.5: Schematic diagram of the improved model for Ce electronic structure in CeO_2. The red arrows represent the probed *2p* to *5d* transitions and two possible de-excitation paths (not considered in this section) [30].

The picture is therefore complicated and, to the limit of our knowledge, the shoulder around 5.724 keV has not been identified yet. Its strong dependence on H_2 presence, *i.e.* a reducing environment, suggests that it is intrinsically related to the reduction of ceria.

For this reason, regardless of the unresolved Ce *4f* controversy, we can associate the observed experimental evidence with the oxygen vacancy formation, accompanied by an increase in the Ce *4f* population.

In fact, when an oxygen atom leaves the lattice, two electrons are left behind and are localized on two Ce atoms, which are reduced from Ce^{4+} to Ce^{3+}.

Therefore, localization and delocalization of the Ce $4f$ electron, induced by the formation and annihilation of the oxygen vacancy, is the mechanism at the basis of the reversible reduction and re-oxidation process of cerium.

Calculations show the close connection between the process of oxygen vacancy formation and the presence of a Ce^{3+} site, such that the energy required to create an O-vacancy is found to be smaller in proximity of two Ce^{3+} ions and, at the same time, the most favorable position of Ce^{3+} atoms is next to an oxygen vacancy in the CeO_2 lattice [26, 27]. In particular, ceria has shown high propensity to coordinate only Ce^{3+} to vacancy clusters [26].

Overall, we can sum up by saying that we observed reversible spectral changes in the Ce L_3 XANES, appearing under hydrogen and disappearing again under oxygen gas flow. We provide a possible explanation by proposing that, under reduction conditions, oxygen atoms detach from the CeO_2 lattice surface and create vacant sites, leaving two electrons behind. Such vacancy formation is facilitated by the localization of the two electrons onto two neighboring Ce atoms, corresponding to the reduction of the latter Ce sites to Ce^{3+}. Whenever the O atom is restoring its position annihilating the vacancy, the electronic charge delocalize again and transfer to oxygen, oxidizing Ce^{3+} to Ce^{4+}. For this reason, according to if the environment is oxygen poor or oxygen rich, the process can work in both directions, leading to reversible transformations.

4.2. Ceria as a support material

It is now important to discuss why at 300°C we only witness the appearance of new spectral features when platinum is added to the system.

In Figures 4.6 and 4.7 a comparison of the reduced Ce spectra in pure CeO_2 and in the two Pt/CeO_2 samples is reported. Please note that from now on only commercial CeO_2 spectra will be used for the comparison of pure ceria with Pt/CeO_2 systems.

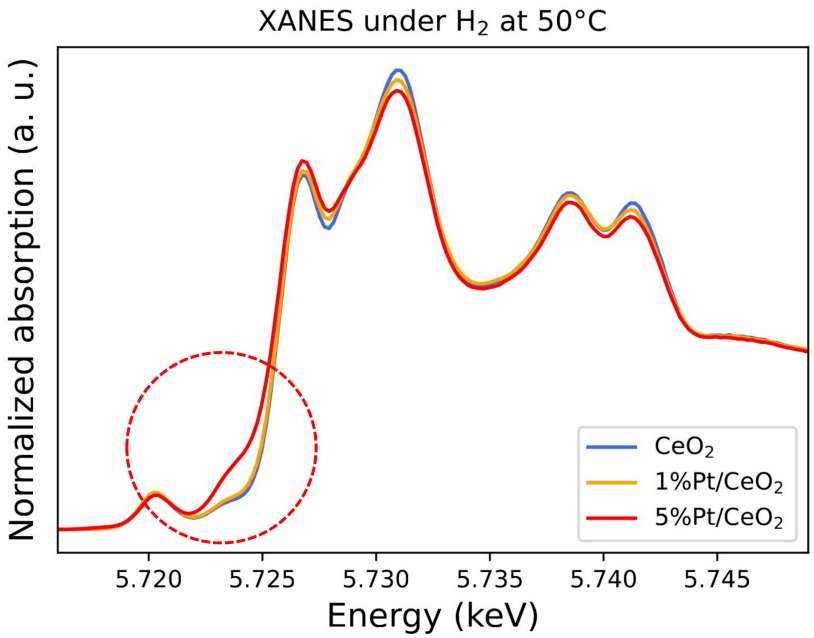

Figure 4.6: Comparison of the XANES spectra in pure CeO_2 and in 1%Pt/CeO_2 and 5%Pt/CeO_2, acquired under hydrogen gas flow at 50°C.

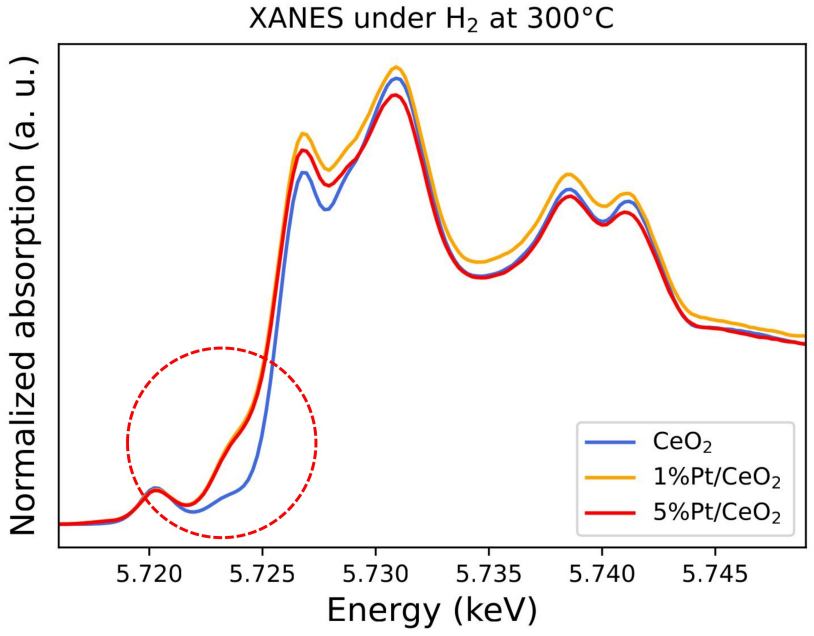

Figure 4.7: Comparison of the XANES spectra in pure CeO_2 and in 1%Pt/CeO_2 and 5%Pt/CeO_2, acquired under hydrogen gas flow at 300°C.

Repeated measurements of pure ceria and two different Pt/CeO_2 systems were conducted

at various temperatures, and consistent spectral changes were observed each time, demonstrating the high reproducibility of the results.

The appearance of such modifications exclusively for Pt/CeO_2 systems in our experiments makes it necessary to discuss the role of ceria as a support material.

Given the complexity of CeO_2-based materials, many studies involving different model catalyst have been carried out and developed in order to gain a deeper understanding of general or more specific catalytic behaviors.

Accordingly, the interaction between a CeO_2 support and metals has been subject of many recent investigations [32–34], being of high importance for the assembly of catalytic metal systems. Many different systems have been considered and developed, such as ceria-based thin films prepared in combination with other oxides, or the so-called 'inverse' catalysts [35], where ceria nanoparticles are deposited onto the catalytically active metal phase, rather than the other way around, but the general matter of interest is the interaction arising between the metal and the support, that alters the electronic states of the oxide support giving rise to different chemical properties and consequently to new and enhanced catalytic properties.

Generally speaking, the presence of the metal boosts the activity of CeO_2 catalysts for most processes, therefore many publications aim at developing model catalysts to offer new and better insights into the physical processes occurring at the surface, being these kinetics, mechanisms, or energetics [33, 34].

In particular, noble metal nanoparticles are the most promising and investigated class of catalysts, and among these Pt-ceria catalysts stand as protagonists of a wide field of studies. In fact, as it is identified by the data presented in *Chapter 3*, it is suggested that platinum somehow enhances the chemical activity of CeO_2, facilitating its reduction. This behavior is indeed well known in literature, being CeO_2 often implemented in many applications as a catalyst support material in combination with platinum group metals (PGMs).

PGMs are characterized by their unique electronic *d*-band structure that makes them widely used as catalytically active phase in catalyst, while CeO_2 is often chosen as a support due to its ability to both stabilize metal dispersion and to sustain a high mobility of lattice oxygen atoms. Many applications are found in different kinds of reactions, such as CO oxidation, hydrogenation and others.

In particular, PGMs are dispersed on the support and they strongly interact with it, giving rise to the so-called strong metal-support interaction, that plays a crucial role at

the metal-ceria interface [36, 37] and leads to many interesting phenomena that are better explained in the next few paragraphs below.

Because of such strong interaction, ceria-based catalysts are often studied with the purpose to find a good support material to better exploit the catalytic action of the noble metal, where the latter is considered the main object of research in the vast majority of catalysis-concerning publications.

On the contrary, our focus is turn to the support material, being the main interest of this thesis firmly on the chemical and electronic behavior of ceria.

Our goal is to understand how Pt modifies ceria electronic structure: we want to ascertain that the experimental evidence that our measurements revealed finds its microscopical origin in ceria peculiar structure, and *not* in new alleged characteristics introduced by the presence of platinum.

4.2.1. Platinum on ceria

Focusing on the system of interest of this thesis, we now discuss platinum dispersed on nanoceria support: we have mentioned above how the close proximity of Pt and ceria often results in a considerable increase of activity.

New properties arise from the formation of the complex nanostructure, strongly differing from the properties of the single components, and this is due to phenomena occurring at the interface between the active metal and the support.

In 1978 Tauster et al. [36] coined the term "Strong Metal-Support Interaction" (SMSI) to describe such phenomena at the interface between a metal species and the oxide support on which it is placed.

The presence of a metal can alter the catalytic performance of the support more or less severely according to many parameters, *e.g.* the nature of the reactants and the size of the system, as it is further explored below in this section.

In particular, SMSI is observed in systems where the support is reducible, like ceria, and its main effects can be categorized into three principal metal-support intefacial types of phenomena: electronic, geometric and bifunctional [34].

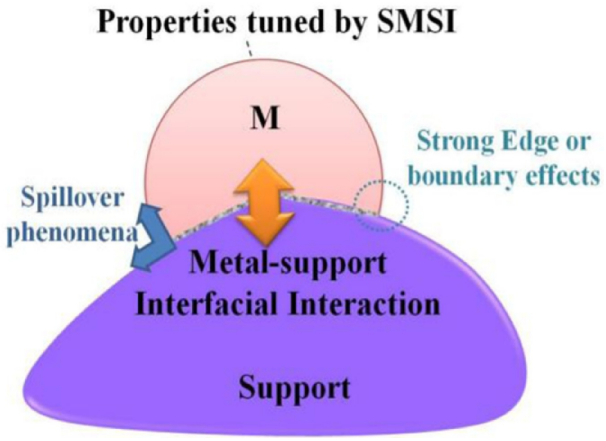

Figure 4.8: Schematic depiction of a metal particle onto an a support and the interfacial effects arising due to SMSI [34].

The three types of metal-oxide interfacial phenomena constituting the SMSI effects are discussed in the next subsections, going into more detail about the case system.

Electronic effect

Transport phenomena are originated at the interface between Pt and the CeO_2 support, together with charge redistribution when the metal is deposited.

Depending on the degree of the metal-oxide interaction (whether it is weak or strong) and on the energy minimization principle, electron transfer can occur at the reactive interface, where some atomic bonds are weakened and new ones are formed.

More specifically, in the case of Pt/CeO_2 electron transfer from the Pt nanoparticle to the support is identified [38].

Considering the density of states of a bulk-like CeO_2 support, it is found to significantly change when going to the nanoscale, in particular the gap between the highest occupied molecular orbital (HOMO) and the lowest unoccupied molecular orbital (LUMO) is markedly reduced for ceria nanoparticles.

In the case of nanometre-sized CeO_2, the HOMO is principally constituted by O *2p* orbitals, while the LUMO by Ce *4f* [39].

When adding Pt nanoparticles onto the structure, the DOS of the CeO_2 support is not significantly modified, however, new available electronic states are introduced inside the bandgap, changing the HOMO and the LUMO of the system (see Figure 4.9).

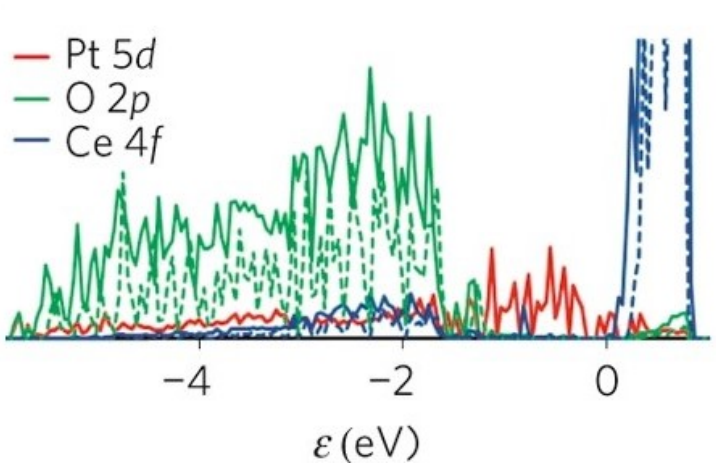

Figure 4.9: Density of states plot calculated for a pure $Ce_{40}O_{80}$ nanoparticle (dashed lines) and for the $Pt_8/Ce_{40}O_{80}$ system (solid line). The energies are plotted with respect to the Fermi level of $Pt_8/Ce_{40}O_{80}$ [38].

Consequently, the very small energy difference between the highest occupied Pt states and the empty Ce *4f* allows electron transfer from the metal cluster to the support, leading to the oxidation of some Pt sites at the interface, in conjunction with the reduction of some Ce sites in its proximity.

Calculations performed for $Pt/CeO_2(111)$ and for a $Pt_8/Ce_{40}O_{80}$ system show that such electron transfer occurs spontaneously, both in the case of bulk-like and nanometre-sized support [38, 40].

Therefore, Ce^{3+} formation is expected when Pt nanoparticles are deposited onto a CeO_2 support, as depicted in Figure 4.10.

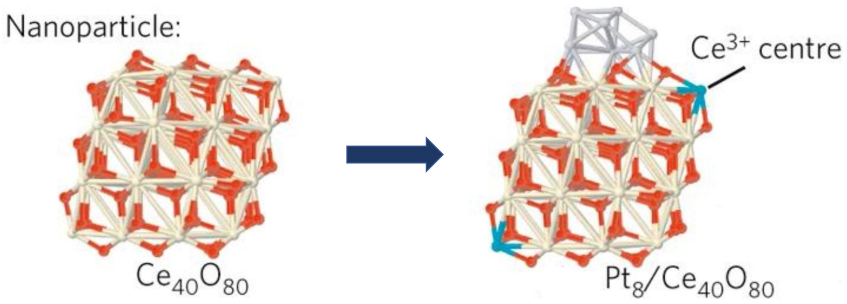

Figure 4.10: Electron transfer from Pt nanocluster to ceria support depicted for a $Pt_8/Ce_{40}O_{80}$ system [38].

It is found, however, that nanoscale effects dramatically modify certain properties of the system: in the case of electron transfer they seem to be hardly relevant, but there are

other effects that are strongly altered, and sometimes completely induced, by the system size, such as the ones discussed below.

Geometric effect

Geometric effects originate from support sites or thin layer physically covering the metal nanoparticle deposited on its surface. Such encapsulation phenomenon (or decoration) can happen partially or completely according to the strength of the metal-oxide interaction, while it is absent when the interaction is weak (Figure 4.11). It is in general driven by thermodynamical balances between metal-metal and metal-oxide bonds.

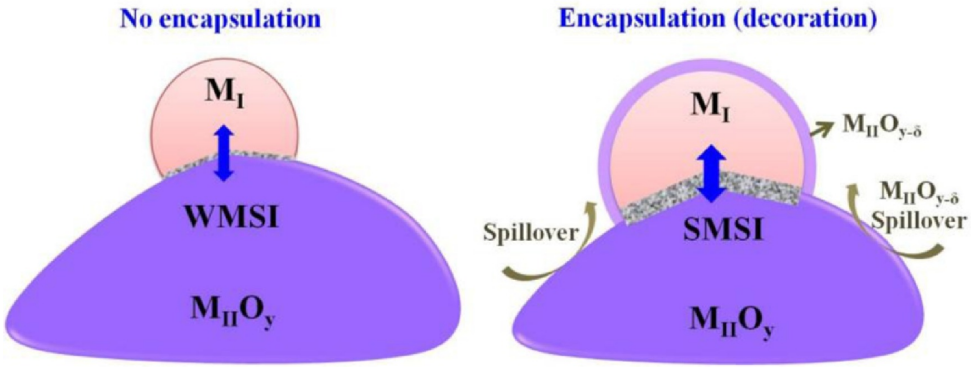

Figure 4.11: Geometric effect of encapsulation induced by strong metal-support interaction [34].

Similarly, the shape of the metal cluster is influenced by such interfacial effects: in the case of weak metal-support interaction the shape of the metal nanoparticle is preserved, while upon applying a strong interaction with the support, the metal cluster can assume a flattened configuration (Figure 4.12).

Moreover, geometric effects are notably influenced by the dimensions of the system, arising only when the size of the metal cluster allows it. In fact, as it is depicted in Figure 4.12, for large clusters the morphology remains unchanged due to the fact that in this case most of the catalytically active surface is far from the metal-oxide interface.

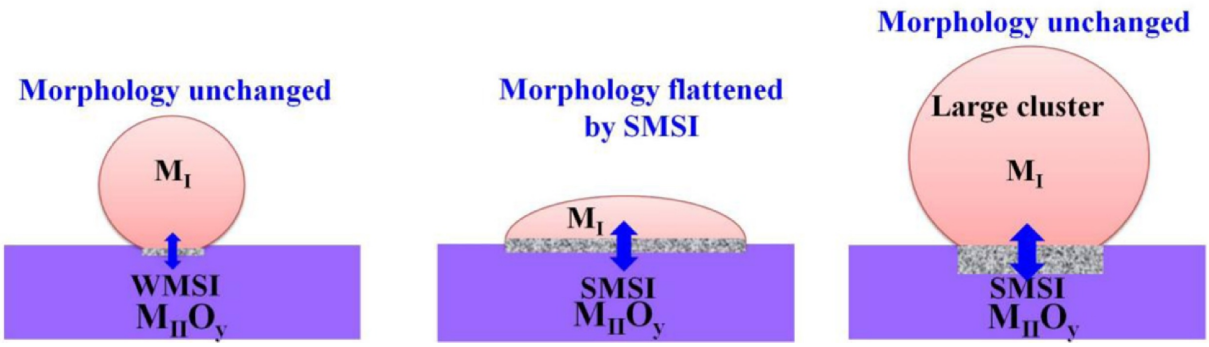

Figure 4.12: Geometric effect induced by weak or strong metal-support interaction [34].

In the case of our samples Pt nanoclusters do not appear completely encanpsulated by the system [15], although some oxygen atoms may have migrated from the support onto the metal nanoparticle to form some PtO_x species, together with CeO_{2-x} species in the support.

In fact, such phenomenon is known as "reverse spillover", *i.e.* oxygen migration through the particle boundary [40, 41], and it is observed in Pt-ceria catalysts only at the nanoscale.

It is calculated that formation of oxygen vacancies in nanoceria can be strongly favoured with respect to bulk-like ceria support [38], leading to energetically favourable reverse spillover of oxygen to the Pt nanocluster (Figure 4.13).

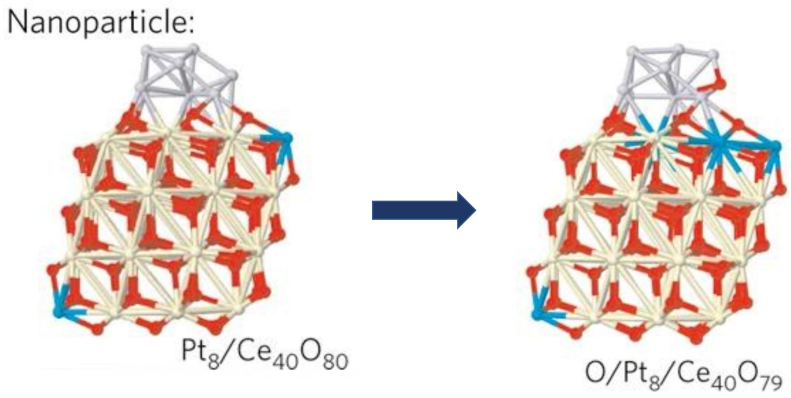

Figure 4.13: Reverse spillover of oxygen from the nanoceria support to the Pt cluster [38].

The migration of each oxygen atom from the CeO_2 lattice onto the metal nanocluster is accompanied by the formation of two Ce^{3+} sites, therefore, together with electron transfer effects, reverse oxygen spillover is responsible for further reduction of ceria.

Experimental demonstration of the occurrence of such interfacial phenomena can be very

demanding, however it is possible to find it indirectly by monitoring the reduction of the ceria support, *i.e.* the Ce^{3+} concentration.

In order to do so, Vayssilov et al. [38] investigated the concentration of Ce^{3+} in pure ceria and in Pt/CeO_2 by performing surface-sensitive RPES measurements, and found that no significant changing occurs in the concentration of Ce^{3+} in pure $CeO_2(111)$ thin film, confirming that Ce does not change its oxidation state and that the vast majority of O atoms remain bounded to the lattice.

On the other hand, the situation was much different for the Pt/CeO_2 system. In fact, as soon as Pt is added onto the ceria support, already at room temperature, a notable increase in the concentration of Ce^{3+} was observed, and this is attributed to the electron transfer phenomenon previously discussed: electrons migrate from the Pt nanocluster to the support, leading to the reduction of some Ce sites.

When increasing the temperature, Ce^{3+} presence was further increased, and this is attributed to oxygen reverse spillover that becomes favorable at higher temperatures, only in the nanometre-sized CeO_2 support [38].

Bifunctional effect

The expression "bifunctional mechanism" stems from the peculiar behavior of metal-oxide systems, where both parts provide separate, although synergistic, reaction sites, with the final result of improved catalytic activity.

Because of SMSI new reaction sites are created at the interface, producing effects like spillover phenomena: in such cases, reactive species interacting with the metal migrate from the latter onto the oxide support, reacting at the surface with second reaction sites provided by the support.

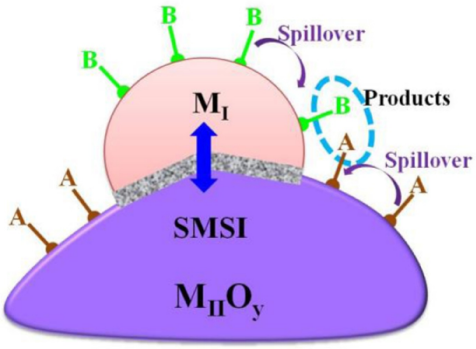

Figure 4.14: Bifunctional effect of reactive species B migrating from the metal to the support, where it interacts with second reactive species A provided by the oxide [34].

As it is depicted in Figure 4.14, the metal interacting with reactive species B can favour the migration of the latter onto the support, where different reactive species A are provided by the oxide and able to react with B species.

A species are often the labile oxygen atoms in the support lattice, which are under-coordinated at the surface, and this applies to our case study as well.

In fact, it is calculated that the energy required to remove a surface oxygen atom close to a Pt nanoparticle is much less with respect to those necessary to remove it from a clean ceria surface [40]. This is due to the SMSI effects introduced in this section, and has major repercussions on the behavior of ceria under reducing environment, *i.e.* under H_2 gas flow.

For this reason, the next section is dedicated to explore deeper the behavior of Pt/CeO_2 systems under H_2 gas flow. Furthermore, we provide additional information on the spillover effect (see the next section) as it is deemed critical for comprehending our experimental results.

4.2.2. Platinum on ceria in redox conditions

We can understand the effect of adding platinum onto the system under a reducing environment by comparing hydrogen temperature-programmed reduction (TPR) measurements performed on pure ceria and on Pt/CeO_2 samples.

In a TPR experiment a reducing gas is flown across the catalyst as the temperature is linearly increased so that the reduction can be plotted against time. At the outlet the chemical difference in atmospheric concentration is analyzed by a detector, producing an accurate picture of the reduction peaks of the catalyst.

As an example, in Figure 4.15 TPR data collected by Lee et al. [42] are reported. In particular, they studied the reducibility of a $2\%Pt/CeO_2$ sample and compared it to pure ceria measurements data.

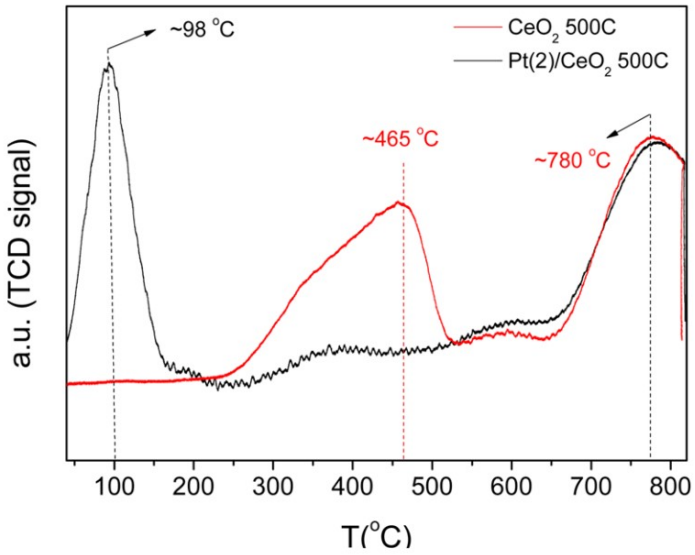

Figure 4.15: H_2 temperature-programmed reduction curves of CeO_2 and 2%Pt/CeO_2 [42]

For both the samples two reduction peaks are present, due to the compact Ce cation sublattice that creates a cage effect restricting all oxygens except those on the surface. In fact, the first peak appearing at lower temperature is attributed to the reduction of surface ceria, being surface oxygen of CeO_2 under-coordinated (2 to 3 instead of 4) and, therefore, more likely to interact with hydrogen at lower temperature.

The second peak, instead, is associated to the reduction of bulk ceria: given the fluorite structure of ceria, bulk oxygen is caged within four cations and therefore needs high temperatures to react with hydrogen.

Comparing the red and the black curves associated to the two samples, we notice that the bulk ceria peak remains fixed around 780°C, meaning that platinum-cerium interaction is confined to the surface, leaving bulk oxygen unaffected by the presence of platinum.

On the other hand, considering the reduction peak of surface ceria, a large shift is present: to reduce clean surface ceria the temperature required is around 465°C, while with the impregnation of 2 wt % of Pt the reduction becomes visible around 98°C.

This is coherent with what we observed for 1%Pt/CeO_2: no spectral changes appear in the spectrum under reducing environment at 50°C, but when increasing the temperature to 200°C the peculiar shoulder evidenced in Figure 4.7 shows up.

In order to explain such effect on the reduction peak appearing in the presence of Pt on the surface, it is relevant to investigate the new bonds created at the interface between Pt and ceria.

It is known, in fact, that the Ce-O bond is weakened by the presence of the metal, leading to a more reducible surface.

In particular, it is found in literature through *in situ* and *ex situ* Raman spectroscopy that Pt is anchored with the surface oxygen of CeO_2 by forming Pt–O–Ce bond [42, 43], as depicted in the schematic diagram in Figure 4.16.

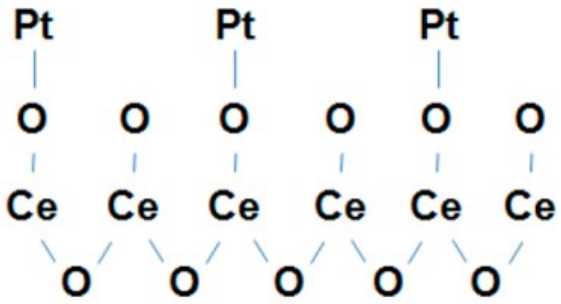

Figure 4.16: Pt–O–Ce bond formed between Pt and CeO_2 after an oxidative treatment [42]

It is known that Pt–O–Ce species, resulting from the strong interaction between platinum and CeO_2, are reduced at temperatures between 40-250°C, and such information is coherent with the TPR measurements where, in the case of Pt/CeO_2 samples (black curve in Figure 4.15), the first reduction peak at lower temperature is associated with the reduction of PtO_x species formed onto the surface of the support, accompanied by neighboring Ce^{4+} reduction.

When Pt loading increases, we expect such reduction peak to shift further to even lower temperatures, because of the size increase of the Pt particles, coherently with what we observed: in fact, in the XANES spectra acquired under H_2 flow at 50°C we did not observe any prominent changes in the $1\%Pt/CeO_2$ sample, but when we switched to $5\%Pt/CeO_2$ noticeable differences were seen in the spectral features, changes that we relate to the reduction of the sample.

Similarly, DFT calculations in literature provide more insight into Pt/CeO_2 chemical bonds at the interface: such studies underline the unusual configuration of oxygen atoms at the Pt/CeO_2 interface, situated between a Ce and a Pt atom: these O atoms are characterized by a considerably lower energy required to remove them from the lattice, resulting in the possibility to participate in the reaction and consequently to low temperature catalytic activity [44].

In situ EXAFS analysis performed by Gatla et al. [45] on Pt/CeO_2 reveals that the local environment of Pt is similar to that of platinum oxide, but with a lower coordination

number, indicating high dispersion of the Pt particles on the ceria support.

Moreover, after *in situ* reduction of the system, the local environment of platinum changes, resulting from a Pt-O bond distance notably longer with respect to the PtO_2 case. At the same time, the Pt-Pt bond results shorter with respect to the metallic Pt case, probably due to an increase in the electronic density between two adjacent sites associated with the rehybridization of the *spd* orbitals in Pt atoms [45].

Such elongated Pt-O bond under reducing conditions is held responsible for the low-temperature catalytic activity of the Pt/CeO_2 system, causing the weakening of the bonding between O atoms and the ceria support.

In addition to this, Gatla et al. [45] propose that the catalytic performance is determined by the Ce^{3+} formed in proximity to the Pt nanoparticle: in fact the appearance of Pt-O-Ce bonds seems to be accompanied by the creation of oxygen vacancies contributing to the formation of Ce^{3+} ions.

Indeed, it has been calculated many times in literature, by means of different spectroscopic measurements at the L_3 edge of Ce, that an increase in the concentration of Ce^{3+} ions is found during hydrogen treatments [45, 46].

The difference between the behavior of pure ceria and those of ceria with the addition of Pt relies in the temperature at which such Ce^{3+} concentration increase is detected.

In order to better appreciate such difference, comparison plots made by Alayoglu et al. [46] of the $\%Ce^{3+}$ in pure ceria and in Pt/CeO_2 are offered in Figure 4.17a under oxygen and hydrogen, as a function of temperature.

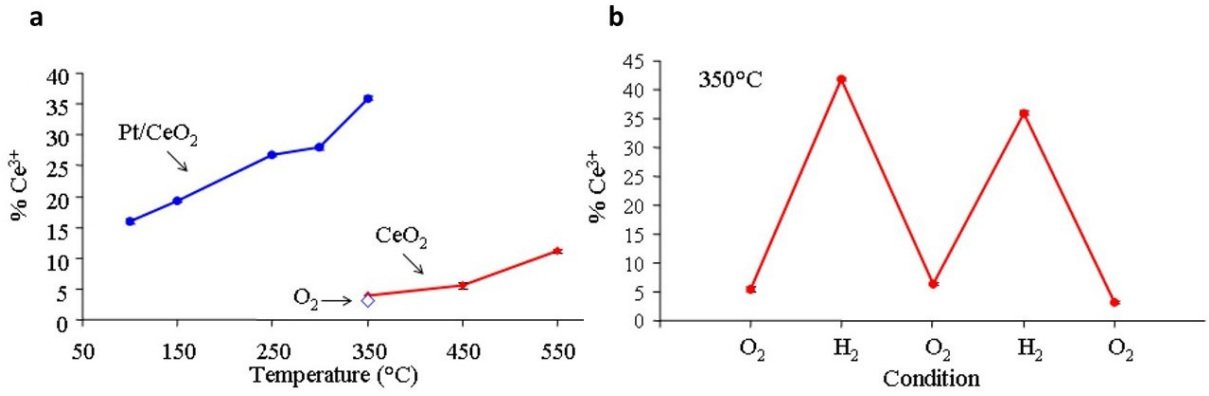

Figure 4.17: (a) Plots of % atom Ce^{3+} as a function of temperature in Pt/CeO_2 (blue line) and pure CeO_2 (red line), calculated from quantification analysis of APXPS spectra acquired under H_2. (b) Plot of % atom Ce^{3+} in Pt/CeO_2 in redox conditions at 350°C [46]

As it is visible from Figure 4.17a, for pure CeO_2 at 350°C changing the gaseous environment from O_2 to H_2 does not significantly affect the percentage of Ce^{3+}, that remains low with respect to Ce^{4+}, but increasing the temperature above 450°C causes an increase of the Ce^{3+} presence in the system. This is coherent with what is expected on the basis of the TPR measurements previously mentioned and presented in Figure 4.15.

When considering Pt/CeO_2 instead, an appreciable increase in the Ce^{3+} percentage is obtained already below 150°C, with a steep increase of % Ce^{3+} with temperature.

In Figure 4.17b it is illustrated how the percentage of Ce^{3+} in Pt/CeO_2 changes upon changing the gaseous environment at a fixed temperature of 350°C: when switching back to oxygen from a hydrogen environment, Ce^{3+} drops to the starting value, demonstrating the reversibility under the given conditions.

Overall, the key result is that the fraction of Ce^{3+} increases significantly when the sample is exposed to a hydrogen flow at a temperature below 350°C only when platinum is present, and this is coherent with the results of our experiment, reported in *Chapter 3*.

In our case it is difficult to quantify the presence of Ce^{3+} from the spectra acquired at ID26, since this is assumed from the oxygen vacancy formation process inducing the spectral changes, and not from direct evidence from the XAS spectra.

However, by looking in more detail at the pre-edge region, it is possible to deduct the formation of some Ce^{3+} ions by comparing the Pt/CeO_2 sample spectra with a liquid $CeCl_3$ standard, providing a reference for a pure Ce^{3+} spectrum at the L_3 pre-edge (Figure 4.18).

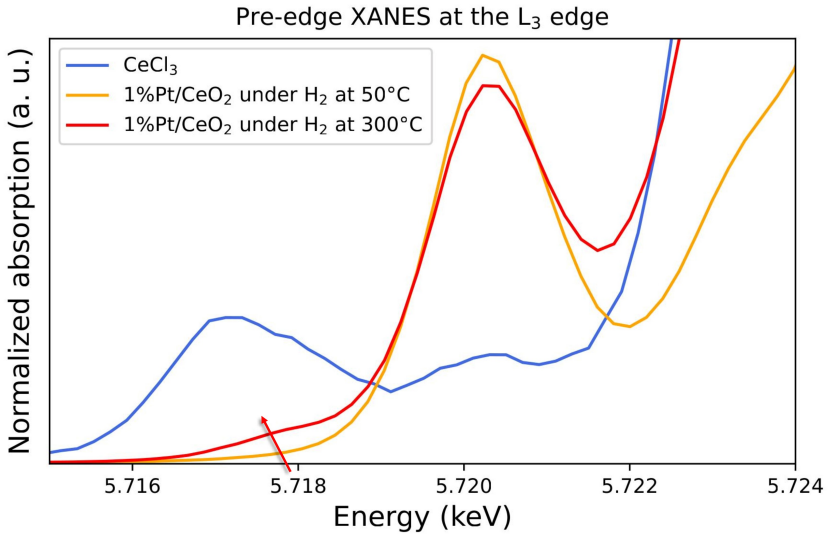

Figure 4.18: XANES spectra at the L_3 edge for liquid $CeCl_3$ in H_2O and at RT, and for 1%Pt/CeO_2 under H_2 flow at 50°C and 300°C.

The $CeCl_3$ sample shows the double-peak pre-edge typical of Ce^{3+}, as explained in *Section 1.2*, while 1%Pt/CeO_2 at 50°C shows the single-peak pre-edge characteristic of Ce^{4+}, since the shoulder at 5.724 keV is not formed and the sample is not reduced yet.

On the other hand, the red line in Figure 4.18, corresponding to 1%Pt/CeO_2 at 300°C, shows a little bump just before 5.718 keV, suggesting that at 300°C some Ce sites are reduced to Ce^{3+}, and the sample shows the appearance of the new spectral features discussed in *Section 4.1*.

Such spectral modifications in the pre-edge region are very small and indicate that the number of Ce^{3+} sites in the sample is very limited. These reduced sites correspond to the Ce atoms at the interface interacting with Pt (that facilitates their reduction), and an estimation of the number of such interacting sites can be retrieved and is therefore addressed in *Section 4.2.3*.

However, by making the same comparison between the $CeCl_3$ XAS spectrum, and the 1%Pt/CeO_2 and pure CeO_2 spectra at 300°C (shown in Figure 4.19), once again we can conclude that without Pt the reduction from Ce^{4+} to Ce^{3+} is not triggered.

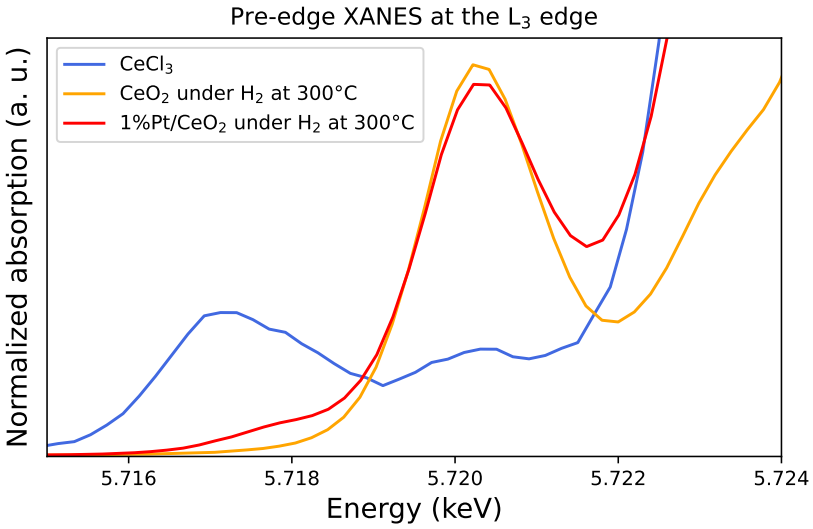

Figure 4.19: XANES spectra at the L_3 edge for liquid $CeCl_3$ in H_2O and at RT, for pure CeO_2 under H_2 flow at 300°C, and for 1%Pt/CeO_2 under H_2 flow at 300°C.

For this reason, it is now discussed the physical mechanism at the basis of Pt ability to facilitate the ceria support reduction.

As it was anticipated by *Section 4.2.1* discussing about bifunctional SMSI phenomena, we believe that the origin of this behavior is attributed to the spillover phenomenon of

atomic hydrogen H from Pt to the CeO_2 surface.

Hydrogen spillover

Hydrogen spillover [47] is the phenomenon of activated hydrogen atoms generated from a metal catalyst particle and migrating onto the surface of the catalyst oxide support [48].

It is widely accepted that Pt catalyst nanoparticles are able to dissociate H_2 molecules into atomic H [49, 50], which then spills and diffuses onto the reducible oxide support. In fact, first-principles atomistic simulations show spontaneous dissociation of hydrogen on the Pt cluster independently on the support [48], together with a small activation energy for surface diffusion, due to the fact that spillover occurring at the interface requires the breaking of bonds between H and the adsorbing surface, and the creation of new bonds with the accepting surface [49].

As a final effect of the spillover of H atoms from Pt onto the support, the reduction of ceria at the interface is facilitated at lower temperature (as confirmed by the TPR measurements, Figure 4.15).

In fact, because H atom is reactive and mobile on the surface, it is able to interact with the more weakly-bounded O atoms at the lattice surface and, consequently, to reduce CeO_2 creating OH species or O vacancies (below denoted as V_o).

As a final result of the process, in the presence of Pt, ceria surface is reduced because of the simultaneous creation of O vacancies and Ce^{3+} sites, together with the formation of water in the cell, given by the H atoms spilled by the metal nanoclusters and interacting with surface oxygen.

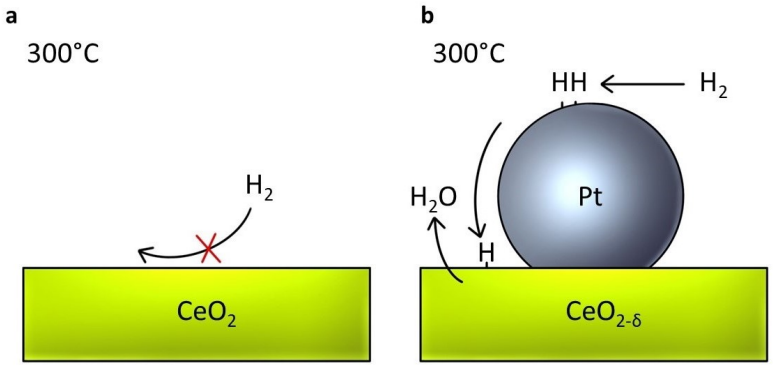

Figure 4.20: Pictorial visualization of the interaction at 300°C of (a) pure CeO_2 with H_2, where no chemical reaction originates and (b) Pt/CeO_2 with H_2, where water formation is speculated.

$$2Pt + H_2 \longrightarrow 2Pt - H \tag{4.2}$$

$$Pt - H + CeO_2 \longrightarrow CeO_2 - H + Pt \tag{4.3}$$

$$2CeO_2 - H \longrightarrow Ce_2^{3+}O_3V_o + H_2O_{(g)} \tag{4.4}$$

Therefore, at 300°C thermal energy alone is too low to trigger any significant reaction between lattice oxygen and hydrogen in pure ceria, leaving the sample not affected by the hydrogen flow, but on the contrary, when Pt is present, the kinetic barrier for the reduction of CeO_2 is reduced and oxygen from the CeO_2 lattice interacts with the H spilled onto the ceria surface, eventually forming water and leaving a vacant site in the lattice.

Following, a summary of what we believe is happening to the system is reported:

- When we flow H_2 onto the sample, if enough thermal energy is provided to overcome the activation barrier for spillover to occur, H atoms are spilled onto the support and interact with O atoms at the surface, forming water into the cell and oxygen vacancies in the ceria lattice. Ce^{3+} ions are formed and the lattice is reduced, showing new spectral features at the L_3 edge.

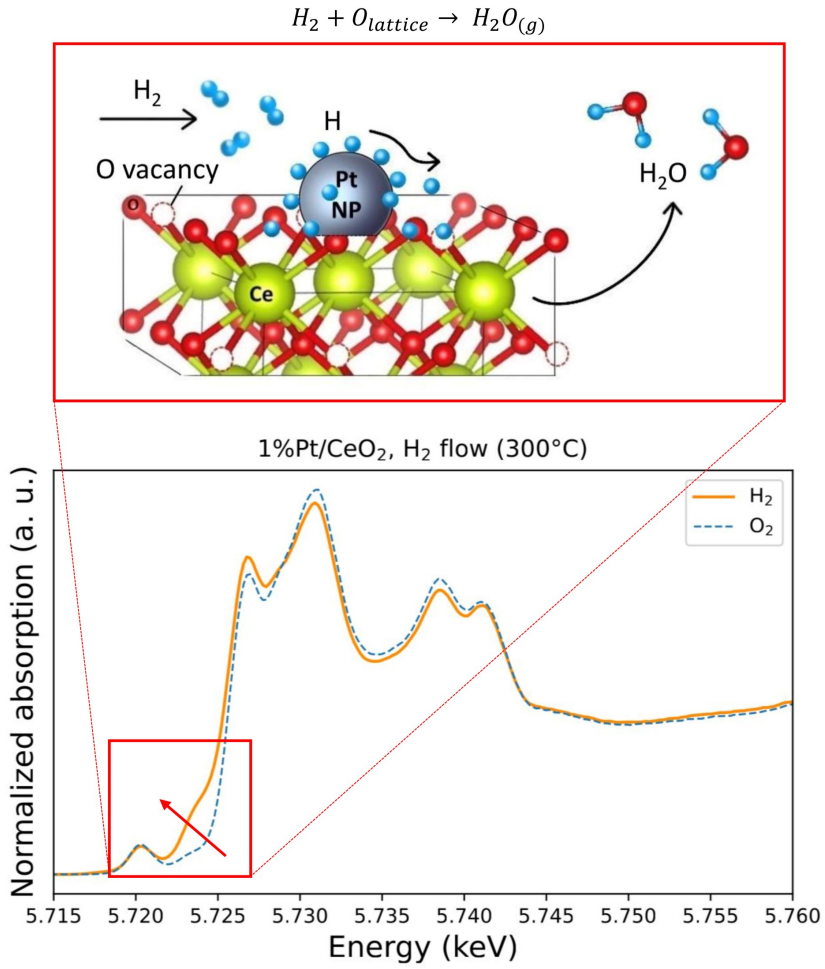

Figure 4.21: H_2O and O vacancies formation upon flowing hydrogen into the cell. New spectral features appear in the near-edge region.

At 50°C, 5 wt % of Pt on a ceria support is sufficient to initiate a reaction, while 1 wt % of Pt requires a slightly higher temperature, as demonstrated by our experiments which indicated that a temperature between 50°C and 200°C is necessary.

- When we flow O_2 onto the sample, the oxygen vacancies previously formed get filled again, and the initial configuration is restored, showing spectral features characteristic of the oxidized state Ce^{4+} in CeO_2 lattice.

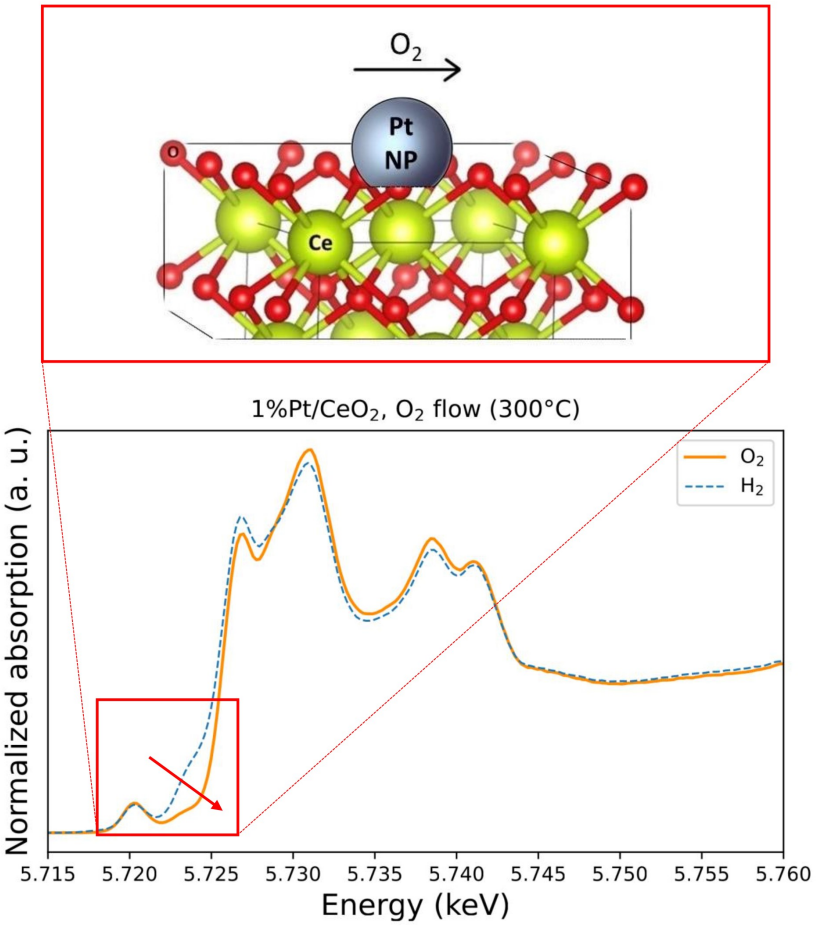

Figure 4.22: O vacancies get filled upon flowing oxygen into the cell. The previously formed new spectral features disappear in the near-edge region.

In summary, our experiments demonstrated that the addition of Pt to a CeO_2 support lowers the ceria reduction temperature. This effect was further elucidated in the preceding section.

Hence, the role of platinum is to reduce the kinetic barrier for the reduction of CeO_2 through Pt-O-Ce bond formation and H-spillover.

We expect such effects to be the main differences - if not the only - between pure ceria and Pt/CeO_2 systems: this would mean that the very same spectral changes would become visible in pure CeO_2 at higher temperatures, namely between 400°C and 500°C.

Moreover, we believe that the principle effect of modifying the wt % of Pt loaded onto the sample from 1% to 5% is to further reduce the reduction temperature, by an increase in PtO_x species and in H atoms spilled onto the support, but we do not expect additional

changes in the electronic structure of ceria. Also, when we compare the shoulder appearing around 5.724 keV in the two cases, we notice that beyond a certain point it does not increase further, appearing similar in the two samples 1%Pt/CeO_2 and 5%Pt/CeO_2 at 300°C. This could be attributed to the possibility that all the weakly-bounded O atoms at the surface have left the lattice, leaving only the O more strongly-bounded to the crystal.

Now that a comprehensive overview of the potential processes occurring during the reduction of ceria has been established, it is pertinent to determine the fraction of Ce involved in the chemical processes shown in Figure 4.21. This calculation is discussed in the following section.

4.2.3. Calculation of the fraction of Pt-Ce sites participating in the interaction

We have observed that the reduction of Ce sites from Ce^{4+} to Ce^{3+} and the formation of oxygen vacancies is somehow related to the spectral changes observed in the 1%Pt/CeO_2 and in the 5%Pt/CeO_2 XANES acquired under hydrogen flow.

Therefore, it is relevant to quantify the amount of Ce^{3+} sites created at the surface in the reduction process, upon interacting with the Pt nanoparticles placed onto the ceria lattice.

In order to do so, Table 4.1 reports the CeO_2 and Pt densities and crystal structure characteristics known in literature, such as the space group, the unit cell parameter and the number of atoms per unit cell (Z).

	Density (g/cm^3)	**Space group**	**Unit cell parameter (nm)**	**Z**
CeO_2	7.22	$Fm\bar{3}m$	0.541	4 Ce
Pt	21.4	$Fm\bar{3}m$	0.392	4 Pt

Table 4.1: CeO_2 and Pt crystal structure specifics.

Detailed calculations are provided in Appendix B, with the main steps to justify our results briefly reported here.

From the characterization analysis presented in *Section 3.1*, we know that a Pt nanoparticle of 1 nm and a ceria crystallite of 7.4 nm are formed in the 5%Pt/CeO_2 sample, therefore it is possible to calculate, under spherical approximation, the volume of the crystallite for

both structures, and similarly the surface area of the Pt hemisphere ($S_{\mathrm{Pt,hemisph.}}$) and the total surface area of the CeO_2 sphere (S_{CeO_2}).

Moreover, knowing that the density is defined as the ratio of mass-to-volume, the masses for the Pt and the CeO_2 crystallites are retrieved, and knowing that for 100 g of CeO_2 sample 5 g of Pt are found, it can be calculated that, on average, for each 7.4 nm-ceria crystallite seven Pt nanoclusters are present onto the surface, creating an active surface area of approximately 6.4% (illustrated in Figure 4.23).

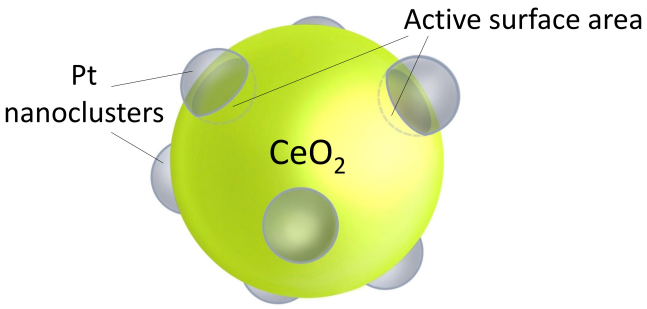

Figure 4.23: Illustration of a CeO_2 crystallite covered by seven Pt nanoparticles, producing 6.4% of active surface area.

For such an active surface area it is possible to calculate that 25 Ce atoms are involved in the interaction, forming 25 Pt-O-Ce bonds, while 48 Pt atoms take an active role in the production of spillover effects.

By comparing the total number of Ce atoms present in the CeO_2 crystallite of 7.4 nm and the number of Ce atoms actively participating in the interaction with platinum, it can be retrieved that only the 0.47% of Ce is involved in the spectral changes appearance at the L_3 edge, assuming that such modifications are effectively related to Pt-CeO_2 interactions inducing ceria reduction.

On the other hand, the number of H_2 spiltover on each ceria crystallite is retrieved from the number of Pt atoms interacting with hydrogen (reported above) and the total number of Ce atoms in the crystallite, leading to 1.79% of H atoms.

Looking at the experimental data reported in *Chapter 3*, it is observed that the shoulder appearing around 5.724 keV does not increase much upon changing the temperature from 200° to 300°C, and neither from changing the wt % of Pt, suggesting that such shoulder may be related to the number of O atoms available at the interface in the active area.

5 | Conclusions and future developments

Beginning with a general overview of ceria, we have observed the many potential uses of this material in the field of biomedicine, surpassing the issues related to existing antioxidants and offering a beneficial solution to cellular oxidative stress and pathological inflammations caused by an excess of ROS in the human body.

We have seen that nanoceria is a good candidate for such purposes because of its peculiar redox properties and consequent oxygen storage capacity, and that research related to this topic is promising and necessary to pave the way towards actual pharmacological applications.

However, we have also underlined how going to the nanoscale affects such redox properties, often dramatically changing the system: the reactivity of complex and nanostructured catalysts strongly differs at the surface from single-crystal systems. This means that chemical properties are closely linked to structure and size characteristics of the system.

Due to the strong connection between the redox properties of ceria and its crystal structure, it is essential to utilize new characterization techniques and theoretical methods to gain a better understanding of this material, so that we can predict its behavior and maximize its potential for applications.

In order to develop good CeO_2 materials for industrial application, it is important to have a clear understanding of the chemical activity of CeO_2, which in turns depends on the electronic structure.

For this reason, the spectroscopic techniques based on synchrotron radiation constitute a powerful tool to study Ce electronic structure with the highest resolution possible, that in combination with other characterization techniques and computational methods, provides a multidisciplinary approach useful to investigate such complex system.

In particular, the work reported by the present thesis stemmed from the necessity to characterize the oxygen vacancy behavior in the CeO_2 lattice when ceria is placed in a

reducing environment. The goal was to acquire high resolution XANES spectra at the L_3 edge of Ce and observe if and how the spectral features change under reducing conditions because of oxygen vacancy formation.

What was noticed with pure ceria samples is that going up to 300°C is not enough to promote oxygen vacancy formation, and upon flowing hydrogen ceria is not reduced.

However, knowing that in the catalysis field ceria is often implemented in combination with noble metal to improve its catalytic activity, we studied also ceria samples with a small percentage of Pt nanoparticles on top, specifically 1% and 5%Pt/CeO_2. We observed for both structures, indeed, that remarkable changes appeared in the near-edge region upon flowing H_2 onto the samples, indicating that some reduction was occurring in ceria (see Figure 5.1).

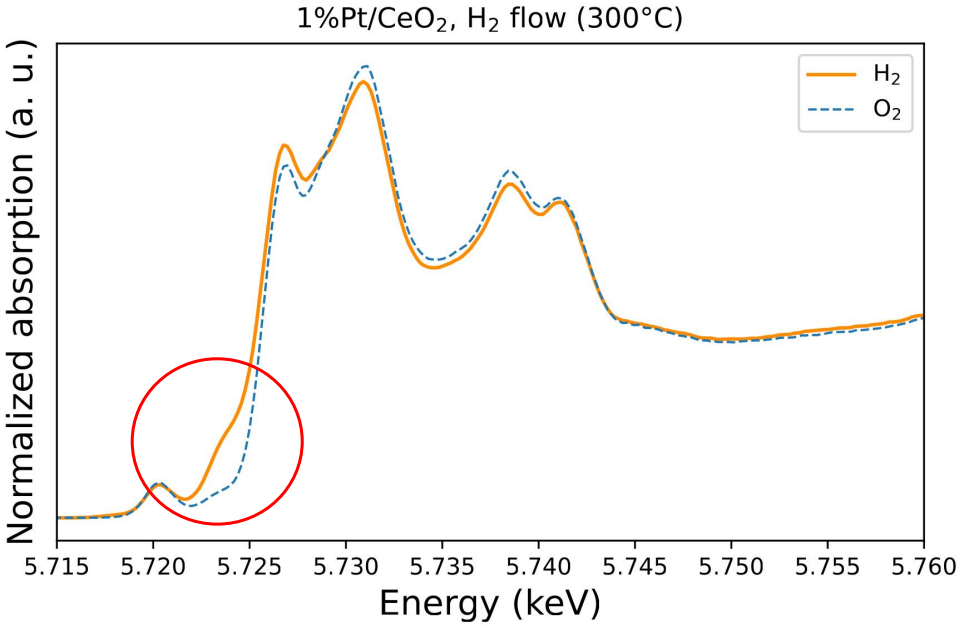

Figure 5.1: XANES spectra acquired at the L_3 edge in 1%Pt/CeO_2 under H_2 and O_2 gas flow at 300°C. Prominent spectral changes are visible around 5.724 keV.

Pt/CeO_2 systems have been extensively studied in catalysis, thus, by making use of past studies reported in literature, we can assume how Pt nanoparticles are influencing the electronic structure of ceria. This allows us to confirm that such spectral alterations are due to the redox properties of ceria alone, which are enhanced at lower temperatures by the presence of Pt, but do not rely on its presence.

In fact, our interest is firmly focused on the ceria support, and not on the catalytic behavior of Pt nanoparticles as it is often the case in catalysis.

It is known in literature that nanosized platinum deposited on nanosized ceria strongly interacts with the support, creating at the surface Pt-O-Ce bonds that weaken the surface oxygen coordination to the ceria fluorite structure, and giving origin to two main phenomena at the nanoscale: electron transfer from Pt nanoclusters to Ce, and oxygen reverse spillover from ceria to Pt, with the common effect of reducing some Ce sites at the interface, creating Ce^{3+}.

In addition to this, under H_2 flow, Pt nanoparticles give rise to hydrogen spillover onto the support surface, promoting the interaction between H and lattice O weakly bounded to the support surface, consequently facilitating the creation of oxygen vacancies in the lattice, together with water formation in the cell.

The process of oxygen vacancy formation is characterized by an oxygen atom leaving the lattice, leaving two electrons behind which localize on neighboring Ce *4f* states, thus reducing Ce^{4+} to Ce^{3+} at the surface.

On the other hand, when oxygen is flown again onto the sample, the new spectral features disappear, and we associate this to the filling of the O vacancies, restoring the Ce^{4+} oxidation state of Ce sites at the surface.

The changes observed around 5.724 keV appear and disappear in each Pt/CeO_2 sample and at every temperature when respectively H_2 and then O_2 are flown onto the material, showing high reproducibility and reversibility.

We believe that such reversible spectral changes are associated to the so-described reversible reduction and oxidation process of some Ce sites, that is in turn related to oxygen vacancy formation, since the valence change from Ce^{4+} to Ce^{3+} of two cations per vacancy is associated to the reversible oxygen release.

This way, the oxygen storage-and-release ability of ceria would give rise to the direct manifestation in the spectra of an electron microscopic process, responsible for the macroscopic properties already known and used in the different ceria applications.

Given the complexity of the electronic structure of the system, it is difficult to correctly attribute the shoulder appearing around 5.724 keV to a specific transition, but to the best of our knowledge, this is the first time that such shoulder is observed to grow *in situ* under reducing conditions, and this opens new questions in the debate of ceria-based catalysis.

Many different theories have been developed concerning the origin of nanosize effects act-

ing on ceria spectral features and related redox properties, but experimental demonstrations are often very demanding, and much investigation is still required to reach efficient industrial and pharmacological application.

We strongly believe that the observed spectral changes would manifest in pure ceria as well, at higher temperatures, *i.e.* 400-500°C, and in order to verify this, the next step would be to reach such temperatures and acquire new spectra at the L_3 edge.

Also, we could ascertain the supposed water formation, as a product of the interaction between flown hydrogen and the surface oxygen from the lattice, by connecting a mass spectrometer at the outlet of the cell, performing *operando* measurements. Finally, time-dependent evolution spectra would be helpful to retrieve the number of Ce species present in the system by looking at the isosbestic points, *i.e.* the intersection points.

In conclusion, we can affirm that much of the redox behavior of ceria is still uncertain, but powerful spectroscopic techniques are continually advancing, giving us a better understanding of its delicate electronic structure. This allows us to detect even the slightest changes, leading to new questions but also greater insight into the ceria debate. The gradual advancement of our knowledge is paving the way for new applications of ceria.

Bibliography

[1] Tiziano Montini, Michele Melchionna, Matteo Monai, and Paolo Fornasiero. Fundamentals and catalytic applications of ceo2-based materials. *Chemical reviews*, 116 (10):5987–6041, 2016.

[2] Lena M Ernst and Victor Puntes. How does immunomodulatory nanoceria work? ros and immunometabolism. *Frontiers in immunology*, 13, 2022.

[3] Geza Telek, Jean-Yves Scoazec, Jacques Chariot, Robert Ducroc, Gerard Feldmann, and Claude Rozé. Cerium-based histochemical demonstration of oxidative stress in taurocholate-induced acute pancreatitis in rats: a confocal laser scanning microscopic study. *Journal of Histochemistry & Cytochemistry*, 47(9):1201–1212, 1999.

[4] Beverly Ann Rzigalinski, D Bailey, L Chow, SC Kuiry, S Patil, S Merchant, and S Seal. Cerium oxide nanoparticles increase the lifespan of cultured brain cells and protect against free radical and mechanical trauma. In *Faseb Journal*, volume 17, pages A606–A606. FEDERATION AMER SOC EXP BIOL 9650 ROCKVILLE PIKE, BETHESDA, MD 20814-3998 USA, 2003.

[5] Jean-Daniel Cafun, Kristina O Kvashnina, Eudald Casals, Victor F Puntes, and Pieter Glatzel. Absence of ce3+ sites in chemically active colloidal ceria nanoparticles. *Acs Nano*, 7(12):10726–10732, 2013.

[6] Frank De Groot and Akio Kotani. *Core level spectroscopy of solids*. CRC press, 2008.

[7] Pantaleo Raimondi. Esrf-ebs: The extremely brilliant source project. *Synchrotron Radiation News*, 29(6):8–15, 2016.

[8] David Morel. Esrf. *European Synchrotron Radiation Facility, Grenoble*, https://www.esrf.fr/about/press-room/intro-esrf-journalists, 2020.

[9] Matthew Newville. Fundamentals of xafs. *Reviews in Mineralogy and Geochemistry*, 78(1):33–74, 2014.

[10] David J Griffiths and Darrell F Schroeter. *Introduction to quantum mechanics*. Cambridge university press, 2018.

[11] Pieter Glatzel, Marcin Sikora, Grigory Smolentsev, and Marcos Fernández-García. Hard x-ray photon-in photon-out spectroscopy. *Catalysis Today*, 145(3-4):294–299, 2009.

[12] Scott Calvin. *XAFS for Everyone*. CRC press, 2013.

[13] Matthew Newville. Fundamentals of xafs. *Center for Advanced Radiation Sources*, Workshop, 2018.

[14] Grant Bunker. *Introduction to XAFS: a practical guide to X-ray absorption fine structure spectroscopy*. Cambridge University Press, 2010.

[15] Frederic C Meunier, Luis Cardenas, Helena Kaper, Břetislav Šmíd, Mykhailo Vorokhta, Rémi Grosjean, Daniel Aubert, Kassiogé Dembélé, and Thomas Lunkenbein. Synergy between metallic and oxidized pt sites unravelled during room temperature co oxidation on pt/ceria. *Angewandte Chemie International Edition*, 60(7): 3799–3805, 2021.

[16] Mauro Rovezzi, Alistair Harris, Blanka Detlefs, Timothy Bohdan, Artem Svyazhin, Alessandro Santambrogio, David Degler, Rafal Baran, Benjamin Reynier, Pedro Noguera Crespo, et al. Texs: in-vacuum tender x-ray emission spectrometer with 11 johansson crystal analyzers. *Journal of synchrotron radiation*, 27(3):813–826, 2020.

[17] Pieter Glatzel, Alistair Harris, Philippe Marion, Marcin Sikora, T-C Weng, Cyril Guilloud, Sara Lafuerza, Mauro Rovezzi, Blanka Detlefs, and Ludovic Ducotté. The five-analyzer point-to-point scanning crystal spectrometer at esrf id26. *Journal of Synchrotron Radiation*, 28(1):362–371, 2021.

[18] L Ducotté, P Glatzel, P Marion, C Lapras, M Lesourd, A Harris, and C Heyman. Mechanical aspects of the id26 emission spectrometer ii: improving stability for a large instrument by the use of multiple air pad supports. *Diamond Light Source Proceedings*, 1(MEDSI-6):e26, 2010.

[19] K Hämäläinen, DP Siddons, JB Hastings, and LE Berman. Elimination of the inner-shell lifetime broadening in x-ray-absorption spectroscopy. *Physical review letters*, 67 (20):2850, 1991.

[20] Vinod K Paidi, Dale L Brewe, John W Freeland, Charles A Roberts, and Johan van Lierop. Role of ce 4 f hybridization in the origin of magnetism in nanoceria. *Physical Review B*, 99(18):180403, 2019.

[21] Marius Retegan. Daxs measurements. *European Syn-*

chrotron Radiation Facility, Grenoble, https://spectroscopy.gitlab-pages.esrf.fr/daxs/modules/measurements.html, 2023.

[22] L Tröger, D Arvanitis, K Baberschke, H Michaelis, U Grimm, and E Zschech. Full correction of the self-absorption in soft-fluorescence extended x-ray-absorption fine structure. *Physical Review B*, 46(6):3283, 1992.

[23] Matteo Bianchini and Pieter Glatzel. A tool to plan photon-in/photon-out experiments: count rates, dips and self-absorption. *Journal of Synchrotron Radiation*, 19 (6):911–919, 2012.

[24] Sara Lafuerza, Marius Retegan, Blanka Detlefs, Ruchira Chatterjee, Vittal Yachandra, Junko Yano, and Pieter Glatzel. New reflections on hard x-ray photon-in/photon-out spectroscopy. *Nanoscale*, 12(30):16270–16284, 2020.

[25] Suresh Gatla, Daniel Aubert, Valérie Flaud, Rémi Grosjean, Thomas Lunkenbein, Olivier Mathon, Sakura Pascarelli, and Helena Kaper. Facile synthesis of high-surface area platinum-doped ceria for low temperature co oxidation. *Catalysis Today*, 333: 105–112, 2019.

[26] Friedrich Esch, Stefano Fabris, Ling Zhou, Tiziano Montini, Cristina Africh, Paolo Fornasiero, Giovanni Comelli, and Renzo Rosei. Electron localization determines defect formation on ceria substrates. *Science*, 309(5735):752–755, 2005.

[27] NV Skorodumova, SI Simak, Bengt I Lundqvist, IA Abrikosov, and Börje Johansson. Quantum origin of the oxygen storage capability of ceria. *Physical Review Letters*, 89(16):166601, 2002.

[28] Børje Johansson, IA Abrikosov, Magnus Aldén, AV Ruban, and Hans Lomholt Skriver. Calculated phase diagram for the γ α transition in ce. *Physical review letters*, 74(12):2335, 1995.

[29] A Kotani, Kristina O Kvashnina, Sergei M Butorin, and P Glatzel. A new method of directly determining the core–hole effect in the ce l3 xas of mixed valence ce compounds—an application of resonant x-ray emission spectroscopy. *Journal of Electron Spectroscopy and Related Phenomena*, 184(3-6):210–215, 2011.

[30] A Kotani, KO Kvashnina, Sergei M Butorin, and P Glatzel. Spectator and participator processes in the resonant photon-in and photon-out spectra at the ce l 3 edge of ceo 2. *The European Physical Journal B*, 85:1–13, 2012.

[31] Kristina O Kvashnina, Sergei M Butorin, and Pieter Glatzel. Direct study of the

f-electron configuration in lanthanide systems. *Journal of Analytical Atomic Spectrometry*, 26(6):1265–1272, 2011.

[32] Shijie Wu, Yu Yang, Chunxiang Lu, Yuanyuan Ma, Shuxia Yuan, and Guangren Qian. Soot oxidation over ceo2 or ag/ceo2: Influences of bulk oxygen vacancies and surface oxygen vacancies on activity and stability of the catalyst. *European Journal of Inorganic Chemistry*, 2018(25):2944–2951, 2018.

[33] Johnny Zhu Chen, Abhijit Talpade, Griffin A Canning, Paige R Probus, Fabio H Ribeiro, Abhaya K Datye, and Jeffrey T Miller. Strong metal-support interaction (smsi) of pt/ceo2 and its effect on propane dehydrogenation. *Catalysis Today*, 371: 4–10, 2021.

[34] Chun-Jern Pan, Meng-Che Tsai, Wei-Nien Su, John Rick, Nibret Gebeyehu Akalework, Abiye Kebede Agegnehu, Shou-Yi Cheng, and Bing-Joe Hwang. Tuning/exploiting strong metal-support interaction (smsi) in heterogeneous catalysis. *Journal of the Taiwan Institute of Chemical Engineers*, 74:154–186, 2017.

[35] José A Rodríguez and Jan Hrbek. Inverse oxide/metal catalysts: A versatile approach for activity tests and mechanistic studies. *Surface Science*, 604(3-4):241–244, 2010.

[36] SJ Tauster, SC Fung, and Rl L Garten. Strong metal-support interactions. group 8 noble metals supported on titanium dioxide. *Journal of the American Chemical Society*, 100(1):170–175, 1978.

[37] Nadia Acerbi, Shik Chi Tsang, Stan Golunski, and Paul Collier. A practical demonstration of electronic promotion in the reduction of ceria coated pgm catalysts. *Chemical communications*, (13):1578–1580, 2008.

[38] Georgi N Vayssilov, Yaroslava Lykhach, Annapaola Migani, Thorsten Staudt, Galina P Petrova, Nataliya Tsud, Tomáš Skála, Albert Bruix, Francesc Illas, Kevin C Prince, et al. Support nanostructure boosts oxygen transfer to catalytically active platinum nanoparticles. *Nature materials*, 10(4):310–315, 2011.

[39] Annapaola Migani, Georgi N Vayssilov, Stefan T Bromley, Francesc Illas, and Konstantin M Neyman. Greatly facilitated oxygen vacancy formation in ceria nanocrystallites. *Chemical communications*, 46(32):5936–5938, 2010.

[40] Albert Bruix, Annapaola Migani, Georgi N Vayssilov, Konstantin M Neyman, Jörg Libuda, and Francesc Illas. Effects of deposited pt particles on the reducibility of ceo 2 (111). *Physical Chemistry Chemical Physics*, 13(23):11384–11392, 2011.

[41] GS Zafiris and Raymond J Gorte. Evidence for low-temperature oxygen migration from ceria to rh. *Journal of Catalysis*, 139(2):561–567, 1993.

[42] Jaeha Lee, YoungSeok Ryou, Xiaojun Chan, Tae Jin Kim, and Do Heui Kim. How pt interacts with ceo2 under the reducing and oxidizing environments at elevated temperature: the origin of improved thermal stability of pt/ceo2 compared to ceo2. *The Journal of Physical Chemistry C*, 120(45):25870–25879, 2016.

[43] Tatiana A Bugrova, Tamara S Kharlamova, Valerii A Svetlichnyi, Anna S Savel'eva, Mikhail A Salaev, and Grigory V Mamontov. Insights into formation of pt species in pt/ceo2 catalysts: Effect of treatment conditions and metal-support interaction. *Catalysis Today*, 375:36–47, 2021.

[44] Wei Tang, Zhenpeng Hu, Miaojun Wang, Galen D Stucky, Horia Metiu, and Eric W McFarland. Methane complete and partial oxidation catalyzed by pt-doped ceo2. *Journal of Catalysis*, 273(2):125–137, 2010.

[45] Suresh Gatla, Daniel Aubert, Giovanni Agostini, Olivier Mathon, Sakura Pascarelli, Thomas Lunkenbein, Marc Georg Willinger, and Helena Kaper. Room-temperature co oxidation catalyst: low-temperature metal–support interaction between platinum nanoparticles and nanosized ceria. *ACS Catalysis*, 6(9):6151–6155, 2016.

[46] Selim Alayoglu, Kwangjin An, Gerome Melaet, Shiyou Chen, Fabiano Bernardi, Lin Wang Wang, Avery E Lindeman, Nathan Musselwhite, Jinghua Guo, Zhi Liu, et al. Pt-mediated reversible reduction and expansion of ceo2 in pt nanoparticle/mesoporous ceo2 catalyst: In situ x-ray spectroscopy and diffraction studies under redox (h2 and o2) atmospheres. *The Journal of Physical Chemistry C*, 117(50): 26608–26616, 2013.

[47] S Khoobiar. Particle to particle migration of hydrogen atoms on platinum—alumina catalysts from particle to neighboring particles. *The Journal of Physical Chemistry*, 68(2):411–412, 1964.

[48] Waiz Karim, Clelia Spreafico, Armin Kleibert, Jens Gobrecht, Joost VandeVondele, Yasin Ekinci, and Jeroen A van Bokhoven. Catalyst support effects on hydrogen spillover. *Nature*, 541(7635):68–71, 2017.

[49] W Curtis Conner Jr and John L Falconer. Spillover in heterogeneous catalysis. *Chemical reviews*, 95(3):759–788, 1995.

[50] Simon K Beaumont, Selim Alayoglu, Colin Specht, Norbert Kruse, and Gabor A Somorjai. A nanoscale demonstration of hydrogen atom spillover and surface diffusion

across silica using the kinetics of co2 methanation catalyzed on spatially separate pt and co nanoparticles. *Nano letters*, 14(8):4792–4796, 2014.

A | Appendix A

In the present appendix a description of the beamline ID26 at the European Synchrotron Radiation Facility (ESRF) in Grenoble is provided. Figure A.1 shows a schematic layout of the optical elements through which the X-ray beam is passing along its path from the storage ring, the undulators and then towards the sample in the experimental hutch. The functioning and the purpose of each device is described below starting from the two optical hutches and proceeding towards the two experimental ones.

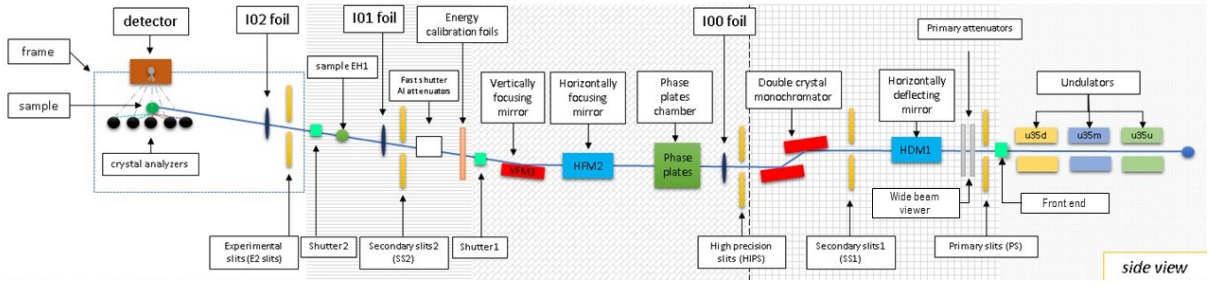

Figure A.1: Schematic side view of the ID26 beamline.

Optics Hutch 1

- **Front end**: at the very beginning of the beamline, it is the first shutter. It is able to block every radiation coming from the ring when the synchrotron is running, preventing even stray radiation from reaching the rest of the beamline.
- **Primary slits**: they are characterized by a horizontal long shape to prevent from melting when hit by the 1 kW beam coming from the open shutter. The wedge-shape is needed to reduce the heat density per surface, distributing the 1 mm thickness of the beam over 8 cm under a certain angle, in each direction. Having this very long footprint, it is possible to very efficiently evacuate the heat with the water cooling.
- **Primary attenuators**: they are two and they are useful to control the heat load. They select the right range of energies by using a diamond window placed across the beam: the polychromatic photon beam goes through the diamond, which is

sufficiently thin such that the high energy photons are not attenuated, while, at the same time, the low energy photons considerably are. Between the two attenuators there is the so-called **Wide Beam Viewer**, used to visualize the beam. It is based on a diamond coated with some fluorescence material and a camera; in the middle there is a deflecting small mirror and the optical camera is looking at the image of the beam which is created by the fluorescence screen that is put into the beam whenever it is required to visualize it.

- **Horizontally deflecting mirror**: the mirror will deflect the beam horizontally in the outside direction, and depending on the energy where we work, we can choose different mirror coatings. Three possible stripes are available: Pd, Pt and Si stripe, depending on the chosen energy; silicon is used at low energies and Pt and Pd can be used at high energies. The beam comes in slightly divergent and will leave again divergent roughly the same way.
- **Secondary slits**: these slits look more oblate with respect to the primary ones. They are centered around the beam, typically moving the two slits together by either changing the gap – we open and close – or moving them left and right or up and down.
- **Monochromator**: it is a double crystal monochromator equipped with two sets of crystals: Si(111), used at low energies (where the range of working energies starts from 2.5 keV and goes up to around 20 keV), and Si(311), used starting from 4.8-4.9 keV. Each set of crystals gives a different energy resolution: in fact, the monochromatic beam that leaves the monochromator is narrower in the energy bandwidth. The main monochromator – Si(111) – provides a resolution in the order of 1 to 2 eV, while Si(311) provides something in the order of 300 meV: for many experiments this makes the main difference, since when the goal is to observe features in a spectrum requiring high resolution, Si(111) is not suited. A system of primary pump, turbomolecular pump and ion pump is employed around the monochromator to create vacuum, while a low temperature is kept by using liquid nitrogen.

All along the beamline valves are used to isolate one section from the other, and pressure gauges are placed to read the pressure in the section: this way, eventual problems arising in one section will not vent the rest of the beamline.

Optics Hutch 2

- **High precision slits and I00 foil**: Additional slits are present at this stage, together with one of the first intensity monitors, indicated with I00. These devices

are used to monitor the flux intensity of the X-rays coming in, making the beam pass through something which is semi-transparent for the X-rays and such that the absorption is very low. Typically, for this purpose, a very thin Kapton foil is used, whose thickness is chosen between 15, 20 or even 50 μm, depending on the working energy. The beam passing through the Kapton foil creates scattering and, in order to record this scattering, a four-quadrant diode is placed just before the foil: this kind of diode is equipped with a small hole in the middle and four diodes around it, such that the beam can pass though the diode's hole and then proceed towards the Kapton foil, producing backscattered radiation when crossing the latter. The so-produced backscattering is then recorded by the four-quadrant diode, mounted to look at the backscattered radiation from the foil. This way, we attenuate just a few percentage of the beam, allowing the rest to continue straight on. There are several monitors like the I00 one along the beamline (called I01, I02, I0t, and I04).

- **Phase plates chamber**: this chamber is used to modify the polarization of the X-rays by inserting a diamond crystal into the beam: in fact, by putting the diamond crystal into a diffraction condition (dynamical diffraction) a phase shift between polarization states of the X-rays is created. The X-rays coming from the synchrotron undulators are σ-polarized in the horizontal plane, therefore, depending on the phase shift that is used, it is possible to either rotate polarization (shifting to π-polarization) or create circular polarization (circular left and circular right).
- **Horizontally and vertically focusing mirror**: in order to focus the beam two stages are employed, one for the horizontal direction and the other for the vertical one. Similar to the deflecting mirror, such focusing mirrors have three stripes that can be selected by moving the system up and down. Different materials and different angles are used in order to cut the undesired energies and translations and rotations with six degree of freedom can be achieved.

In order to visualize the beam, cameras are placed along the beamline: one is present right after the monochromator (based on a fluorescence screen which is seen by the camera), and then the next one is in the experimental hutch at the sample position to check the beam size. This is sufficient because at the earlier stages of the beamline diodes provide the needed information, since in principle the size of the beam is not relevant there.

Experimental Hutch 1

The first experimental hutch presents a TEXS chamber, which is a tender X-ray emission spectrometer encased in a large high-vacuum chamber, providing enough room for *in*

situ and *operando* experimental setups. This chamber is optimized for energies between 1.5 keV and 5.5 keV and it implements 11 Johansson crystal analyzers arranged in a Rowland circle geometry, covering an angular range between 35° and 88°. Depending on the emission energy that we would like to record, we use combinations of different sets of analyzer crystals to completely cover the energy range.

Experimental Hutch 2

In the second experimental hutch the beam comes in through a large tube, whose diameter is large enough to facilitate the pumping procedure upon reducing the impedance of the tube. Before the arrival of the beam upon the sample, the following components are present:

- **Slits**: these define the beam size and the beam position: sometimes, in fact, it is required to use a beam size which is smaller than the minimum beam size reached from the source and from the focusing mirrors. Although in this way the flux is reduced, for some experiments this is needed.
- **I02 foil**: with I02 the same concept of I00 intensity monitor is repeated: the beam goes through the diode's hole and then through a Kapton foil, from which the backscattering is read by the four-quadrant diode.
- **Beryllium window**: After the Kapton foil, the beam leaves the beamline crossing a beryllium window, used to isolate the vacuum created inside the beamline. Beryllium is a good candidate to constitute the exit window: in fact, being a light metal, we expect it to absorb very little of the X-ray beam. At the same time though, gas nitrogen has to be continuously flushed onto the surface of the beryllium window in order to prevent the formation of beryllium oxide (which is carcinogenic) from the reaction with the air ionized by the beam. Once it has crossed the beryllium window, the beam goes onto the sample.

B | Appendix B

Here it is reported the detailed calculation for the number of Ce sites participating in the interaction between the CeO_2 ($r_{CeO_2} = 3.7$ nm) and the Pt nanoparticles ($r_{Pt} = 0.5$ nm), whose results are presented in *Section 4.2.3*.

The volume of the crystallite for both CeO_2 and Pt structures was calculated under spherical approximation, finding the following numerical values:

$$V_{CeO_2} = \frac{4}{3}\pi r_{CeO_2}^3 = 212nm^3 \tag{B.1}$$

$$V_{Pt} = \frac{4}{3}\pi r_{Pt}^3 = 0.524nm^3 \tag{B.2}$$

Similarly, the surface area of the Pt nanoparticle hemisphere ($S_{Pt,hemisph.}$) and the total surface area of the CeO_2 crystallite (S_{CeO_2}) are calculated:

$$S_{CeO_2} = 4\pi r_{CeO_2}^2 = 172nm^2 \tag{B.3}$$

$$S_{Pt,hemisph.} = \frac{4\pi r_{Pt}^2}{2} = 1.57nm^2 \tag{B.4}$$

Knowing that the density is defined as the mass/volume ratio, the total mass of the CeO_2 crystallite (M_{CeO_2}) and of the single Pt nanoparticle ($M_{Pt,1NP}$) are calculated, while, knowing that in the 5%Pt/CeO_2 sample for 100 g of ceria there is a quantity of 5 g of Pt, by making a simple proportion, the mass of the total amount of Pt present on one crystallite of CeO_2 ($M_{Pt,TOT}$) is retrieved. Then, dividing the total mass by the mass of the single Pt nanoparticle, the number of Pt nanoparticles for each ceria crystallite ($N_{Pt,NP}$) is obtained.

$$M_{CeO_2} = \rho_{CeO_2} V_{CeO_2} = 1.53 \cdot 10^{-18} g \tag{B.5}$$

$$M_{Pt,1NP} = \rho_{Pt} V_{Pt} = 1.12 \cdot 10^{-20} g \tag{B.6}$$

$$100g : 5g = M_{CeO_2} : M_{Pt,TOT} \tag{B.7}$$

$$N_{Pt,NP} = \frac{M_{Pt,TOT}}{M_{Pt,1NP}} \simeq 7 \tag{B.8}$$

Defining the active surface area of Pt ($S_{Pt,active}$) as the area of contact between the Pt NPs and the ceria crystallite, having 7 Pt NPs on a single ceria crystallite means that $S_{Pt,active}$ is given by seven times the surface area of the single Pt NP hemisphere. Then, it is found, by dividing such surface area by the total ceria surface area (S_{CeO_2}), that the ceria crystallite surface area involved in the interaction with Pt (S_{active}) is 6.4%.

$$S_{Pt,active} = 7 \cdot (1.57nm^2) = 10.99nm^2 \tag{B.9}$$

$$S_{active} = \frac{S_{Pt,active}}{S_{CeO_2}} \simeq 6.4\% \tag{B.10}$$

Now it is necessary to calculate how many atoms of Pt and Ce are involved in such active surface area, and in order to do so we have to start by calculating how many lattice cells are facing S_{active}. We proceed by making an underestimation and considering for each cubic cell a surface S_{cell} given by all the faces of the cube ($6a^2$), and then we divide the total active surface area of Pt by the area occupied by the single cell to find the number of cells (N_{cells}). Knowing that for each cell there are 4 atoms (both for Pt and for Ce in the respective lattices), multiplying the number of cells by 4 it is possible to retrieve the number of atoms participating in the interaction (N).

$$N_{Pt} = \frac{S_{Pt,active}}{6(a_{Pt})^2} \cdot 4 = N_{cells,Pt} \cdot 4 \simeq 48 \tag{B.11}$$

$$N_{Ce} = \frac{S_{Pt,active}}{6(a_{CeO_2})^2} \cdot 4 = N_{cells,CeO_2} \cdot 4 \simeq 25 \tag{B.12}$$

Therefore, for 25 atoms of Ce at the interface between Pt and ceria, 25 Pt-O-Ce bonds are created, and diving this number by the total number of Ce atoms present in the crystallite, the percentage of Ce sites participating in the interaction is obtained ($\%Ce$).

To find the total number of Ce atoms for a single 7.4 nm-crystallite, we divide the total volume of the crystallite by the volume of the single lattice cell and multiply by 4:

$$N_{Ce,TOT} = \frac{V_{CeO_2}}{(a_{CeO_2})^3} \cdot 4 \simeq 5368 \tag{B.13}$$

$$\%Ce = \frac{25}{5368} \cdot 100 = 0.47\% \tag{B.14}$$

Finally, the percentage of H_2 molecules interacting with Pt for each ceria crystallite is given by the ratio between the number of Pt atoms N_{Pt} and the total number of Ce atoms. Then, multiplying by 2, the percentage of H atoms spiltover the support is retrieved.

$$N_{H,spilt} = \frac{N_{Pt}}{N_{Ce,TOT}} \cdot 2 \cdot 100 \simeq 1.79\% \tag{B.15}$$

List of Figures

1.1 Histogram of the number of publications concerning ceria (blue bars) and ceria in the catalysis field (red bars) from 1994 to 2015 [1]. 1
1.2 Ceria lattice releasing O atoms under reducing environment (H_2), and storing oxygen under oxidizing environment (O_2). 2
1.3 a) Time dependent X-ray absorption spectra during *in situ* synthesis of ceria nanoparticles. At time t=0 cerium is Ce^{3+}, while it progressively shifts to its Ce^{4+} configuration; b) Magnification of the pre-edge region corresponding to *2p* to *4f* quadrupole transitions for the two oxidation states of Ce [5]. 7

2.1 The European Synchrotron Radiation Facility (71 Av. Martyrs, 38000 Grenoble) [8]. 12
2.2 Schematic absorption process of an X-ray photon with consequent emission of a core electron [9]. 13
2.3 Schematic depiction of an X-ray beam of intensity I_0 crossing a sample of thickness t and leaving with final intensity I. 14
2.4 Schematic fluorescent de-excitation process of an electron filling the core hole with consequent emission of an X-ray photon [9]. In this example, the emission lines depicted are the K_α, involving the *2p-1s* transitions and the K_β, involving the *3p-1s*. 15
2.5 Schematic layout of the experimental setup for measuring in fluorescence mode (achieved through the five-analyzer crystal spectrometer) and in transmission mode at ID26 [11]. 16
2.6 Example of absorption spectrum for the Fe K edge of FeO. Two regions are distinguished: the near-edge (XANES) region and the extended fine structure (EXAFS) [13]. 17
2.7 XRD experiment scheme: the incident radiation is scattered by the atomic planes and produces constructive interference with itself when Bragg's law is fulfilled. 18
2.8 Shorter caption 19

2.9 Shorter caption . . . 21
2.10 Side view and top view of the ID26 beamline. In the upper layout all the optical, electronic and physical elements are depicted, while in the lower one all the motors responsible for the movements of the devices are reported. 22
2.11 Source volume, analyzer crystal and detector placed on a Rowland circle [17]. 24
2.12 a) Motion of the crystal analyzer and the detector on the Rowland circle when changing the Bragg angle. Notice that the Bragg angle is the same from any point on the circle [16]; b) Multi-crystal analyzer layout composed by 5 crystals in the sagittal plane. Each crystal defines a Rowland circle [17]. . . . 25
2.13 Five-analyzer crystals in experimental hutch EH2 at ID26 [18]. . . . 26
2.14 EH2 at ID26, He bag between the sample, the analyzer crystals and the detector. . . . 27
2.15 Comparison between HERFD and Total Fluorescence Yield (TFY) XANES spectra, acquired at the L_3 edge of ceria [5]. . . . 29
2.16 Geometry of the experimental setup in a photon-in/photon-out experiment [23]. . . . 31
2.17 Schematic layout of the cell. . . . 33
2.18 Experimental setup at ID26. The X-ray beam is sent onto the cell containing the sample, and the consequently emitted radiation is collected and focused by the five analyzer crystals onto the detector. . . . 34

3.1 XRD pattern of the spent catalyst and of 5%Pt/CeO_2 as-synthesized sample (study performed by Meunier et al. [15]) . . . 36
3.2 Representative HAADF-STEM images of the Pt/CeO_2 catalyst (a, b) and the corresponding Pt particle sizes distribution (c) [15] . . . 37
3.3 Selected Area Electron Diffraction (SAED) on the reduced sample ([15], SI). 37
3.4 Selected Area Electron Diffraction (SAED) on the spent sample ([15], SI). 38
3.5 a) NAP-XPS Pt 4f core levels measured over the Pt/CeO_2 sample at room temperature under O_2, O_2+CO, CO, and then CO+O_2 again. b) Corresponding distribution of Pt oxidation states under the different gas compositions [15]. . . . 39
3.6 XANES spectra of the four samples (CeO_2 commercial, CeO_2 lab synthesized, 1%Pt/CeO_2 and 5%Pt/CeO_2) acquired under helium gas flow at 50°C. . . . 40

3.7 Self-absorption evaluation for the lab synthesized CeO_2 spectrum: self-absorption distortion is applied to the non-distorted commercial CeO_2 spectrum, which is subsequently fitted onto the lab synthesized CeO_2 spectrum affected by self-absorption. 41
3.8 XANES spectra of the commercial CeO_2 sample, acquired at 50°C under helium, hydrogen, oxygen and no gas flow. 43
3.9 XANES spectra of the commercial CeO_2 sample, acquired at 200°C under helium, hydrogen, oxygen and no gas flow. 44
3.10 XANES spectra of the commercial CeO_2 sample, acquired at 300°C under helium, hydrogen, oxygen and no gas flow. 44
3.11 XANES spectra of the lab synthesized CeO_2 sample, acquired at 50°C under helium, hydrogen, oxygen and no gas flow. 45
3.12 XANES spectra of the lab synthesized CeO_2 sample, acquired at 200°C under helium, hydrogen, oxygen and no gas flow. 46
3.13 XANES spectra of the lab synthesized CeO_2 sample, acquired at 300°C under helium, hydrogen, oxygen and no gas flow. 46
3.14 XANES spectra of the 1%Pt/CeO_2 sample, acquired at 50°C under helium, hydrogen, oxygen and no gas flow. Inset shows the magnified region around 5.724 keV. 47
3.15 XANES spectra of the 1%Pt/CeO_2 sample, acquired at 200°C under helium, hydrogen, oxygen and no gas flow. 48
3.16 XANES spectra of the 1%Pt/CeO_2 sample, acquired at 300°C under helium, hydrogen, oxygen and no gas flow. 48
3.17 XANES spectra of the 5%Pt/CeO_2 sample, acquired at 50°C under helium, hydrogen, oxygen and no gas flow. 49
3.18 XANES spectra of the 5%Pt/CeO_2 sample, acquired at 200°C under helium, hydrogen, oxygen and no gas flow. 50
3.19 XANES spectra of the 5%Pt/CeO_2 sample, acquired at 300°C under helium, hydrogen, oxygen and no gas flow. 50
3.20 Difference XANES spectra (H_2-O_2) of the 5%Pt/CeO_2 sample at 50°C, 200°C, and 300°C. 51

4.1 XANES spectrum of the 1%Pt/CeO_2 sample acquired under hydrogen gas flow (orange line), compared to the one acquired under oxygen flow (dashed blue line). 54
4.2 Scheme of the oxygen vacancy formation process in ceria: when the oxygen atom leaves the lattice, two electrons are localized on two Ce atoms [27]. . 56

4.3 Schematic diagram of Ce electronic structure in CeO_2. The red arrows represent the probed *2p* to *5d* transitions and two possible de-excitation paths (not considered in this section) [29]. 57
4.4 Schematic diagram of mixed valence state of Ce in CeO_2. The red arrows represent the probed $2p_{3/2}$ to *5d* transitions and the four possible de-excitation paths [30]. 58
4.5 Schematic diagram of the improved model for Ce electronic structure in CeO_2. The red arrows represent the probed *2p* to *5d* transitions and two possible de-excitation paths (not considered in this section) [30]. 59
4.6 Comparison of the XANES spectra in pure CeO_2 and in 1%Pt/CeO_2 and 5%Pt/CeO_2, acquired under hydrogen gas flow at 50°C. 61
4.7 Comparison of the XANES spectra in pure CeO_2 and in 1%Pt/CeO_2 and 5%Pt/CeO_2, acquired under hydrogen gas flow at 300°C. 61
4.8 Schematic depiction of a metal particle onto an a support and the interfacial effects arising due to SMSI [34]. 64
4.9 Density of states plot calculated for a pure $Ce_{40}O_{80}$ nanoparticle (dashed lines) and for the $Pt_8/Ce_{40}O_{80}$ system (solid line). The energies are plotted with respect to the Fermi level of $Pt_8/Ce_{40}O_{80}$ [38]. 65
4.10 Electron transfer from Pt nanocluster to ceria support depicted for a $Pt_8/Ce_{40}O_{80}$ system [38]. 65
4.11 Geometric effect of encapsulation induced by strong metal-support interaction [34]. 66
4.12 Geometric effect induced by weak or strong metal-support interaction [34]. 67
4.13 Reverse spillover of oxygen from the nanoceria support to the Pt cluster [38]. 67
4.14 Bifunctional effect of reactive species *B* migrating from the metal to the support, where it interacts with second reactive species *A* provided by the oxide [34]. 68
4.15 H_2 temperature-programmed reduction curves of CeO_2 and 2%Pt/CeO_2 [42] 70
4.16 Pt–O–Ce bond formed between Pt and CeO_2 after an oxidative treatment [42] 71
4.17 (a) Plots of % atom Ce^{3+} as a function of temperature in Pt/CeO_2 (blue line) and pure CeO_2 (red line), calculated from quantification analysis of APXPS spectra acquired under H_2. (b) Plot of % atom Ce^{3+} in Pt/CeO_2 in redox conditions at 350°C [46] 72
4.18 XANES spectra at the L_3 edge for liquid $CeCl_3$ in H_2O and at RT, and for 1%Pt/CeO_2 under H_2 flow at 50°C and 300°C. 73
4.19 XANES spectra at the L_3 edge for liquid $CeCl_3$ in H_2O and at RT, for pure CeO_2 under H_2 flow at 300°C, and for 1%Pt/CeO_2 under H_2 flow at 300°C. 74

4.20 Pictorial visualization of the interaction at 300°C of (a) pure CeO_2 with H_2, where no chemical reaction originates and (b) Pt/CeO_2 with H_2, where water formation is speculated. 75
4.21 H_2O and O vacancies formation upon flowing hydrogen into the cell. New spectral features appear in the near-edge region. 77
4.22 O vacancies get filled upon flowing oxygen into the cell. The previously formed new spectral features disappear in the near-edge region. 78
4.23 Illustration of a CeO_2 crystallite covered by seven Pt nanoparticles, producing 6.4% of active surface area. 80

5.1 XANES spectra acquired at the L_3 edge in 1%Pt/CeO_2 under H_2 and O_2 gas flow at 300°C. Prominent spectral changes are visible around 5.724 keV. 82

A.1 Schematic side view of the ID26 beamline. 91

List of Tables

4.1 CeO_2 and Pt crystal structure specifics. 79

List of Symbols

Variable	Description	SI unit
$\boldsymbol{\lambda}$	wavelength	nm
$\boldsymbol{\nu}$	frequency	s^{-1}
$\boldsymbol{h}$	Planck's constant	$J{\cdot}s$
$\boldsymbol{\mu}$	absorption coefficient	m^{-1}

Acknowledgements

I want to thank Professor Ghiringhelli for giving me the opportunity to spend six months at ESRF, offering me the chance to experience firsthand how research is performed in one of the biggest european centers, and then I want to extend my gratitude to Dr. Pieter Glatzel for welcoming me into his beamline and showing me how stimulating a reseach environment can be, especially when driven by the passion for science.

I acknowledge ESRF for granting me beamtime and resources, and all the ID26 staff for helping my research and making my stay at ESRF incredible and inspiring.

Especially, I want to thank Vinod, for mentoring me all along my six months and after that, teaching me a lot and encouraging my individual work while altogether guiding me. Thank you for supervising me during the writing of the thesis, but also for supporting me through the many presentations, they helped both my work and my personal growth.

Thanks to Luca for the countless times that he helped me, to his Saint-Gobain collaborators for providing the samples, and to Alexander and the sample environment for providing the cell. Thanks to Francesca for sharing this wonderful experience with me, and to Michelangelo, who encouraged me unquestioningly like always, all along my path.

Last but not least, I want to thank my parents: it may seem obvious at this point, but I never take your unconditional support for granted, and I have never once failed to find it.